

**$b$  quark tagging performance and  
Higgs detection via top production  
using the ATLAS detector**

Andrew Norman Pickford

Department of Physics & Astronomy  
University of Glasgow

*Thesis submitted for the degree of  
Doctor of Philosophy*

May 2001

© A. N. Pickford, May 2001

ProQuest Number: 11007876

All rights reserved

INFORMATION TO ALL USERS

The quality of this reproduction is dependent upon the quality of the copy submitted.

In the unlikely event that the author did not send a complete manuscript and there are missing pages, these will be noted. Also, if material had to be removed, a note will indicate the deletion.



ProQuest 11007876

Published by ProQuest LLC (2018). Copyright of the Dissertation is held by the Author.

All rights reserved.

This work is protected against unauthorized copying under Title 17, United States Code  
Microform Edition © ProQuest LLC.

ProQuest LLC.  
789 East Eisenhower Parkway  
P.O. Box 1346  
Ann Arbor, MI 48106 – 1346

GLASGOW  
UNIVERSITY  
LIBRARY

12262  
COPY 1

## Abstract

The single particle response of the ATLAS Inner Detector has been simulated. The impact parameter resolution was parameterised as  $\sigma(d_0) = 11 \oplus 59/p_T$   $\mu\text{m}$  and  $\sigma(z_0) = 85 \oplus 94/p_T$   $\mu\text{m}$ , with  $p_T$  in GeV. The  $b$ -tagging performance was evaluated, for a  $b$ -tagging efficiency  $e_b = 0.5$ , the light quark rejection  $R_u = 83 \pm 6$  for 97% silicon microstrip and pixel detector efficiency and  $R_u = 61 \pm 4$  for 90% detector efficiency for 200 GeV jets. The viability for a Higgs boson search using the channel  $t\bar{t}H \rightarrow bW^+\bar{b}W^-b\bar{b}$  was examined. For a total integrated luminosity of  $3 \cdot 10^4 \text{pb}^{-1}$  and a Higgs boson of mass  $m_H = 80$  GeV the signal significance was 11.7, for  $m_H = 100$  GeV 6.5, above  $m_H = 110$  GeV the signal significance fell below the  $5\sigma$  level.

*This thesis is dedicated to my parents*

## Author's Declaration

The work described in this thesis was done by the author. No portion of the work referred to in this thesis has been submitted in support of an application for another degree or qualification of this or any other university or other institute of learning. The software tools used to perform this work were written by the ATLAS Collaboration and others.

# Acknowledgements

This work owes much to the active help and kindness of many people. I would like to express my thanks to my supervisors, Prof. Kenway Smith and Tony Doyle. Without their help and encouragement this thesis would never have been written.

I also owe thanks to the ATLAS Inner Detector group, in particular Alan Poppleton and Giorgos Stavropoulos for writing and explaining the iPatRec reconstruction package.

My thanks go to Maya Stavrianakou for her help at CERN and Catherine MacIntyre for sorting out many of the problems that cropped up over the years.

I gratefully acknowledge the financial support MCP Wafer Technology Ltd. (now Wafer Technology Ltd.) for their sponsorship of the Particle Physics & Astronomy Research Council CASE award which enabled me to study at Glasgow.

Finally many thanks go to the other members of the Glasgow PPE group, fellow students and staff, with whom working was a pleasure.

*2001*  
*Glasgow*

# Notation

Throughout this thesis the following notation will be used. The coordinate system has its origin at the interaction point of the LHC colliding proton beams, with the  $z$ -axis parallel to the beam direction. The  $(x, y)$  or  $(r, \phi)$  coordinate systems are used, as appropriate, to denote positions in the transverse plane. The positive  $x$ -axis is defined as pointing from the interaction point to the centre of the LHC ring, with the positive  $y$ -axis pointing upwards. The azimuthal angle  $\phi$  is measured around the beam axis and polar angle  $\theta$  is the angle from the beam axis of a track or to a given point. The pseudorapidity  $\eta$  is defined as

$$\eta = -\ln \tan(\theta/2)$$

$\Delta R$  is the distance in the pseudorapidity-azimuthal angle space

$$\Delta R = \sqrt{(\Delta\eta)^2 + (\Delta\phi)^2}$$

The transverse momentum  $p_T$ , energy  $E_T$  and other transverse variables are defined in the  $xy$  plane.

The trajectories of charged particles are described by five helix parameters in a uniform magnetic field. These quantities are all measured at the point of closest approach of the track to  $x = y = 0$ . The parameters are:

$1/p_T$  the reciprocal of the transverse momentum;

$\phi$  the azimuthal angle, where  $\tan \phi = p_x/p_y$ ;

$d_0$  the transverse impact parameter, the distance to the beam axis at the point of closest approach;

$\cot \theta$  the cotangent of the polar angle, where  $\cot \theta = p_z/p_T$ ;

$z_0$  the longitudinal impact parameter, the  $z$  position of the track at the point of closest approach in the  $xy$  plane.

Masses, momenta and energies are expressed in units where  $\hbar = c = 1$ .

# Contents

<b>Author's Declaration</b>	<b>ii</b>
<b>Acknowledgements</b>	<b>iii</b>
<b>Notation</b>	<b>iv</b>
<b>List of Figures</b>	<b>ix</b>
<b>List of Tables</b>	<b>xii</b>
<b>1 Introduction</b>	<b>1</b>
<b>2 Theory</b>	<b>4</b>
2.1 Introduction . . . . .	4
2.2 Fundamental Interactions . . . . .	4
2.3 The Standard Model . . . . .	5
2.4 Standard Model Dynamics . . . . .	6
2.5 The Higgs Mechanism . . . . .	11
2.6 Summary . . . . .	22
<b>3 LHC Phenomenology</b>	<b>23</b>
3.1 Introduction . . . . .	23
3.2 LHC Accelerator . . . . .	23
3.3 Physics at the LHC . . . . .	25
3.4 Higgs Production . . . . .	25
3.5 Higgs Decay Modes . . . . .	27
3.6 $t\bar{t}H$ . . . . .	31
3.7 Summary . . . . .	32
<b>4 The ATLAS Experiment</b>	<b>34</b>
4.1 Introduction . . . . .	34
4.2 Detector Overview . . . . .	34

---

4.3	Detector Subsystems . . . . .	36
4.3.1	Magnet System . . . . .	36
4.3.2	Muon Spectrometer . . . . .	38
4.3.3	Calorimetry . . . . .	41
4.3.4	Inner Detector . . . . .	44
4.4	Triggering . . . . .	55
4.5	Summary . . . . .	56
<b>5</b>	<b>Single Track Performance</b>	<b>57</b>
5.1	Overview of ATLAS Software . . . . .	57
5.1.1	Detector Simulation . . . . .	58
5.1.2	Digitisation . . . . .	59
5.1.3	Reconstruction . . . . .	59
5.2	Track Parameter Resolutions . . . . .	63
5.2.1	Track Parameterisation . . . . .	64
5.2.2	Momentum Resolution . . . . .	65
5.2.3	Angular Resolution . . . . .	66
5.3	Impact Parameter . . . . .	70
5.3.1	Parameterisation . . . . .	70
5.3.2	Simulation Results . . . . .	72
5.4	Summary . . . . .	83
<b>6</b>	<b><i>b</i> quark tagging</b>	<b>84</b>
6.1	Introduction . . . . .	84
6.2	Overview . . . . .	84
6.3	Simulation Procedure . . . . .	85
6.3.1	Primary Vertex . . . . .	86
6.3.2	Significance distribution . . . . .	86
6.3.3	Tagging Methods . . . . .	88
6.3.4	Track Selection . . . . .	90
6.3.5	Track reconstruction efficiency and quality . . . . .	91
6.4	<i>b</i> Tagging Performance . . . . .	96
6.4.1	Detector Misalignment . . . . .	98
6.5	Reduced Layout Performance . . . . .	101
6.5.1	Layouts . . . . .	103
6.5.2	Simulation . . . . .	105
6.5.3	Track Selection . . . . .	105
6.5.4	Analysis . . . . .	108
6.5.5	Track Quality . . . . .	110
6.6	Summary . . . . .	115

---

<b>7</b>	<b>Higgs Analysis</b>	<b>117</b>
7.1	Introduction . . . . .	117
7.2	Simulation . . . . .	118
7.3	Signal . . . . .	120
7.3.1	Event Characteristics . . . . .	122
7.3.2	Higgs Signal . . . . .	125
7.3.3	$b_H$ identification . . . . .	127
7.3.4	Signal Summary . . . . .	140
7.4	Background . . . . .	140
7.4.1	Irreducible Backgrounds . . . . .	142
7.4.2	Semi-irreducible Backgrounds . . . . .	142
7.4.3	Reducible Backgrounds . . . . .	144
7.5	Background Reduction . . . . .	147
7.5.1	Tagging Efficiency . . . . .	147
7.5.2	$p_T$ Cut . . . . .	149
7.5.3	$\eta$ Cut . . . . .	150
7.5.4	Background Reduction Summary . . . . .	151
7.6	Event Reconstruction . . . . .	152
7.7	Leading Order Performance . . . . .	153
7.8	Systematic Errors . . . . .	156
7.9	NLO cross-section . . . . .	159
7.10	Summary . . . . .	160
<b>8</b>	<b>Summary</b>	<b>162</b>
	<b>References</b>	<b>164</b>

# List of Figures

2.1	QED one loop corrections . . . . .	10
2.2	$e^-e^-$ one loop scattering diagram . . . . .	12
2.3	Scalar field potential . . . . .	14
2.4	Complex scalar field potential . . . . .	16
2.5	Standard Model Higgs coupling to the electron . . . . .	21
3.1	Higgs production diagrams . . . . .	28
3.2	Higgs production as a function of $m_H$ . . . . .	29
3.3	Higgs decay modes . . . . .	30
3.4	Higgs discovery significance as a function of $m_H$ . . . . .	33
4.1	ATLAS Detector . . . . .	37
4.2	Muon spectrometer . . . . .	40
4.3	Hadronic and electromagnetic calorimeters . . . . .	42
4.4	Inner tracking detector . . . . .	45
4.5	Cross section of the ID . . . . .	47
4.6	ID barrel . . . . .	50
5.1	Track helix parameters . . . . .	65
5.2	$p_T$ resolution for 200 and 20 GeV $p_T$ tracks . . . . .	67
5.3	$p_T$ resolution for 5 and 1 GeV $p_T$ tracks . . . . .	67
5.4	Track $\phi$ resolution . . . . .	68
5.5	Track $\cot(\theta)$ resolution . . . . .	69
5.6	$z$ perigee resolution with two detection planes . . . . .	71
5.7	The barrel region of the ID . . . . .	73
5.8	Track $d_0$ resolution as a function of $ \eta $ . . . . .	74
5.9	Track $z_0$ resolution as a function of $ \eta $ . . . . .	74
5.10	Pixel Clustering . . . . .	76
5.11	$\sigma(d_0)$ , $p_T = 200$ GeV . . . . .	77
5.12	$\sigma(d_0)$ , $p_T = 1$ GeV . . . . .	78
5.13	$\sigma(z_0)$ , $p_T = 200$ GeV . . . . .	79
5.14	$\sigma(z_0)$ , $p_T = 1$ GeV . . . . .	80

5.15	$\sigma(z_0) \sin \theta, p_T = 200 \text{ GeV}$ . . . . .	81
5.16	$\sigma(z_0) \sin \theta, p_T = 1 \text{ GeV}$ . . . . .	81
5.17	$d_0$ resolution as a function of $p_T$ . . . . .	82
5.18	$z_0$ resolution as a function of $p_T$ . . . . .	82
6.1	Higgs decay . . . . .	86
6.2	Significance distribution for tracks from $b, c, u$ and gluon jets .	88
6.3	Fraction of tracks as a function of the number of total hits, unique hits, wrong hits and spoilt hits on the track . . . . .	93
6.4	Primary tracks reconstruction efficiency as a function of $ \eta $ . .	94
6.5	Fraction of fake tracks as a function of $ \eta $ . . . . .	94
6.6	Fraction of secondary tracks as a function of $ \eta $ . . . . .	95
6.7	Primary track reconstruction efficiency after selection cuts . .	96
6.8	Fraction of fake tracks after selection cuts . . . . .	97
6.9	Fraction of secondary tracks after selection cuts . . . . .	98
6.10	Jet weight distribution . . . . .	99
6.11	$u, c$ and gluon jet rejection as a function of $b$ -jet efficiency . .	99
6.12	$u, c$ and gluon jet rejection as a function of $ \eta $ with no mis- alignment . . . . .	100
6.13	$u$ -jet rejection as a function of $ \eta $ with misalignment . . . . .	102
6.14	Calorimeter energy reconstruction . . . . .	104
6.15	3+4 layout schematic . . . . .	105
6.16	2+4 layout schematic . . . . .	106
6.17	3+3 layout schematic . . . . .	107
6.18	$u$ -jet rejection as function of $b$ -tagging efficiency . . . . .	109
6.19	$u$ -jet rejection for 50% $b$ -tagging efficiency as a function of $ \eta $	109
6.20	$u$ -jet rejection for 97% and 90% detector efficiency . . . . .	111
6.21	Primary track efficiency for $e_b = 0.5$ . . . . .	113
6.22	Secondary track efficiency for $e_b = 0.5$ . . . . .	114
6.23	Fake track efficiency for $e_b = 0.5$ . . . . .	114
6.24	Pre B-layer secondary track-rate, $e_b = 0.5$ . . . . .	115
6.25	Post B-layer secondary track-rate, $e_b = 0.5$ . . . . .	116
7.1	$t\bar{t}H$ production diagram . . . . .	121
7.2	Jet $p_T$ . . . . .	123
7.3	Jet $\eta$ . . . . .	123
7.4	Jet energy . . . . .	124
7.5	Jet multiplicity . . . . .	124
7.6	$b$ -jet multiplicity . . . . .	125
7.7	Invariant $m_{bb}$ mass . . . . .	128
7.8	$b$ -jet angular separation . . . . .	130

---

7.9	$m_{bb}$ using angular separation . . . . .	131
7.10	$W \rightarrow l\nu$ reconstruction . . . . .	135
7.11	$W \rightarrow jj$ reconstruction . . . . .	136
7.12	Top mass reconstruction . . . . .	137
7.13	Higgs mass reconstruction . . . . .	139
7.14	$b$ -jet characteristics for $t\bar{t}Z$ . . . . .	143
7.15	Jet characteristics for semi irreducible backgrounds . . . . .	145
7.16	Jet characteristics for $WW + \text{jets}$ and $WZ + \text{jets}$ . . . . .	146
7.17	Jet characteristics for reducible backgrounds . . . . .	148
7.18	$m_{b\bar{b}}$ for signal plus background . . . . .	155
7.19	Significance as a function of mass . . . . .	157
7.20	Significance with NLO corrections as a function of $m_H$ . . . . .	161

# List of Tables

2.1	Gauge bosons of the Standard Model . . . . .	6
2.2	Fundamental fermions of the Standard Model . . . . .	7
3.1	Cross-sections for selected processes at LHC . . . . .	26
4.1	ID parameters and measurement resolutions . . . . .	48
4.2	ID pixel barrel parameters . . . . .	49
4.3	End-cap pixel ring parameters . . . . .	51
4.4	End-cap pixel ring parameters . . . . .	51
4.5	SCT barrel layer parameters . . . . .	52
4.6	End-Cap SCT ring parameters . . . . .	53
4.7	End-Cap SCT wheel parameters . . . . .	54
6.1	$b$ -tagging rejection factors . . . . .	100
6.2	Residual module misalignments . . . . .	101
6.3	$u$ -jet rejection for 50% $b$ -tagging efficiency . . . . .	110
6.4	Track finding rates and efficiencies . . . . .	112
7.1	$p_t$ correction factors for $R_u$ and $R_c$ . . . . .	120
7.2	Event characteristics . . . . .	126
7.3	Angular separation cuts . . . . .	133
7.4	Reconstruction Performance . . . . .	140
7.5	Process cross-sections . . . . .	141
7.6	Event rate as a function of $e_b$ . . . . .	149
7.7	Event rate as a function of $p_T$ cut . . . . .	150
7.8	Event rate as a function of $\eta$ cut . . . . .	151
7.9	Event rate for optimum cuts . . . . .	152
7.10	Significances for reconstruction methods . . . . .	153
7.11	Signal significance for $m_H = 80, 100, 120$ GeV . . . . .	156
7.12	Background changes with jet energy scale . . . . .	158
7.13	Signal changes with small $e_b$ differences . . . . .	159
7.14	Signal significance using NLO cross-sections . . . . .	160

# Chapter 1

## Introduction

The Standard Model (SM) of particle physics has successfully explained all experimental observations from the current generation of high energy particle accelerators. In the SM particles acquire mass by spontaneous symmetry breaking, through a process known as the Higgs mechanism. As part of this process a new spin 0 particle is introduced, the Higgs boson, which has yet to be observed experimentally. The mass of the Higgs boson is not predicted by the SM. Experimental constraints rule out a Higgs mass below 109.7 GeV [1] and theoretical arguments indicate that the Higgs mass should be less than 1 TeV.

The Large Hadron Collider (LHC) accelerator being built at the European Laboratory for Particle Physics (CERN), on the French Swiss border, is expected to become operational in 2005, and will provide an excellent opportunity to discern the predicted Higgs boson. The LHC will collide two beams of protons each with an energy of 7 TeV. Four detectors are planned: ATLAS (A Toroidal LHC Apparatus), CMS (Compact Muon Solenoid), LHCb and ALICE (A Large Ion Collider Experiment). ATLAS and CMS are general purpose detectors, LHCb is dedicated to  $b$ -quark physics and ALICE is

dedicated to heavy ion physics.

This thesis is concerned with the Inner Detector (ID) of the ATLAS experiment. The conditions in the ATLAS detector are experimentally difficult. Proton bunches will cross in the detector centre once every 25 ns with a total inelastic  $pp$  interaction cross section of  $\simeq 80$  mb. This gives an expected 23 interactions per bunch crossing at the design luminosity of  $10^{34}\text{cm}^{-2}\text{s}^{-1}$ . This generates a large background of ‘minimum bias events’ superimposed on any physically interesting events making event/track reconstruction within the detector challenging. The large number of particles in the inner detector per event also leads to a very high radiation environment.

The ID provides the ATLAS detector with the primary method of differentiating between, or tagging, particle jets originating from  $b$ -quarks and from non  $b$ -quarks. This is done by measuring the impact parameter of tracks in a jet. Tracks in jets from  $b$ -quarks tend to have high impact parameters compared to jets from non  $b$ -quarks.

In a search for the Higgs boson  $b$ -tagging is of primary importance at the low end of the possible Higgs mass range, where the Higgs decays primarily to  $b\bar{b}$ . Tagging is used to identify the signal from the large background of events with light quark jets, which is orders of magnitude higher in cross-section than the signal.

Chapter 2 discusses the theoretical background of the Standard Model, with particular attention to spontaneous symmetry breaking and the Higgs mechanism. Chapter 3 describes the Higgs production and decay modes expected at the LHC. Chapter 4 describes the geometry and layout of the ATLAS detector in general and provides a more detailed description of the inner tracking detector. Chapter 5 describes the response of the ID to single particles. In Chapter 6 the identification of hadronic jets of particles is

examined. The jets are identified using impact parameter measurements, as originating either from a  $b$ -quark or not. The performance of three different ID layouts are compared in terms of  $b$ -tagging performance. Chapter 7 describes how the  $b$ -tagging of jets is used to examine a particular Higgs production channel of associated production with  $t\bar{t}$ . The analysis focuses on the problem of identifying which  $b$ -jets in a given event come from top quark decays and which from the Higgs boson decay. The significance of the signal is determined as a function of Higgs mass. Finally, Chapter 8 provides conclusions and closing remarks.

# Chapter 2

## Theory

### 2.1 Introduction

This chapter introduces the fundamental interactions of matter and the Standard Model (SM) of particle physics. After a brief description of Quantum Electrodynamics (QED) and Quantum Chromodynamics (QCD), the Higgs mechanism for mass generation is described.

### 2.2 Fundamental Interactions

There are four types of interaction that are sufficient to explain all currently observed phenomena in physics. These are gravitation, electromagnetism, weak and strong interactions. For high energy particle physics, where typically particle masses are  $O(10^{-27})$  kg, the gravitational force is so weak as to have no significant effect on elementary particle interactions. The dominant force on charged particles down to  $10^{-15}$  m is the electromagnetic interaction, which is responsible for the binding forces between atoms and between molecules, and is described by QED.

The weak interaction mediates many particle decays, for example nuclear  $\beta$  decay and all neutrino interactions. The theory of electromagnetic and weak interactions can be unified into one electroweak theory as proposed by Glashow, Salam and Weinberg [2].

The strong interaction accounts for the binding of particles in nuclei, the confinement of quarks in hadrons and gives rise to the large number of observed hadrons. Quarks and gluons directly feel the strong force which is described by QCD.

The unified electroweak theory and QCD together form the basis of the SM of particle physics. The success of the SM is such that so far no experimental contradictions have been found. However the SM is not complete and some experiments have indicated that extensions are required. For example the solar neutrino detector Super Kamiokande [3] has inferred a non zero mass value for the neutrino. Also the SM does not explain why there are three generations of quarks and leptons, when only one generation is required to make up the ordinary visible matter of the universe. In addition the Higgs particle, required by the SM process for generating the boson masses and by Yukawa coupling, the lepton and intrinsic quark masses has yet to be found experimentally. The search for the Higgs particle is a major motivation for building the LHC.

## 2.3 The Standard Model

The SM is a gauge theory which describes the electromagnetic, weak and strong interactions. The model has been described in detail in many textbooks and review articles, see [4, 5, 6]. The three forces described by the SM are each mediated by spin 1 particles called gauge bosons. Table 2.1 lists

Interaction	Boson	Mass (GeV)	Charge (e)	Typical cross-section (mb)	Relative Strength
Strong	gluon	0	0	10	1
Electromagnetic	$\gamma$	0	0	$10^{-3}$	$10^{-2}$
Weak	$W^\pm$	$80.419 \pm 0.056$	$\pm 1$	$10^{-11}$	$10^{-6}$
	$Z^0$	$91.1882 \pm 0.0022$	0		

Table 2.1: The interactions and corresponding gauge bosons of the Standard Model. The masses of the  $W^\pm$  and  $Z^0$  are from [8].

the bosons corresponding to each interaction, the typical cross-section and relative strength of each interaction.

The fundamental fermions are spin  $\frac{1}{2}$  particles, divided up into leptons, which interact electromagnetically and weakly, and quarks which also interact strongly. The fermions are grouped into three families as shown in Table 2.2. In addition each fermion has a corresponding anti-particle, with the same mass and spin but opposite charge.

In the SM, quarks and leptons are true elementary particles with no internal structure, size or excited states. Nuclei, atoms and molecules are all built up out of the first family of fermions. The second and third families have an identical structure and differ from the first family only in mass and flavour. In the minimal SM a single additional scalar particle is predicted, responsible for mass generation, the Higgs boson  $H$ .

## 2.4 Standard Model Dynamics

QED describes the electromagnetic interaction, between charged fermions and photons. The QED Lagrangian consists of three parts, the Dirac La-

Family	Leptons			Quarks		
	Flavour	Charge (e)	Mass (GeV)	Flavour	Charge (e)	Mass (GeV)
1st	$\nu_e$	0	$< 5 \cdot 10^{-9}$	u	2/3	$7 \cdot 10^{-3}$
	$e$	-1	$5.11 \cdot 10^{-4}$	d	-1/3	$15 \cdot 10^{-3}$
2nd	$\nu_\mu$	0	$< 0.3 \cdot 10^{-3}$	c	2/3	1.3
	$\mu$	-1	$1.06 \cdot 10^{-1}$	s	-1/3	0.2
3rd	$\nu_\tau$	0	$< 0.03$	t	2/3	175
	$\tau$	-1	1.777	b	-1/3	4.8

Table 2.2: The fundamental fermions of the Standard Model. The masses given here for the  $u$ ,  $d$  and  $s$  quarks are intrinsic masses and all masses are from [8].

grangian for a fermion field  $\psi$ , the Maxwell Lagrangian for the electromagnetic vector potential  $A_\mu$  and an interaction term between photons and fermions. The QED Lagrangian has the form

$$\mathcal{L} = \bar{\psi}(i\partial_\mu\gamma^\mu - m)\psi - \frac{1}{4}F_{\mu\nu}F^{\mu\nu} - q\bar{\psi}\gamma_\mu A^\mu\psi \quad (2.1)$$

where  $m$  is the fermion mass,  $q$  is the fermion charge and  $F_{\mu\nu} = \partial_\mu A_\nu - \partial_\nu A_\mu$ . The first term represents the fermion field, the second the photon potential and the third the interaction term. The theory is Abelian (i.e. the group elements commute) and is based on the group U(1).

QCD describes the strong interaction, between spin  $\frac{1}{2}$  quarks and spin 1 gluons. It is a non-Abelian (i.e. group elements do not commute) gauge theory based on the group SU(3). The fundamental differences between QCD and QED are the appearance in QCD of interaction terms between only gluons and the three colour charges of QCD as opposed to the positive and negative charges in QED. (The photon in QED has no electric charge,

however gluons have the colour charge of QCD.) This difference underlies the confinement of quarks into hadrons and the decreasing strength of the strong coupling with increasing energy scale.

The QCD Lagrangian consists of a Dirac Lagrangian for a fermion field  $\psi$ , gluon potential  $A_\mu^a$  and an interaction term between gluons and fermions. The Lagrangian has the form

$$\mathcal{L} = -\frac{1}{4}G_{\mu\nu}^a G^{a\mu\nu} + \bar{\psi}(i\partial_\mu\gamma^\mu - m)\psi - ig\bar{\psi}A_\mu^a\gamma^\mu T^a\psi \quad (2.2)$$

where  $m$  is the intrinsic quark mass,  $g$  the quark gluon coupling constant,  $a$  is a colour label, running from 1 to 8 for SU(3) and  $T^a$  are a set of eight independent Hermitian traceless  $3 \times 3$  matrices. The gluon field strength tensor  $G_{\mu\nu}^a$  is

$$\partial_\mu A_\nu^a - \partial_\nu A_\mu^a + gf^{abc}A_\mu^b A_\nu^c \quad (2.3)$$

where  $f^{abc}$  are the structure constants of SU(3) and the third term in the gluon field strength represents the gluon gluon interactions.

In QCD hadrons are formed from quarks, bound by colour interactions into colour singlet states, either as three-quark baryons or quark-anti-quark pairs forming mesons. The binding energy of a quark in a hadron is infinite, hence free quarks are not observed. However as the coupling strength decreases at high energies, quarks inside hadrons can behave in many ways as free particles, for example in Deep Inelastic Scattering [7].

Weak interactions act on the flavour degrees of freedom of quarks and between leptons in the same family. If weak interactions were distinct from QED interactions then a new ‘quantum flavourdynamics’ acting on the lepton types and quark flavours would be introduced. However this is not the case, the weak and electromagnetic interactions are linked together.

The electroweak interactions are based on the gauge group  $SU(2)_L \otimes U(1)_Y$ , where the groups  $SU(2)_L$  and  $U(1)_Y$  refer to the weak isospin and the weak hypercharge. The  $L$  denotes that the  $SU(2)$  part acts only on the left-handed parts of the fermion fields. The gauge boson mediating the weak interactions are the charged  $W^\pm$  and the neutral  $Z^0$ . Charged current interactions, due to the exchange of a  $W^\pm$ , are responsible for nuclear  $\beta$  decay and muon decay ( $\mu^- \rightarrow e^- + \bar{\nu}_e + \nu_\mu$ ). Weak neutral current interactions (such as electron-neutrino scattering) are due to the  $Z^0$ .

The  $Z^0$  couples only to quarks or leptons within the same family, i.e. there are no flavour-changing neutral currents. The  $W^\pm$  also couples to leptons only in the same family. However for quarks the  $W^\pm$  couples not to the quark mass eigenstates  $q$  but to linear combinations  $q'$ . This allows for quark decays such as  $s \rightarrow u + W^-$  and  $b \rightarrow c + W^-$ . This mixing can be described by the Cabibbo-Kobayashi-Maskawa mixing matrix [9]

$$\begin{pmatrix} d' \\ s' \\ b' \end{pmatrix} = \begin{pmatrix} V_{ud} & V_{us} & V_{ub} \\ V_{cd} & V_{cs} & V_{cb} \\ V_{td} & V_{ts} & V_{tb} \end{pmatrix} \begin{pmatrix} d \\ s \\ b \end{pmatrix} \quad (2.4)$$

where  $V_{ij}$  are numerical values giving the size of the mixing between two quarks.

All the gauge theories of the SM are renormalisable, that is divergences introduced by adding additional loop diagrams to a calculation (Figure 2.1) can be cancelled by rescaling the fields, masses and couplings in the original Lagrangian. For example the charge on the electron is replaced by a ‘bare’ electronic charge  $e_0 = e + \Delta e$ . The calculation of  $\Delta e$  is non-trivial and increases in complexity as more loops are added to diagrams. Without renormalisation the divergences introduced by loop diagrams would mean that no measurable physical quantities could be calculated.

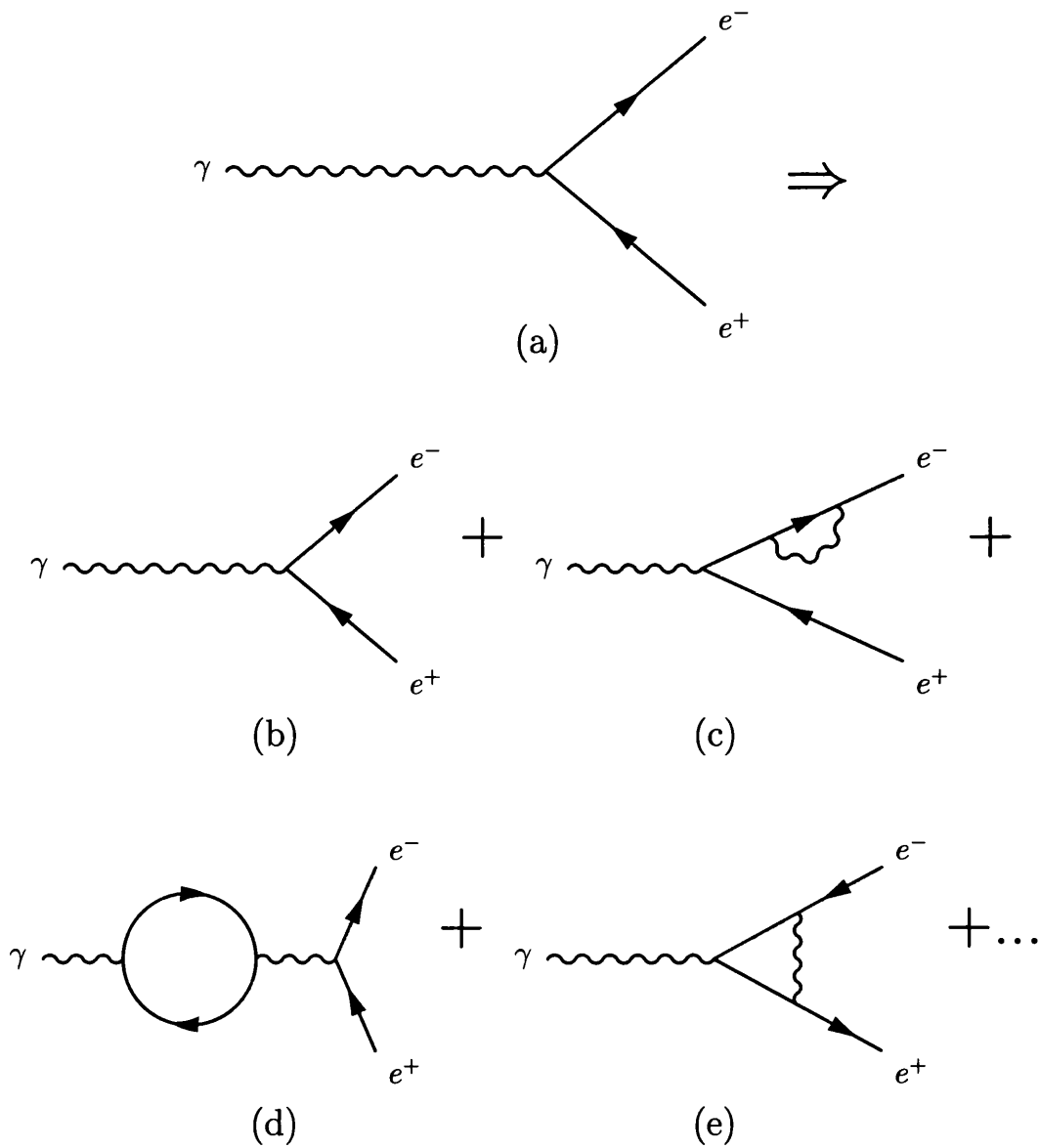


Figure 2.1: Vertex renormalisation in QED, to the one loop level. (a) shows the Feynman diagram for electron positron pair production. At the one loop level of corrections this diagram is replaced by the original diagram (b) plus a correction for the self energy of the electron (and a similar correction for the self energy of the positron) (c), the self energy of the photon (d) and a vertex correction (e).

## 2.5 The Higgs Mechanism

The term *mass* in high energy physics can refer to several different types of masses. The spontaneous breaking of the SU(2) symmetry in the Higgs mechanism gives rise to the mass of the  $W^\pm$  and  $Z^0$  bosons. The intrinsic masses of the leptons and quarks are then generated in the SM by Yukawa couplings between a fermion and the Higgs boson. The masses of the hadrons arise partly from the intrinsic quark masses and partly from the QCD interactions that form the hadrons.

Electroweak theory has four gauge bosons which, without any additions, gives rise to four massless gauge bosons. Physically the photon is massless however the  $W^\pm$  and  $Z^0$  have mass of the order of 100 GeV. Simply adding mass terms for the  $W^\pm$  and  $Z^0$  to the Lagrangian would violate the gauge symmetry, which is required if the theory is to be renormalisable and therefore predictive.

For example in Figure 2.2 ( $e^-e^-$  scattering at the 1 loop level) both the photon and  $Z^0$  can propagate in the loop. The momentum around the loop may take any value so the amplitude is of the form  $\int \partial^4 q$  (propagators). In the case of a photon in the loop then the integral becomes  $\int \partial^4 q \Delta_e \Delta_e \Delta_\gamma \Delta_\gamma$  where  $\Delta$  represents the propagators for the electron and photon. At high  $q^2$  the electron propagator goes as  $1/q$  and the photon propagator goes as  $1/q^2$ . Hence the integral becomes  $\int \partial^4 q \frac{1}{q^6}$  which is convergent, however for the  $Z^0$  the propagator is

$$i \frac{-g_{\mu\nu} + q_\mu q_\nu / M^2}{q^2 - M^2} \quad (2.5)$$

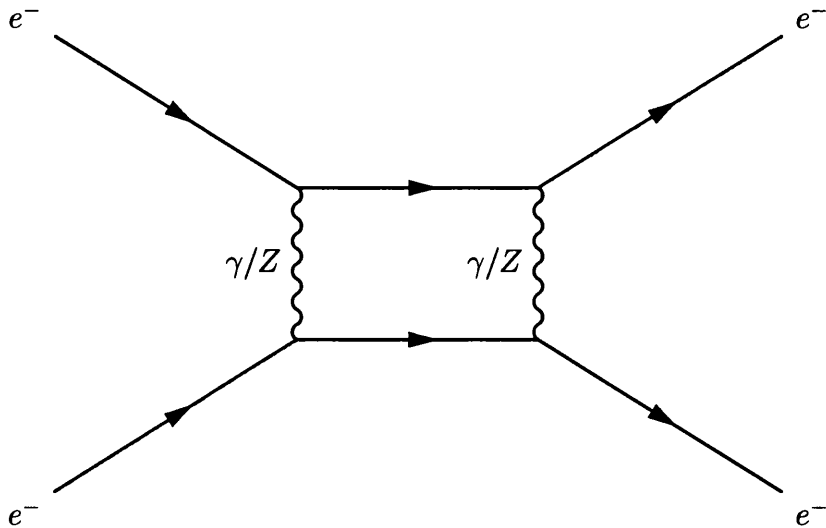


Figure 2.2: A one loop Feynman diagram for  $e^-e^-$  scattering.

where  $M$  is the  $Z^0$  mass, and  $q^\mu$  the  $Z^0$  four momentum, which becomes

$$i \frac{q_\mu q_\nu}{q^2 M^2} \quad (2.6)$$

at high  $q^2$ . Therefore the integral for the  $Z^0$  propagator would become  $\int \partial^4 q \frac{1}{q^4}$  which is logarithmically divergent. Counter-terms can be added to the Lagrangian to cancel the divergence in the integral, however high-order diagrams with more loops would introduce an infinite number of divergences requiring an infinite number of counter-terms. The theory would become non-renormalisable and be unable to give any predictions. The  $W^\pm$  and  $Z^0$  masses cannot be added in ‘by hand’ however the masses can be generated consistently using the Higgs mechanism [10].

To introduce the Higgs mechanism consider, a simple world of scalar particles [4], ignoring gauge fixing terms, with the Lagrangian

$$\mathcal{L} = \frac{1}{2}(\partial_\mu \phi)^2 - \frac{1}{2}\mu^2 \phi^2 - \frac{1}{4}\lambda \phi^4 \quad (2.7)$$

where  $\phi$  is the scalar particle field, the first term is the particle kinetic energy ( $T$ ), the second and third terms are the potential energy ( $V$ ) made up from the particle mass term (second term) and a four particle vertex with coupling  $\lambda$  (third term). With  $\lambda > 0$  there are two possible forms of the potential as shown in Figure 2.3 depending on the sign of  $\mu^2$ . With  $\mu^2 > 0$  the Lagrangian describes a scalar particle with mass  $\mu$  (the  $\mu^2\phi^2$  term). The ground state corresponds to  $\phi = 0$ . In the second case, where  $\mu^2 < 0$ , there is a mass term of the wrong sign for the field  $\phi$ . The potential has two minima which satisfy

$$\frac{dV}{d\phi} = \phi(\mu^2 + \lambda\phi^2) = 0 \quad (2.8)$$

and are therefore at  $\phi = \pm v$  with  $v = \sqrt{-\mu^2/\lambda}$ . The energy minimum is moved from  $\phi = 0$  and hence the physical states sit at this minimum. Perturbative calculations should therefore use expansions about  $\phi = \pm v$ , so

$$\phi(x) = v + \eta(x). \quad (2.9)$$

Substituting this back into the Lagrangian gives

$$\mathcal{L}' = \frac{1}{2}(\partial_\mu\eta)^2 - \lambda v^2\eta^2 - \lambda v\eta^3 - \frac{1}{4}\lambda\eta^4 + \text{const.} \quad (2.10)$$

This gives a mass term ( $\lambda v^2\eta^2$ ) for the field  $\eta$  with  $m_\eta = \sqrt{2\lambda v^2} = \sqrt{-2\mu^2}$  with the correct sign as well as a triple scalar vertex ( $\lambda v\eta^3$ ). The higher order terms represent the interaction of the  $\eta$  field with itself.

The two Lagrangians  $\mathcal{L}$  and  $\mathcal{L}'$  must describe the same physics. However  $\mathcal{L}$  cannot be solved perturbatively whereas the perturbative solutions of  $\mathcal{L}'$  give the correct physical picture. This way of ‘generating’ mass is referred to as ‘spontaneous symmetry breaking’.

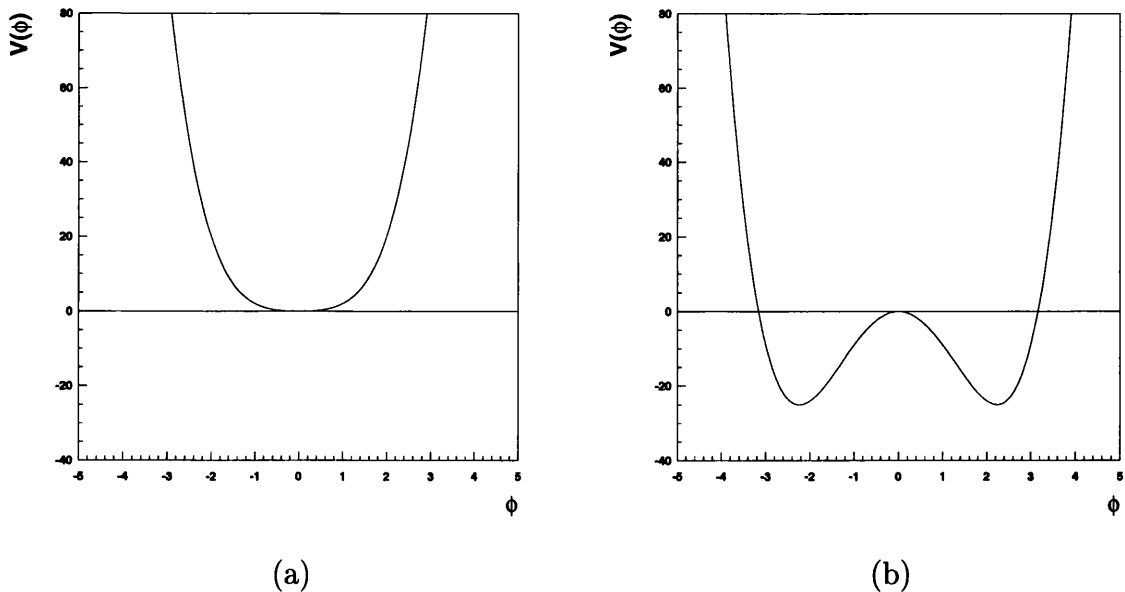


Figure 2.3: The potential  $V(\phi) = \frac{1}{2}\mu^2\phi^2 + \frac{1}{4}\lambda\phi^4$  for (a)  $\mu^2 > 0$  and (b)  $\mu^2 < 0$  with  $\lambda > 0$  in both cases.

Next, consider a complex scalar field, which will lead to massive vector particles,  $\phi = (\phi_1 + i\phi_2)/\sqrt{2}$  with the Lagrangian

$$\mathcal{L} = (\partial_\mu \phi)^* (\partial^\mu \phi) - \mu^2 \phi^* \phi - \lambda (\phi^* \phi)^2 \quad (2.11)$$

The Lagrangian possesses a  $U(1)$  global gauge symmetry, i.e. it is invariant under a global phase change,  $\phi \rightarrow e^{i\alpha}\phi$ . As in the case of the scalar field, if  $\lambda > 0$  and  $\mu^2 < 0$ , the potential minimum is not at the origin. Substituting  $\phi = (\phi_1 + i\phi_2)/\sqrt{2}$  for  $\phi$  gives

$$\mathcal{L} = \frac{1}{2}(\partial_\mu \phi_1)^2 + \frac{1}{2}(\partial_\mu \phi_2)^2 - \frac{1}{2}\mu^2(\phi_1^2 + \phi_2^2) - \frac{1}{4}\lambda(\phi_1^2 + \phi_2^2)^2 \quad (2.12)$$

The potential  $V(\phi) = -\frac{1}{2}\mu^2(\phi_1^2 + \phi_2^2) - \frac{1}{4}\lambda(\phi_1^2 + \phi_2^2)^2$  now has, in the  $\phi_1, \phi_2$

plane, a circle of minima of radius  $v$  with

$$v^2 = \phi_1^2 + \phi_2^2 = -\frac{\mu^2}{\lambda} \quad (2.13)$$

as can be seen in Figure 2.4. Again the Lagrangian can be expanded about a particular vacuum point, chosen to be  $\phi = \sqrt{\mu^2/2\lambda} \equiv v/\sqrt{2}$ , in terms of new fields by substituting

$$\phi(x) = \sqrt{\frac{1}{2}}[v + \eta(x) + i\zeta(x)] \quad (2.14)$$

where  $\eta$  and  $\zeta$  are the new fields. This gives

$$\mathcal{L}' = \frac{1}{2}(\partial_\mu\zeta)^2 + \frac{1}{2}(\partial_\mu\eta)^2 - \nu^2\lambda\eta + \dots \quad (2.15)$$

with additional constant terms and cubic and quartic terms in  $\eta$  and  $\zeta$ . The term  $\nu^2\lambda\eta$  is in the form of a mass term for the  $\eta$  field with a mass of  $\sqrt{2\nu^2\lambda}$ . However there is no corresponding mass term of the  $\zeta$  field, i.e. the theory contains a massless scalar particle, known as a Goldstone Boson.

This Goldstone Boson will disappear if, instead of a global gauge symmetry, a local gauge symmetry is considered. To make the Lagrangian given in 2.11 invariant under a  $U(1)$  local gauge transformation,  $\phi \rightarrow e^{i\alpha(x)}\phi$ , requires  $\partial_\mu$  to be replaced by  $D_\mu = \partial_\mu - ieA_\mu$ , where the gauge field transforms as  $A_\mu \rightarrow A_\mu + \frac{1}{e}\partial_\mu\alpha$ . The Lagrangian then becomes

$$\mathcal{L} = (\partial^\mu + ieA^\mu)\phi^*(\partial_\mu + ieA_\mu)\phi - \mu^2\phi^*\phi - \lambda(\phi^*\phi)^2 - \frac{1}{4}F_{\mu\nu}F^{\mu\nu} \quad (2.16)$$

Again taking  $\mu^2 < 0$  and translating the field  $\phi$  to a true ground state the Lagrangian becomes

$$\begin{aligned} \mathcal{L}' = & \frac{1}{2}(\partial_\mu\zeta)^2 + \frac{1}{2}(\partial_\mu\eta)^2 - \nu^2\lambda\eta^2 + \frac{1}{2}e^2v^2A_\mu A^\mu - evA_\mu\partial^\mu\zeta \\ & - \frac{1}{4}F_{\mu\nu}F^{\mu\nu} + \text{interaction terms} \end{aligned} \quad (2.17)$$

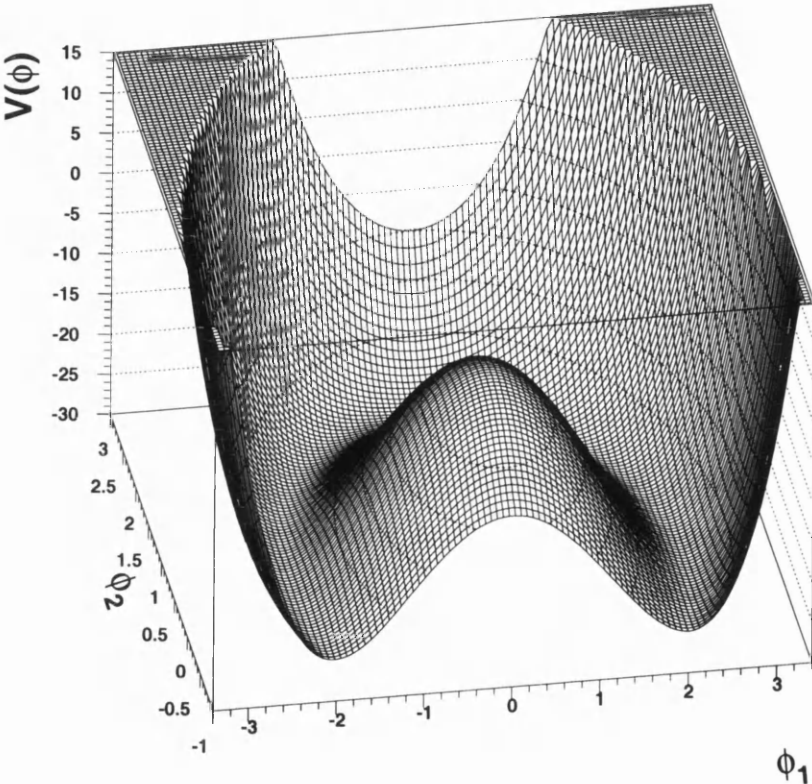


Figure 2.4: The potential  $V(\phi)$  for a complex scalar field for the case  $\mu^2 < 0$  and  $\lambda > 0$ .

The Lagrangian  $\mathcal{L}'$  now appears to have a massless Goldstone boson  $\zeta$ , a massive scalar  $\eta$  and a massive vector  $A_\mu$  where,  $m_\zeta = 0$ ,  $m_\eta = \sqrt{2\lambda v^2}$  and  $m_A = ev$ . However by giving mass to  $A_\mu$  its polarisation degrees of freedom have increased from 2 to 3, as it can now possess longitudinal polarisation. Simply translating field variables cannot create new degrees of freedom, so the fields in  $\mathcal{L}'$  do not all correspond to distinct physical particles. In fact by using a particular gauge transformation the  $\zeta$  field can be eliminated. Substituting a different set of real fields  $h$ ,  $\theta$ ,  $A_\mu$  where,

$$\phi \rightarrow \sqrt{\frac{1}{2}}(v + h(x))e^{i\theta(x)/v} \quad (2.18)$$

$$A_\mu \rightarrow A_\mu + \frac{1}{ev}\partial_\mu\theta \quad (2.19)$$

into the original Lagrangian and choosing  $\theta(x)$  so that  $h$  is real then the Lagrangian becomes

$$\begin{aligned} \mathcal{L}'' = & \frac{1}{2}(\partial_\mu h)^2 - \lambda v^2 h^2 + \frac{1}{2}e^2 v^2 A_\mu^2 - \lambda v h^3 - \frac{1}{4}\lambda h^4 + \frac{1}{2}e^2 A_\mu^2 h^2 \\ & + ve^2 A_\mu^2 h - \frac{1}{4}F_{\mu\nu}F^{\mu\nu} \end{aligned} \quad (2.20)$$

which is independent of  $\theta$  and the Goldstone boson does not appear.

The apparent extra degree of freedom is spurious, as it is only the freedom to make a gauge transformation. This Lagrangian describes two massive interacting particles, a vector gauge boson  $A_\mu$  and a massive scalar  $h$ , which is called a Higgs boson. The Goldstone boson has been ‘absorbed’ into the gauge boson in the form of its additional freedom corresponding to longitudinal polarisation. This is the basic form of the Higgs mechanism to generate massive vector bosons.

The spontaneous breaking of a  $U(1)$  gauge symmetry can be generalised to a non-Abelian theory [11, 12]. The aim is to find a Higgs sector which will break  $SU(2)_L \otimes U(1)_Y$  to  $U(1)_{em}$ .

From the Lagrangian

$$\mathcal{L} = (\partial_\mu \phi)^\dagger (\partial^\mu \phi) - \mu^2 \phi^\dagger \phi - \lambda (\phi^\dagger \phi)^2 \quad (2.21)$$

where  $\phi$  is a complex  $SU(2)_L$  doublet with hypercharge  $Y = 1$ , the simplest choice to maintain local gauge invariance is to replace  $\partial_\mu$  with the covariant derivative

$$D_\mu = \partial_\mu + igT^A W_\mu^A + \frac{ig'}{2} Y B_\mu \quad (2.22)$$

The Lagrangian then becomes

$$\mathcal{L}_{Higgs} = (D_\mu \phi)^\dagger (D_\mu \phi) + \mu^2 \phi^\dagger \phi + \lambda (\phi^\dagger \phi)^2 \quad (2.23)$$

As charge is equal to the sum of the third component of weak isospin and half the hypercharge,  $Q = T_3 + Y/2$  then the charge assignment for  $\phi$  is,

$$\phi = \begin{pmatrix} \phi^+ \\ \phi^0 \end{pmatrix} \quad (2.24)$$

To maintain charge conservation only the  $\phi^0$  should get a vacuum expectation value. This motivates rewriting  $\phi$  in terms of two new fields  $\chi^A$  and  $H$ , both of which are real

$$\phi = \frac{1}{\sqrt{2}} e^{i\frac{1}{v} T^A \chi^A} \begin{pmatrix} 0 \\ v + H \end{pmatrix} \quad (2.25)$$

where  $v^2$  is chosen to be  $\frac{\mu^2}{\lambda}$  to give a minimum at  $H = 0$ . The potential is

$$V(H) = -\frac{1}{2}\mu^2(v + H)^2 + \frac{\lambda}{4}(v + H)^4. \quad (2.26)$$

Substituting into  $\mathcal{L}_{Higgs}$  gives

$$\phi = \frac{1}{\sqrt{2}}U \begin{pmatrix} 0 \\ v + H \end{pmatrix} \quad (2.27)$$

where  $U$  is an  $SU(2)_L$  gauge transformation. As the Lagrangian is gauge invariant it cannot depend on  $U$  which can be absorbed into a redefinition of the gauge field so that in the ‘unitary gauge’ the Lagrangian has the form

$$\mathcal{L}_{Higgs} = (D_\mu\phi)^\dagger(D_\mu\phi) + \mu^2\phi^\dagger\phi - V(\phi, \phi^\dagger) \quad (2.28)$$

with

$$\phi = \frac{1}{\sqrt{2}} \begin{pmatrix} 0 \\ v + H \end{pmatrix} \quad (2.29)$$

Again the Goldstone boson fields have disappeared from the particle spectrum, defined by the Lagrangian. The vacuum expectation value for the scalar fields is

$$\langle \phi \rangle = \frac{1}{\sqrt{2}} \begin{pmatrix} 0 \\ v \end{pmatrix} \quad (2.30)$$

The expectation value is not invariant under  $SU(2)_L$  transformations or under  $U(1)_Y$  as  $\phi$  has been assigned  $Y = 1$ . However the expectation value is invariant under  $U(1)_{em}$  transformations as

$$Q \langle \phi \rangle = (T_3 + \frac{1}{2}Y) \langle \phi \rangle = 0 \quad (2.31)$$

So the  $SU(2)_L \otimes U(1)_Y$  group is spontaneously broken to  $U(1)_{em}$  and three Goldstone bosons are generated. The vector bosons  $W^\pm$  and  $Z^0$  absorb the Goldstone bosons, thus acquiring mass, while the photon remains massless as  $U(1)_{em}$  is unbroken. One massive neutral scalar particle is left, the Higgs boson.

Expanding out the Lagrangian the masses of the  $W^\pm$ ,  $Z^0$  and  $H$  are identified as

$$m_W^2 = \frac{1}{4}g^2v^2 \quad (2.32)$$

$$m_Z^2 = \frac{1}{4}(g^2 + g'^2)v^2 = \frac{1}{4} \frac{g^2}{\cos^2\theta_W} m_W^2 \quad (2.33)$$

$$m_H^2 = 2\lambda v^2 \quad (2.34)$$

As the parameters  $v$  and  $\lambda$  are free then the mass of the Higgs boson is not predicted.

Masses for the fermions can also be generated using the Higgs boson using Yukawa couplings. Figure 2.5 shows the Higgs coupling to the electron in the SM. In the Lagrangian this is represented by the terms

$$\mathcal{L} = -g_e(\bar{l}_{eL}\phi e_R + \bar{e}_R\phi^\dagger l_{eL}) \quad (2.35)$$

with

$$l_{eL} = \begin{pmatrix} \nu_e \\ e^- \end{pmatrix}_L \quad (2.36)$$

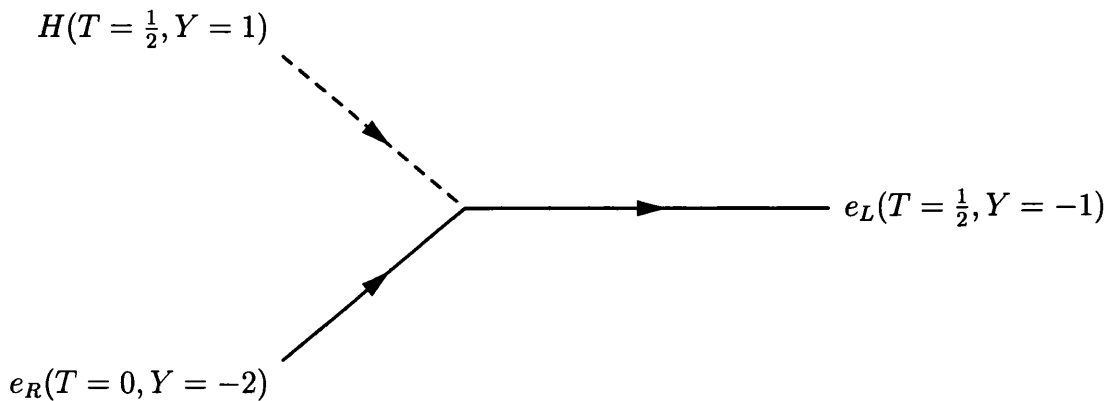


Figure 2.5: The Higgs  $H$  coupling to the electron in the Standard Model.  $T$  is weak isospin,  $Y$  is hypercharge,  $e_R$  is the right handed part of the electron field and  $e_L$  is the left hand part. The Higgs couples equally to the left and right handed fields.

where  $\phi$  is the Higgs field,  $l_{eL}$  is the left handed part of the electron/ $\nu_e$  doublet and  $e_R$  is the right handed singlet component [5].

The Higgs doublet has the correct  $SU(2) \otimes U(1)$  quantum numbers to couple  $e_L e_R$ . Substituting

$$\phi = \frac{1}{\sqrt{2}} \begin{pmatrix} 0 \\ v + H \end{pmatrix} \quad (2.37)$$

into the Lagrangian gives

$$\mathcal{L} = -\frac{g_e}{\sqrt{2}}v(e_L e_R + e_R e_L) - \frac{g_e}{\sqrt{2}}(e_L e_R + e_R e_L)H \quad (2.38)$$

and by choosing  $g_e$  such that

$$m_e = \frac{g_e v}{\sqrt{2}} \quad (2.39)$$

the Lagrangian then becomes

$$\mathcal{L} = -m_e \bar{e}e - \frac{m_e}{v} \bar{e}eH \quad (2.40)$$

As  $g_e$  is arbitrary the mass of the electron is not predicted. The second term is small as  $v = 2^{-1/4} G_F^{-1/2} = 246$  GeV [8] and has not produced a detectable effect in electroweak interactions. The muon and tau are similar however the quark sector is more complicated as both the upper and lower components of the  $SU(2)_L$  doublet acquires a mass. The Higgs mechanism does not account for the masses of the hadrons as these arise from the QCD bindings of the quarks into the hadrons.

## 2.6 Summary

The fundamental interactions and particles of the SM of particle physics have been introduced. The Higgs mechanism to give mass to the  $W^\pm$  and  $Z^0$  boson has been described. In addition the Higgs fields have been shown to allow Yukawa couplings to give fermions mass.

# Chapter 3

## LHC Phenomenology

### 3.1 Introduction

This chapter gives an overview of the expected processes at the LHC. The production processes and decay modes of the SM Higgs are described. Finally associated Higgs production with  $t\bar{t}$  is introduced and a search method is motivated.

### 3.2 LHC Accelerator

The SM Higgs particle has not been found and the ability to find the Higgs, should such a mechanism prove physically correct, is one of the main reasons for building the LHC. In addition to the Higgs the LHC has the potential to find any new physics, such as supersymmetric particles. In supersymmetric theory all known particles have a supersymmetric partner which differs in spin. Spin  $\frac{1}{2}$  fermions have spin 1 partners and spin 1 bosons have spin  $\frac{1}{2}$  partners. Any supersymmetric particles also differ in mass, they must be heavier than the known particles otherwise they would have been detected

already. In addition the LHC will be able to find any new and unexpected physics at these new energy scales.

The centre of mass energy of the electron-positron collider LEP2 is limited by energy loss due to synchrotron radiation, and the highest centre of mass energy currently obtained is 209 GeV [1]. Linear electron-positron colliders have been proposed but will require more investment than circular colliders to achieve TeV centre of mass energies. To reach higher centre of mass energies the LHC will collide protons on protons.

The performance of hadron colliders is limited not by synchrotron radiation but by the strength and cost of the required bending magnets. Each parton in the proton carries only a fraction of the total momentum and hence the centre of mass energy for a hadron collider has to be higher than 1 TeV to give quark and gluon interactions at the TeV scale.

At the TeV energy scale the cross-sections and branching ratios for some of the more interesting processes are very small. In order to observe a sufficient number of events in a reasonable time the LHC requires a high luminosity, and hence a high bunch crossing rate.

The LHC accelerator will collide together two proton beams of 7 TeV energy, to give a centre of mass energy,  $\sqrt{s} = 14$  TeV. The accelerator is to be built in the existing LEP tunnel at CERN and hence will have a circumference of 27 km. The current schedule for the LHC has a 3 year run from 2005 at a luminosity of  $10^{33}$   $\text{cm}^{-2}\text{s}^{-1}$  followed by running at a higher luminosity of  $10^{34}$   $\text{cm}^{-2}\text{s}^{-1}$  for the remaining lifetime of the experiment, around 10 years.

### 3.3 Physics at the LHC

The total cross-section of proton-proton collisions at the LHC is estimated to be  $\sigma_T = 110 \text{ mb} \pm 20 \text{ mb}$  [27]. Of these interactions 26% are calculated to be elastic, leaving an inelastic cross-section of  $\sigma \simeq 80 \text{ mb}$ . The cross-sections are to be compared to interesting signal processes such as the  $b$ -quark production cross-section of  $\sigma_{b\bar{b}} = 500 \mu\text{b}$  or top quark production cross-section of  $\sigma_{t\bar{t}} = 833 \text{ pb}$  [19]. There are significant uncertainties in the process cross-sections due to the lack of higher order corrections, parton density uncertainties, the energy scale for the QCD evolution and the models used by the event generators.

The cross-sections of a selection of processes at the LHC are shown in Table 3.1. For low luminosity running this gives an interaction rate of  $8 \cdot 10^7$  per second and for high luminosity an interaction rate of  $8 \cdot 10^8$  per second. The LHC will produce approximately  $5 \cdot 10^{12}$   $b\bar{b}$  pairs in the first year alone and will allow investigation of decays of the  $B_s$ . The LHC can also be called a ‘top factory’ producing over  $8 \cdot 10^6$   $t\bar{t}$  pairs per year at low luminosity.

### 3.4 Higgs Production

The experimental observation of the Higgs boson is one of the most important physics goals of ATLAS. The SM gives no direct prediction for the mass of the Higgs boson. Experimental constraints from LEP2 directly rule out a Higgs mass below 109.7 GeV [1] and the data favours slightly a Higgs boson with a mass of 115 GeV. High precision electroweak data are also used to indirectly constrain the Higgs mass via their sensitivity to loop corrections. Assuming the validity of the SM, a fit to all the electroweak data gives  $m_H = 80_{-37}^{+60}$  GeV [31]. Theoretical arguments indicate that the Higgs boson should have a

Process	Cross-section
Inclusive $b\bar{b}$ production	500 $\mu\text{b}$
Inclusive $W$ production	140 nb
Inclusive $Z$ production	43 nb
Inclusive $t\bar{t}$ production	833 pb
$WW$	71 pb
$WZ$	26 pb
Inclusive $H$ production, $m_H = 100$ GeV	27.8 pb
$WH$ , $m_H = 100$ GeV	1.87 pb
$t\bar{t}H$ , $m_H = 100$ GeV	1.01 pb

Table 3.1: The expected cross-sections for selected processes at LHC. [19]

mass below 1 TeV. The upper limit of around 1 TeV is obtained from unitarity arguments [25, 26, 28]. When the Higgs mass increases the amplitude for high energy scattering of longitudinal  $W$  bosons, which includes contributions from Higgs exchange diagrams, becomes large. In order that the scattering does not violate unitarity then the Higgs mass must be less than 1 TeV or  $WW$  and  $ZZ$  interactions will show new physics at around the 1 TeV scale.

There is no single production mechanism or decay process [34, 35] which dominates over the potential Higgs mass range (80 GeV to 1 TeV) observable with ATLAS. Instead there are several different discovery scenarios depending on the mass of the Higgs particle.

There are several Higgs production methods at the LHC which have the potential to lead to observable cross-sections. These include:

- gluon-gluon fusion;
- $WW$  and  $ZZ$  fusion;

- associated production with  $W$  and  $Z$  bosons;
- associated production with  $t\bar{t}$ .

Figure 3.1 shows the Feynman diagrams for these production methods.

Figure 3.2 shows a particular calculation of the Higgs production cross-sections at the LHC [32]. The dominant production mode is gluon fusion which is an order of magnitude higher in cross-section than the other production methods for all but the highest masses. However the direct production channels cannot be triggered on by the ATLAS detector for low Higgs mass ( $m_H < 130$  GeV). The  $t\bar{t}H$  production cross-section is lower than given in Table 3.1,  $\simeq 25\%$  less for  $m_H = 100$  GeV. The difference in production cross-sections is due to the lack of precise knowledge of the gluon distribution at small parton momentum  $x$ , which is important for the intermediate mass Higgs, and the effect of NNLO perturbative QCD corrections [33].

### 3.5 Higgs Decay Modes

The decay of the Higgs boson after production depends critically on its mass. The Higgs couples preferentially to heavy particles so the Higgs boson decays primarily into the highest mass particles energetically allowed. The important decay modes for observing the Higgs are [19]:

- $H \rightarrow \gamma\gamma$  direct or associated production;
- $H \rightarrow b\bar{b}$  associated production with  $WH$ ,  $ZH$  and  $t\bar{t}H$ ;
- $H \rightarrow ZZ \rightarrow 4l$  and  $H \rightarrow ZZ \rightarrow ll\nu\nu$ ;
- $H \rightarrow WW \rightarrow l\nu jj$  and  $H \rightarrow ZZ \rightarrow l^+l^-jj$ .

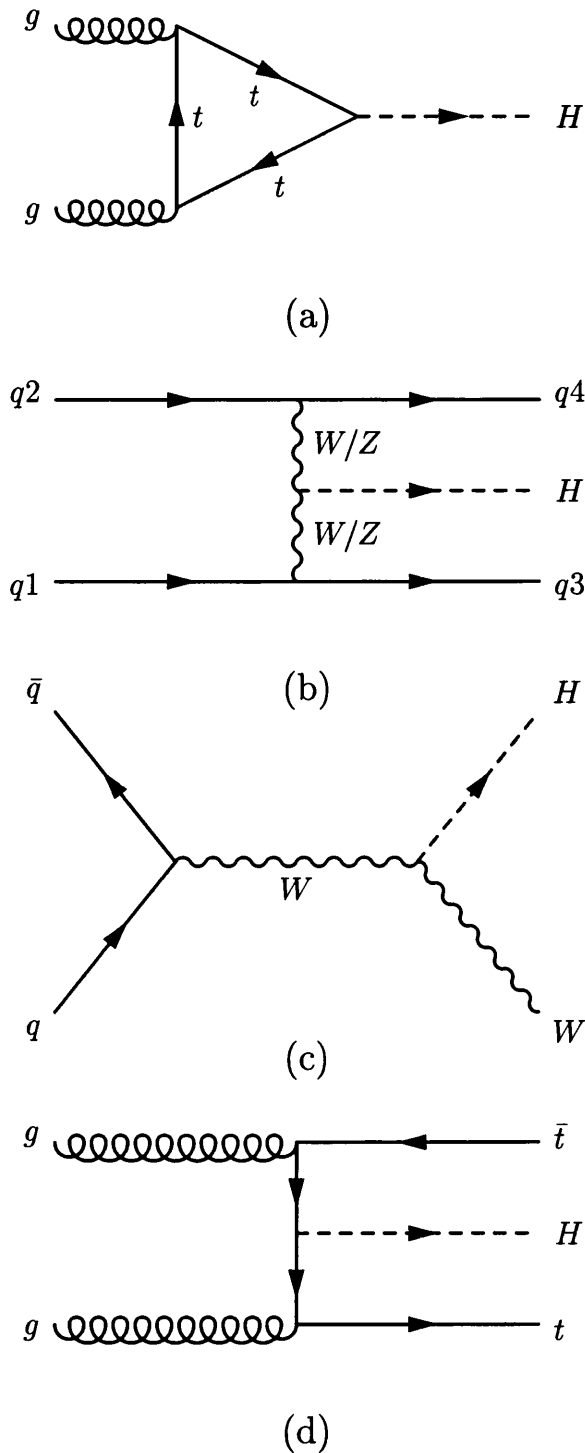


Figure 3.1: Higgs production diagrams for (a) gluon-gluon fusion, (b)  $WW$  or  $ZZ$  fusion, (c) associated production with  $W$  or  $Z$  bosons and (d) associated production with  $t\bar{t}$ .

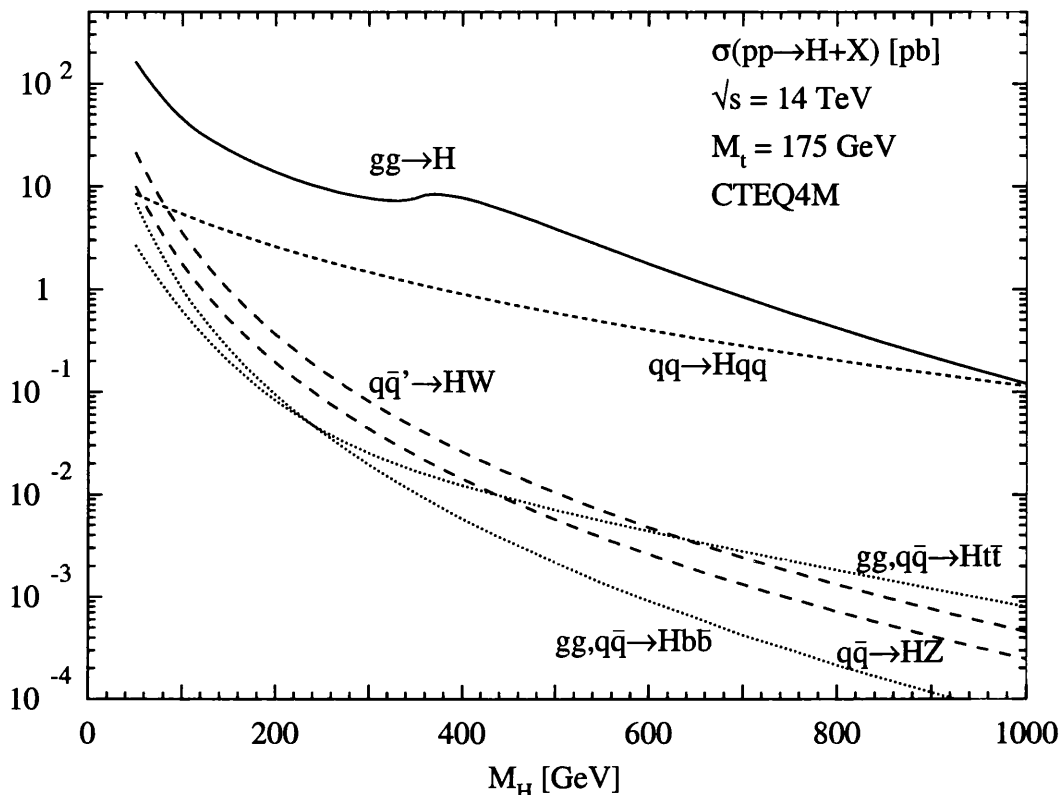


Figure 3.2: Higgs production cross-section as a function of Higgs mass. [32]

Figure 3.3 shows the branching ratio of the Higgs as a function of  $m_H$ . For  $m_H < 130$  GeV the dominant decay is to  $b\bar{b}$ . Beyond this mass range, decays to  $WW$  dominate with decays to  $ZZ$  at about half the rate of decays to  $WW$ . From  $m_H = 350$  GeV the decay mode to  $t\bar{t}$  opens up, however the branching ratio is about 20% of the  $WW$  branching ratio.

The  $H \rightarrow \gamma\gamma$  decay [19] is a rare decay. However it is a promising channel for Higgs searches in the mass window  $100 < m_H < 150$  GeV and requires excellent energy measurement from the ATLAS detector. The important backgrounds are the irreducible prompt  $\gamma\gamma$  continuum, QCD jet-jet,  $\gamma$ -jet and (if  $m_H \approx m_Z$ )  $Z \rightarrow ee$ .

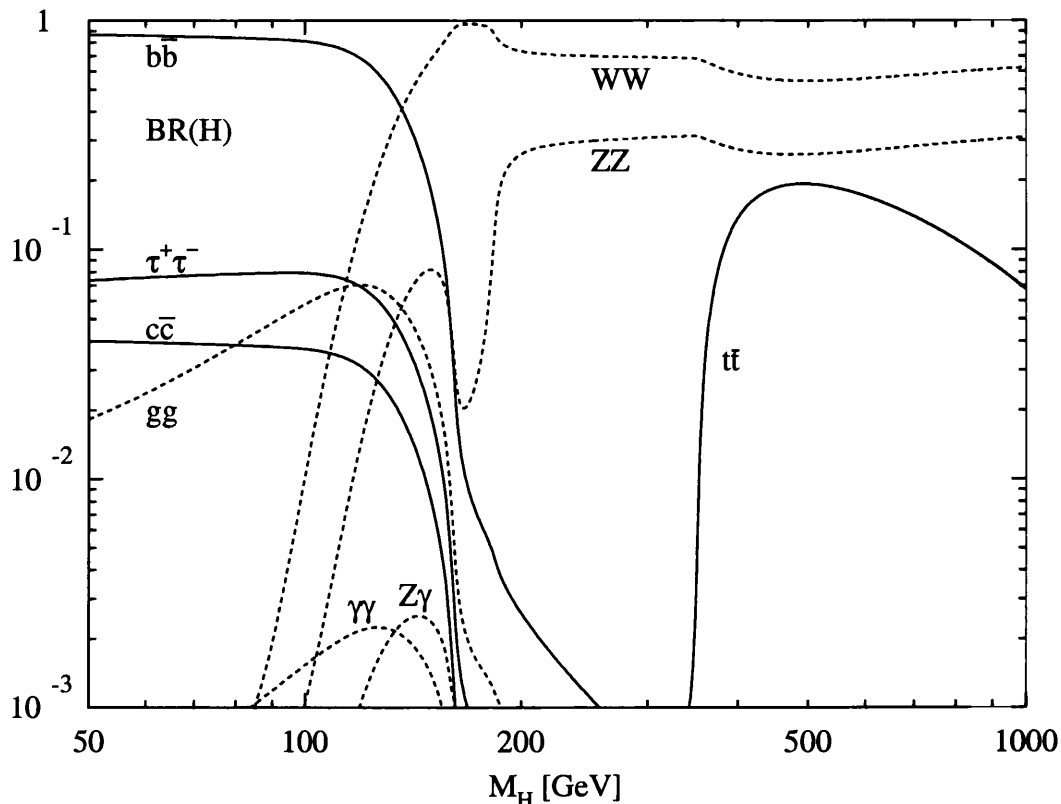


Figure 3.3: Higgs branching ratio as a function of Higgs mass. [32]

The associated production channels  $WH$  and  $t\bar{t}H$  are applicable for  $m_H < 120$  GeV. They both require excellent  $b$ -tagging. Background in both cases are  $t\bar{t} + \text{jets}$  and  $W + \text{jets}$ . The  $t\bar{t}H$  channel is discussed in section 3.6.

The decay channel  $H \rightarrow ZZ^* \rightarrow 4l$  provides a clean channel for  $120 < m_H < 800$  GeV. For  $m_H > 180$  GeV both the  $Z$ 's are real. Backgrounds here are  $ZZ^*$  continuum production and  $Zb\bar{b}$ .

For a Higgs mass close to twice the  $W$  mass the  $H \rightarrow ZZ^* \rightarrow 4l$  branching ratio is reduced as the  $H \rightarrow WW$  decay mode opens up, suppressing the  $ZZ^*$  branching ratio. For a Higgs mass of 170 GeV the  $H \rightarrow WW$  branching ratio is close to 1. The  $H \rightarrow WW$  decay is also useful up to  $m_H = 1$  TeV, however

below  $m_H < 800$  GeV  $H \rightarrow ZZ \rightarrow 4l$  is the simpler discovery channel.

The discovery potential of these channels is determined from the *significance* of the channel which is equal to the expected number of signal events divided by the square root of the expected number of background events, both determined from Monte Carlo simulations. Figure 3.4 shows the overall significance for Higgs discovery from all channels [19]. Clearly the low mass region is the most challenging for ATLAS to discover the Higgs.

### 3.6 $t\bar{t}H$

$H \rightarrow b\bar{b}$  is the dominant decay mode for a Higgs mass less than twice the  $W$  mass. Recent LEP2 results suggest a possible Higgs discovery for  $m_H \simeq 115$  GeV [1] making this channel of particular interest. The direct production from gluon-gluon fusion with decay to  $b\bar{b}$  cannot be efficiently triggered nor extracted from the huge QCD background. The signal can be observed in associated production, if the Higgs is produced with a  $W$  or  $Z$  boson or a  $t\bar{t}$  pair. The leptonic decays of the  $W$  and  $Z$  or the leptonic decay of the  $W$  from the decay of the top quark provide an isolated high- $p_T$  lepton for triggering.

The channel  $t\bar{t}H$  is useful in the mass range  $80 < m_H < 120$  GeV. The cross-section for  $t\bar{t}H$  production is approximately 1 pb for a Higgs mass of 100 GeV [36].

The initial production process is either gluon or quark fusion, with gluon fusion dominating via the diagram shown in Figure 3.1 (d). Each top quark decays to a bottom quark and a  $W$  boson and in this mass range the Higgs decays into a  $b\bar{b}$  pair.

In order to provide a trigger at least one of the  $W$  bosons is required

---

to decay semi-leptonically. The Higgs signal would then appear as a peak in the  $b\bar{b}$  invariant mass distribution. The analysis of this channel therefore depends on excellent  $b$ -tagging performance. The  $b$ -tagging performance of the ATLAS detector is discussed in Chapter 6 and Chapter 7 describes the  $t\bar{t}H$  analysis.

### 3.7 Summary

The operation parameters of the LHC have been described. The expected physics of interest and in particular, a Higgs boson search with the ATLAS detector at the LHC have been introduced. The production and decay modes of the SM Higgs boson have been described and the channels used for search for the Higgs boson with ATLAS have been discussed.

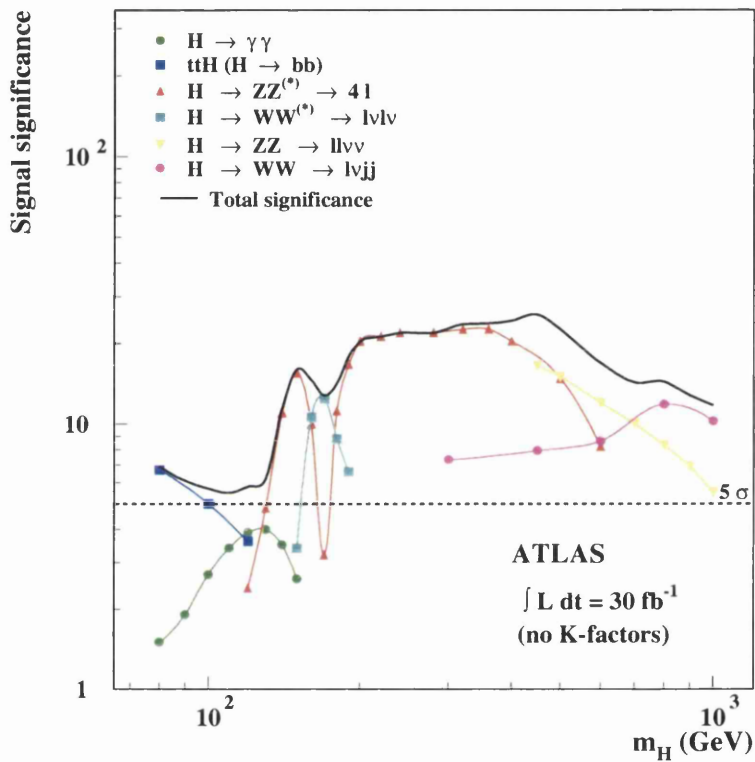


Figure 3.4: The sensitivity of the ATLAS detector for the discovery of the SM Higgs Boson, for 3 year's low luminosity running ( $\mathcal{L} = 3 \cdot 10^4$  pb).

# Chapter 4

## The ATLAS Experiment

### 4.1 Introduction

This chapter describes the ATLAS detector for the LHC accelerator. The overall parameters are first introduced then the separate sub-detector systems are described. Particular attention is paid to the inner detector as this provides the  $b$ -tagging ability, which is required for the Higgs search with  $t\bar{t}H$  discussed in Chapter 7.

### 4.2 Detector Overview

ATLAS [13] is a general purpose detector which will be installed at CERN as a detector for the LHC [14]. Three other detectors will also be built: LHCb [15], ALICE [16] and CMS [17].

The high bunch crossing rate at the LHC causes difficulties for the detector readout electronics. Studies of the readout design show that the small interval between bunch crossings is more challenging in the detector design than the pile-up of minimum bias events. The original bunch crossing sepa-

ration of 15ns was relaxed to 25ns due to these considerations.

The initial design of the ATLAS detector is described in the Letter of Intent [18]. The Technical Proposal [13] gives a more detailed description of the detector. The design of the detector is still evolving somewhat although, with the definitions described in the Technical Design Reports for each detector subcomponent, the design has now largely stabilised.

The design of the detector is based on the requirement to exploit the physics potential of the LHC accelerator to the full. Section 3.3 covers the physics processes. The detector requirements from the potential physics are:

- Good electromagnetic calorimetry for electron and photon identification;
- Good hadron jet energy and spatial resolution;
- Hermetic calorimetry to measure accurately jet and missing transverse energy;
- Efficient tracking at high luminosity for lepton momentum measurements, for  $b$ -quark tagging, and for enhanced electron and photon identification;
- Tau and heavy flavour vertexing and reconstruction capability of some B hadron decay final states, at lower luminosity;
- Standalone, precision muon momentum measurements up to the highest luminosity;
- Large acceptance in tracking coverage out to  $|\eta| < 2.5$ ;
- Triggering and measurements of particles at low  $p_T$  thresholds, e.g.  $p_T > 6$  GeV for muon trigger at low luminosity.

The detector, shown in Figure 4.1, is approximately 42 m long, with a radius of 11 m and an overall weight of approximately 7000 tons. The main components of the detector, in increasing radius are:

- the inner detector (ID);
- the superconducting solenoid;
- the electromagnetic calorimeter (ECAL);
- the hadronic calorimeter (HCAL);
- the air-core toroid magnet and the muon spectrometer.

## 4.3 Detector Subsystems

In this section the detector subsystems are described starting with the magnet system. The sub detectors are then described starting from the outer muon spectrometer inward to the ID. The details of the detector design are still evolving and the design described dates from 1999.

### 4.3.1 Magnet System

The magnet design for ATLAS consists of an inner solenoid and an outer air-core toroid magnet system. The inner 2 Tesla solenoid is positioned between the ID and the ECAL.

The solenoid half length in  $z$  is 2.65 m which is shorter than the 3.35 m half length of the ID. The length of the solenoid is a design compromise. A shorter length reduces the amount of material in front of the calorimeter while a longer length increases the uniformity of the magnetic field inside the

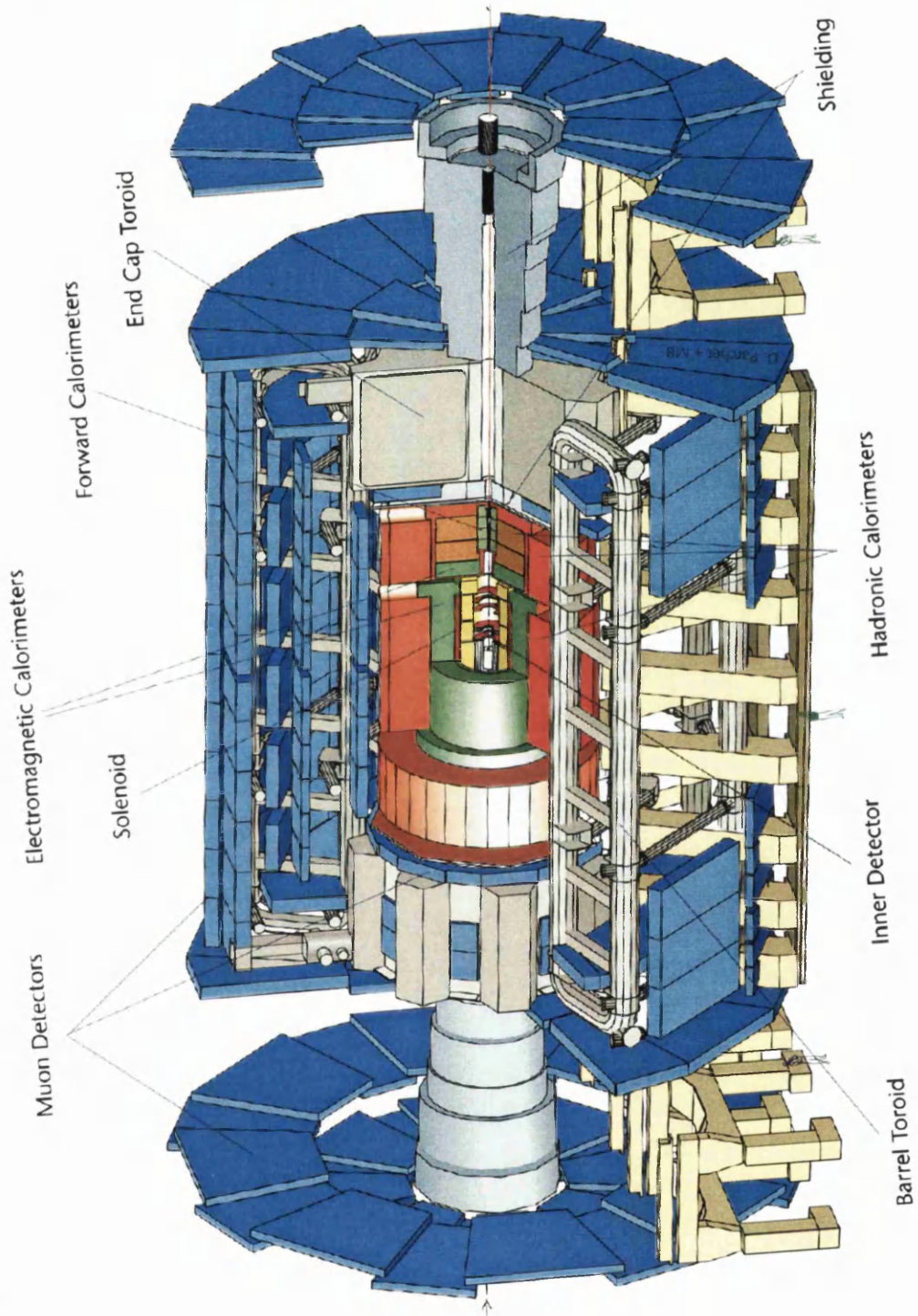


Figure 4.1: Three dimensional cutaway view of the ATLAS Detector.

ID. The solenoid coil which requires cooling is integrated into the vacuum vessel of the ECAL barrel cryostat, eliminating the material and space of independent cooling vessel walls. The superconducting magnet is kept at 4.5 K and gives a 2 T field in the center of the ID falling to 0.5 T at the outer edges of the ID.

The air-core toroid system for the muon spectrometer is made up of a barrel section, and two end-cap toroid sections. The barrel section design is 26 m long with an inner bore of 9.4 m and an outer diameter of 19.5 m. The end-caps are 5.6 m long and have an inner bore of 1.26 m. The individual toroids each consist of eight flat coils symmetrically arranged about the beam axis. The end-cap toroids are rotated with respect to the barrel so that the barrel and end-cap toroids will interleave.

The design gives a (relatively) light and economical structure for the large volume of the magnetic field. Using only eight coils results in the total bending power of the system varying, from 3 Tm at a  $\eta = 0$  to about 8 Tm at a  $\eta = 2.8$ .

### 4.3.2 Muon Spectrometer

The muon detector system in ATLAS serves a dual purpose, both as a trigger to select events with muons and as a precision muon spectrometer. For the trigger system the rapidity coverage extends to  $|\eta| < 2.4$  and down to  $p_T > 6$  GeV. The muon spectrometer as a whole has a rapidity coverage out to  $|\eta| < 2.7$ . For momentum resolution the design performance is to measure  $p_T$  to 2% accuracy at  $p_T = 100$  GeV, degrading to an accuracy in  $p_T$  of 8% at  $p_T = 1000$  GeV.

The muon spectrometer, shown in Figure 4.2, consists of the air-core toroid, a barrel section and two end-cap sections. The barrel section is made

up of three layers of high precision tracking chambers and each end-cap from three vertical discs of tracking chambers. The three layers of the barrel section are positioned at radii of 4.5 m (inner to the toroid), 7 m (inside of the toroid system) and 10 m (outer to the toroid system). The design uses two types of chambers for precision tracking measurements and two types of chambers for triggering. The individual precision chambers have a  $80\ \mu\text{m}$  measurement accuracy and are small enough to have a low occupancy (max 5% per measurement cell) for good pattern recognition and long chamber life.

The air-core toroid provides a magnetic field that is configured such that the muon trajectories are mostly orthogonal to the field. The precision measurement of the muon tracks is either the  $z$  coordinate, for the barrel section or the  $r$  coordinate in the end-caps. The precision chambers are of two types [20] monitored drift tube (MDT) proportional chambers and cathode strip chambers (CSC) which are used in the end-caps due to their higher granularity.

The MDTs are aluminium tubes of 30 mm diameter, with a  $400\ \mu\text{m}$  wall thickness and a  $50\ \mu\text{m}$  diameter central wire. When an ionising particle passes through the tube electrons are ionised from the gas inside the tube. The electrons travel to the anode wire and the radial position of the particle traversing the tube can be determined by measuring the time taken for the ionisation induced charge to move from the particle path to the wire. The MDTs are arranged into multilayers each made up of 3 or 4 MDT layers. The CSC are multiwire proportional chambers with cathode strip readout. The anode wire pitch is 2.54 mm and the anode-cathode spacing is the same as the anode wire pitch. To obtain the precision coordinate the cathode is segmented into strips which are orthogonal to the anode wires and the charge

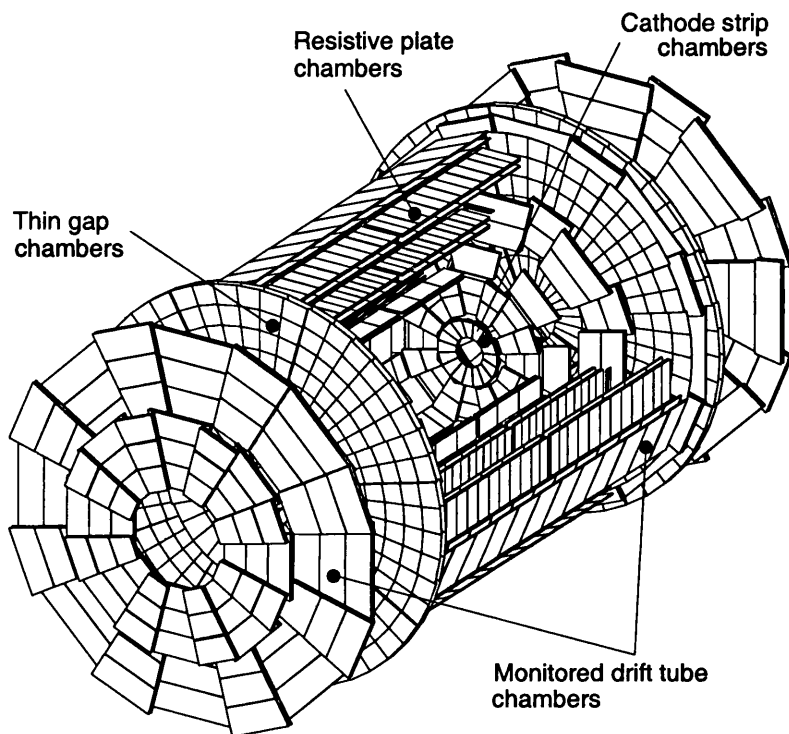


Figure 4.2: A three-dimensional cutaway view of the muon spectrometer, indicating the different chamber technologies used.

induced on the cathode strips by the electron avalanche on the anode wire is measured.

For the trigger muon chambers two types of chamber are used: thin gap chambers (TGC) and resistive plate chambers (RPC). The TGCs are used in the barrel and end-cap regions and the RPCs are used in the barrel. The TGCs are a type of multiwire proportional chamber but with the anode wire pitch larger than the cathode-anode distance. The anode wires provide the trigger signal. The RPCs are gaseous detectors with two parallel bakelite plates, 2 mm thick, separated by 2 mm with a gas mixture between the plates. Primary ionisation electrons are multiplied by an electric field of 4.5 kV/mm across the plates. The signal is read out by capacitive coupling using metal strips on both sides of the detector.

### 4.3.3 Calorimetry

The ATLAS calorimetry is separated into an electromagnetic and a hadronic calorimeter. This is possible due to the different interaction lengths of electromagnetic and hadronic interactions. The ATLAS calorimetry system consists of an inner barrel cylinder and end-caps located inside the muon spectrometer. The conceptual layout of the calorimetry is shown in Figure 4.3. The total thickness of the ECAL is 24 radiation lengths ( $X_0$ ) in the barrel section and 26  $X_0$  in the end-caps. The HCAL has a total thickness of 11 interaction lengths ( $\lambda$ ).

For electromagnetic showers the variations in shape and registered energy are small for showers of equal incident energy, hence energy resolution is limited by the resolution of the calorimeter and by pre-showering. The size of an electromagnetic shower is linearly dependent on the  $X_0$  of the calorimeter material. Material in front of the calorimeter causes pre-showering: electro-

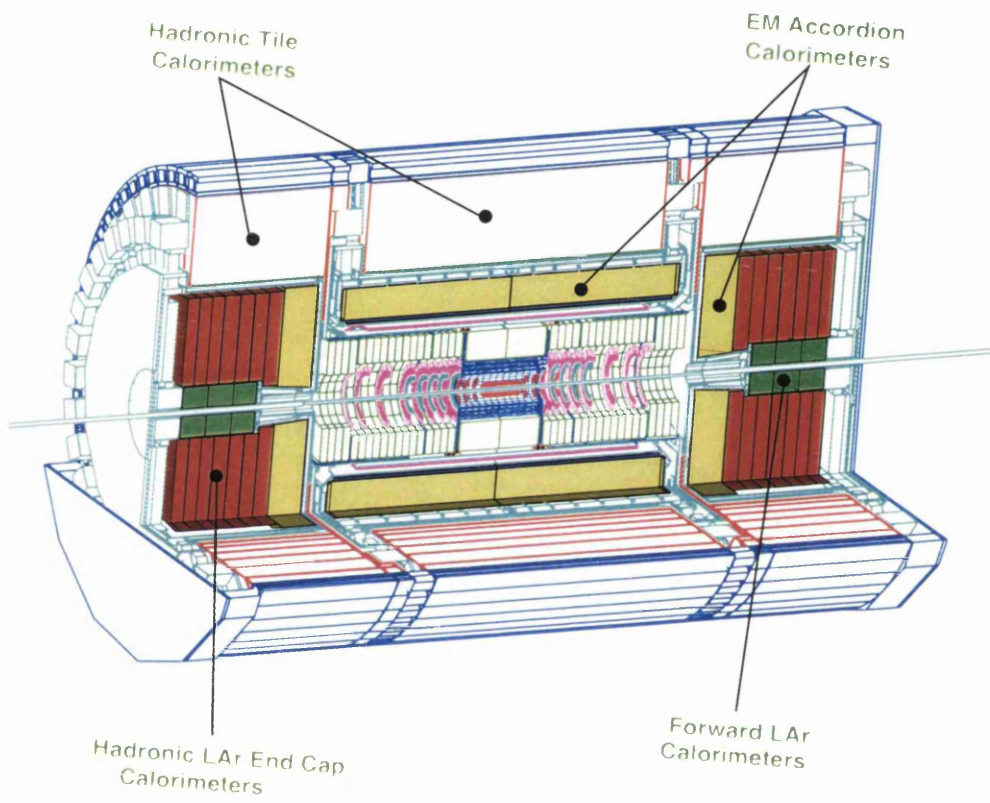


Figure 4.3: A three-dimensional cutaway view of the ATLAS electromagnetic and hadronic calorimetry.

magnetic showers which start in front of the calorimeter and cause the energy of a track deposited in the ECAL to be spread out over a larger area of the calorimeter than would otherwise be the case.

For hadronic showers the nuclear processes producing the secondary pions, neutrons etc., have large variations in the amount of energy transferred to the secondary particles. Hence the resolution on the energy measurement in a hadronic calorimeter is normally limited by the variations intrinsic to the shower. The size of a hadronic shower is linearly dependent on the interaction length  $\lambda$  of the calorimeter material.

The ECAL sections use liquid argon technology, utilising the rapid rise time (approx. 1 ns) of the ionisation current. This, together with suitable electronics, gives a very fast (approx. 40 ns) calorimeter readout. However this readout time is still greater than the bunch crossing interval of 25 ns, resulting in the piling up of tracks from more than one bunch crossing in a single readout cycle.

The ECAL subdetector sections each consist of 1.5 mm or 1.1 mm thick lead absorber plates, arranged in an ‘accordion’ geometry. The absorber plates are clad in 0.2 mm thick stainless steel sheets to give mechanical strength. Between two absorber plates is a liquid argon region in the middle of which is a three layer Kapton-copper readout electrode.

The HCAL uses several different techniques due to varying requirements and radiation environments over the  $\eta$  range of the HCAL. Out to  $|\eta| < 1.7$  an iron scintillating tile [21] system is used. The iron is the absorber for the incoming tracks, the shower then causes scintillation in the tiles which are read out by wave length shifting fibres into photomultipliers. Over the range  $1.5 < |\eta| < 4.9$  liquid argon calorimetry is used. The HCAL liquid argon uses copper as the absorber for  $|\eta| < 3.1$  and in the forward region ( $|\eta| > 3.1$ )

both copper and tungsten are used.

The expected energy resolution of the ECAL is  $\Delta E/E = 10\%/\sqrt{E} \oplus 0.7\% (E \text{ in GeV})^1$ , where the first term arises from variations in the electromagnetic showers and the second term from calibration of the detector. A third term, arising from detector noise, is negligible.

For the HCAL the expected energy resolution is  $\Delta E/E = 52\%/\sqrt{E} \oplus 0.4\% (E \text{ in GeV})$  for pions. Again the first term is due to shower statistics and the second term to detector calibration.

#### 4.3.4 Inner Detector

A cutaway view of the ATLAS ID is shown in Figure 4.4. The ID is located inside the barrel cryostat of the electromagnetic calorimeter, which also houses the superconducting solenoid. This provides the axial 2 Tesla field for tracking. The ID contains three types of precision detectors: three layers of silicon pixel detectors, four layers of silicon strip detectors (SCT) and the transition radiation tracker (TRT). The requirements of the ID are:

- to reconstruct efficiently the tracks and vertices in an event;
- to perform, together with the calorimeter and muon systems, electron, pion and muon identification;
- to find short lived particle decay vertices.

The high precision measurements required of the ID need fine granularity detectors due to the very high track multiplicity expected. The highest precision detectors, located immediately around the vertex region, are silicon

---

<sup>1</sup>the  $\oplus$  indicating combining in quadrature i.e. the square root of the sum of the values squared.

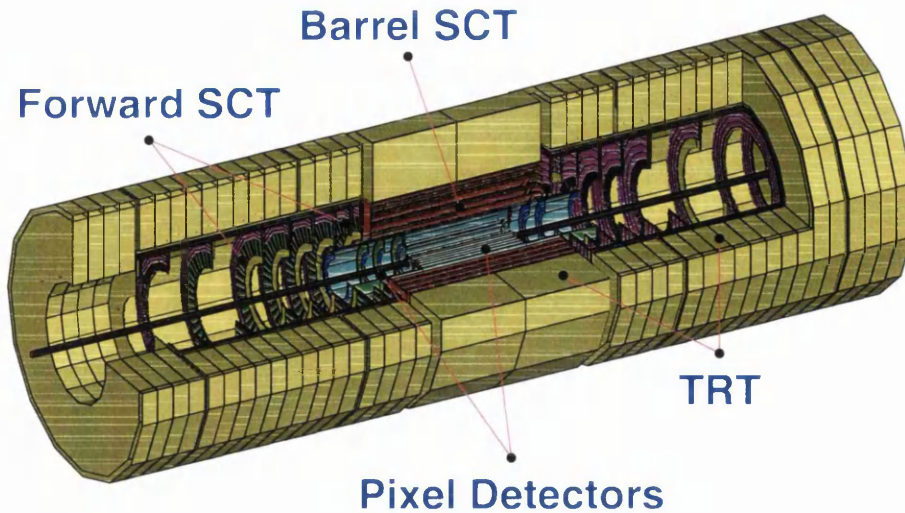


Figure 4.4: Three dimensional cutaway view of the ATLAS ID showing the sub detectors of the ID.

pixel detectors, with a precision of  $12 \mu\text{m}$  in  $r\phi$  and  $66 \mu\text{m}$  in  $z$ . Outside the pixel discs are silicon microstrip detectors ( $\sigma_{r\phi} = 16 \mu\text{m}$ ,  $\sigma_z = 580 \mu\text{m}$ ). The number of these precision layers is limited due to the material introduced and power dissipation of these detectors, as well as the high cost of the detectors. Each track will cross at least four strip layers and 3 pixel layers, for  $|\eta| < 2.5$ . The Transition Radiation Tracker (TRT) or straw tube tracker provides a large number of tracking points, typically 36 points per track. The TRT uses less material per point and at a lower cost per point, although at a lower precision ( $\sigma = 170 \mu\text{m}$ ) than the pixel and strip detectors.

The ID half-length in  $z$  of the ID is 350 cm and the outer radius is 115 cm. The ID is physically divided into three parts: a barrel section with a half length of 80 cm and two identical end-caps which fill the rest of ID cavity. The precision tracking layers are cylinders in the barrel section and discs in the end-cap sections. In both cases the precision detectors are contained within a radius of 56 cm. External to the precision layers is the continuous

TRT tracker out to 105 cm, beyond which are the support and services. The TRT wheels at the outermost  $z$  extend inwards to a lower radius to help give a uniform coverage over the full acceptance.

In the barrel section the pixel layers are segmented in  $r\phi$  and  $z$ . Each layer of silicon strips consists of two silicon strip detectors back to back with a 40 mrad stereo angle between the strip directions. For the barrel layers one set of strips in each layer measures the  $\phi$  coordinate. End-cap strip detectors again have two layers back to back with a 40 mrad angle between the strips but here one of the strips is always in the radial direction. The TRT straws are parallel to the beam axis in the barrel and arranged radially in the end-cap.

The expected  $p_T$  resolution is  $\Delta p_T/p_T < 30\%$  for muons with  $p_T = 500$  GeV and the expected vertex resolution is 25  $\mu\text{m}$  in  $x$  and  $y$  and 40  $\mu\text{m}$  in  $z$ . Figure 4.5 shows a cross sectional engineering layout of the ID. The space point resolutions and basic design parameters of the ID elements are summarised in Table 4.1. The inner-most pixel layer at 4 cm enhances the impact parameter measurements, secondary vertex measurement and the heavy flavour tagging. However the lifetime of the inner pixel layer is expected to be limited due to radiation damage and it will need to be replaced after a few years of operation, the precise time being dependent on the luminosity vs. time profile of the LHC.

### Pixel Detector

Silicon is an excellent material for tracking detectors as the minimum energy required to create an electron/hole pair is 3.6 eV. For a minimally ionising particle approximately 80 electron/hole pairs are produced per  $\mu\text{m}$  thickness of silicon that the particle traverses. If a voltage is applied across the silicon

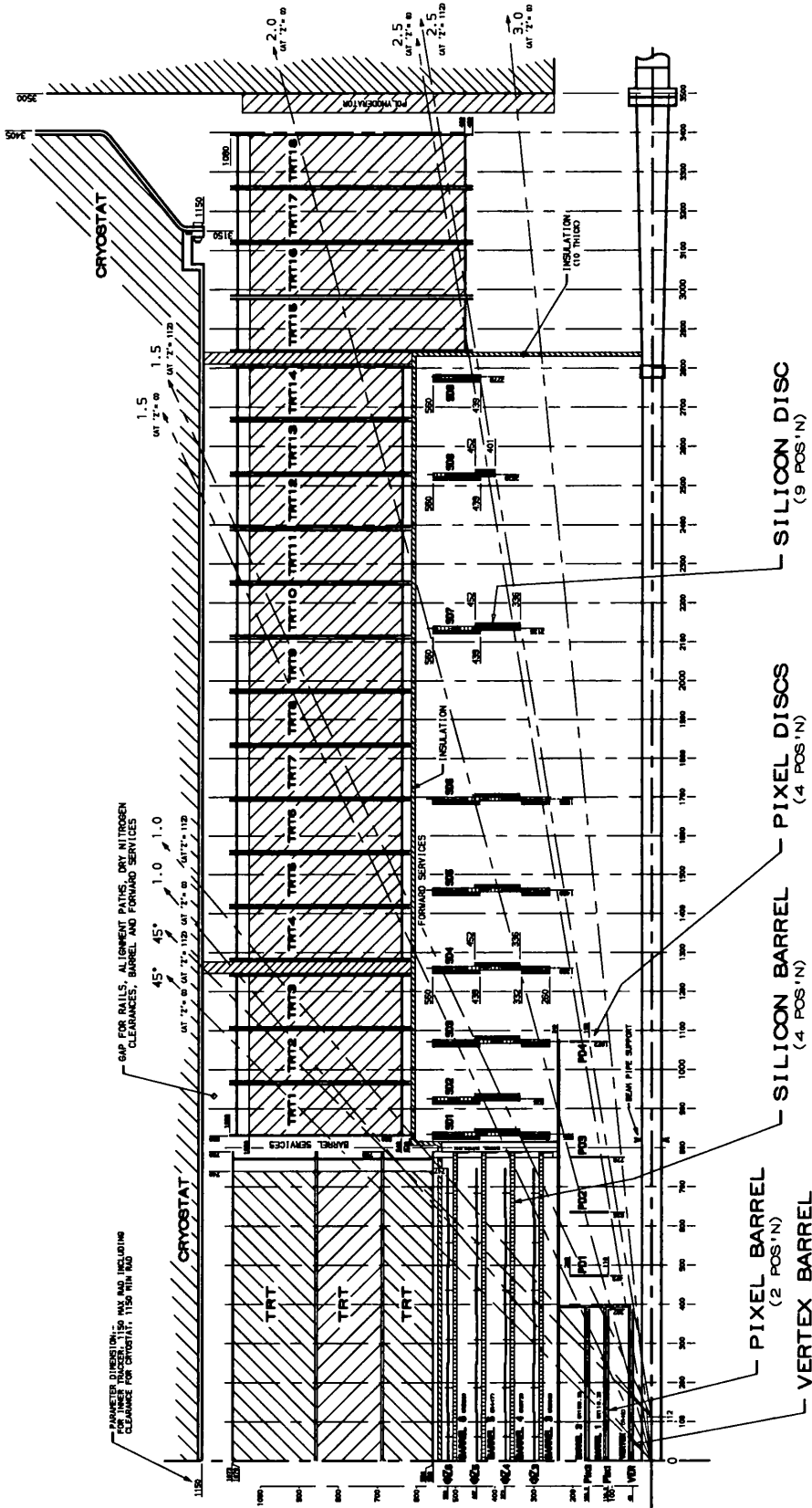


Figure 4.5: Cross section of ID layout through the beam axis.

System	Position	Resolutions			Channels ( $10^6$ )	$ \eta $ coverage
		$r\phi$ ( $\mu m$ )	$r/z$ ( $\mu m$ )	$\phi$ (mrad)		
Pixels	B-layer	12	66 ( $z$ )	0.3	16	2.5
	Barrel	12	66 ( $z$ )	0.08	81	1.7
	End-cap	12	77 ( $r$ )	0.08	43	1.7-2.5
Strips	Barrel	16	580 ( $z$ )	0.035	3.2	1.4
	End-cap	12	580 ( $r$ )	0.029	3.0	1.4-2.5
TRT	Barrel	170 (per straw)		0.17	0.1	0.7
	End-Cap	170 (per straw)			0.32	0.7-2.5

Table 4.1: Parameters and measurement resolutions for individual detector elements of the ID.

then the electrons and holes will move towards the surface electrodes where they can be detected.

Pixel semiconductor detectors are used closest in to the interaction point due to the extremely high charged particle multiplicity in the region. The pixel system resolution determines the impact parameter resolution and hence the  $b$ -tagging ability of the inner tracker. With a two dimensional segmentation the detector gives space points without the ambiguities associated with strip detectors. However this requires advanced electronics so that each pixel can be read out. Each readout chip is bump-bonded to the detector substrate and hardened to withstand over 30 kGy of ionising radiation and over  $5 \cdot 10^{13}$  neutron per  $cm^2$  per year of full luminosity operation[13].

The pixel barrel section of the inner tracker is made up of pixel modules

Layer	Radius (cm)	Active half- length (cm)	Tilt angle (degrees)
B-layer	4.0	38.4	+10.5
Layer 1	11.0	38.4	+9.5
Layer 2	14.2	33.8	+9.5

Table 4.2: ID pixel barrel parameters.

arranged on three cylindrical layers at average radii of 4 cm, 11 cm and 14 cm. The pixel modules have a small tilt from the perpendicular to the radial direction. The tilt angle was chosen to maximise the charge collected by a single pixel and thus keep the single pixel detection efficiency high. Table 4.2 gives the radii, active half lengths and tilt angles for each of the three layers.

The individual pixel modules in the barrel are 62.4 mm long and 22.4 mm wide, with a total of 61440 pixel elements on each module. Each individual pixel is 50  $\mu\text{m}$  in  $r\phi$  and 300  $\mu\text{m}$  in  $z$ . Each module uses 16 readout chips. The modules overlap in order to give hermetic coverage, as shown in Figure 4.6.

The barrel pixel modules are arranged in long ‘ladders’, which are parallel to the  $z$  axis of the detector. The modules overlap in  $z$  with alternate modules shifted  $\pm 0.03$  cm from the nominal radial position. The pixel ladders are tilted in  $\phi$  giving an overlap in the active area of the modules.

The end-cap pixel modules are arranged in rings, modules adjacent in  $\phi$  are mounted on alternate sides of the support and service ring. The modules are arranged so that there is an overlap of 200  $\mu\text{m}$  in  $r\phi$ . There are two types of pixel ring: inner (active radius from 11 to 16 cm) and outer (active radius from 16 to 21 cm). One outer ring and one inner ring are placed together on three discs at  $z = 47, 64$  and  $78$  cm. The fourth disc at  $107$  cm consists of one outer ring alone. The parameters of the pixel discs are summarised in



Ring type	Number of Modules	Active $R_{min}$ (cm)	Active $R_{max}$ (cm)
Inner	108	11.00	15.94
Outer	144	15.90	20.84

Table 4.3: End-Cap pixel ring parameters.

Disc number	$z$ position (cm)	Ring types
1	47.3	inner, outer
2	63.5	inner, outer
3	77.6	inner, outer
4	107.2	outer

Table 4.4: End-Cap pixel disc parameters.

Tables 4.3 and 4.4.

### SCT Detector

The silicon strip detectors used in the ATLAS detector have a single-sided readout of  $n^+$  strips with an n-type bulk, as this is expected to be resistant to radiation. Over time the high radiation environment of ATLAS will cause the bulk material to change into a p-type semiconductor. This will happen after 1-2 years of full luminosity running, however the detectors will still be functional.

As with the pixel detector the SCT consists of a barrel detector unit and two end-cap detectors. The SCT barrel is formed from modules arranged in four cylinders. Each layer has an active half length in  $z$  of 74.5 cm and a tilt

Layer	$r$ (cm)	Number of modules in $\phi$
1	30.0	32
2	37.3	40
3	44.7	48
4	52.0	56

Table 4.5: SCT barrel layer parameters.

angle of  $10^\circ$ . Table 4.5 gives the different parameters of each of the barrel layers. Each SCT barrel module is made up of two silicon strip detectors. Each strip detector is formed from two silicon crystals 6.36 cm square and 300  $\mu\text{m}$  thick to form a 12.72 cm long, 6.36 cm wide silicon surface. This gives 768 strips each of 80  $\mu\text{m}$  width across each detector module. The innermost of the two strip detectors is rotated by 40 mrad relative to the outermost detector, along the long axis of the module parallel to the beam pipe.

The modules which make up the barrel are arranged, end to end, on long ladders parallel to the beam direction. The ladders each hold 12 modules. Modules within a ladder are staggered by  $\pm 1$  mm above and below the layer radius to give an overlap of the active area in the  $z$ -direction. The SCT ladders are tilted in the  $\phi$  direction to maximise the strip efficiency and to give an overlap in the  $r\phi$  direction (typically 1-2 mm active area overlap).

Each end-cap SCT module is formed from two trapezoids of active semiconductor material. The precise size and shape of the trapezoids depends on the radial position occupied in the SCT end-cap. These strips are each keystone-shaped, i.e. their width is uniform in  $\phi$ . As the width of each of the modules is dependent upon which ring they are mounted on, the strip pitch also varies, from about 63  $\mu\text{m}$  for the smallest radii modules to 85  $\mu\text{m}$

Ring type	Number of modules	Active $r_{min}$ (cm)	Active $r_{max}$ (cm)
1	52	43.8	56.0
2	40	33.4	45.1
3	40	39.9	45.1
4	40	26.0	33.1

Table 4.6: End-Cap SCT ring parameters.

for the largest.

The two semiconductor trapezoids are set at an angle to each other of 40 mrad, with the strips of the inner trapezoid running radially. The rotation is in the opposite direction for adjacent wheels.

On each ring adjacent modules are separated by 0.25 cm in  $z$  to allow for an overlap of active area in  $\phi$ . Four types of ring are used to cover different radial ranges. The parameters of the rings are given in Table 4.6.

Each of the rings are arranged on one of nine wheels. Rings which overlap in active radii are placed on opposite sides of a wheel. To avoid lining up all the overlapping material in  $\phi$  the wheels are rotated in  $\phi$  with respect to each other. Table 4.7 gives the parameters for the nine wheels.

## TRT

The TRT is the outer-most subdetector of the ID located between the silicon tracker and the solenoid. The TRT consists of straw detectors, thin proportional chambers which can operate at very high rates due to their small diameter and the isolation of the sense wires within individual gas envelopes. The TRT is radiation hard and each track which traverses the TRT will on average trigger 36 straws. Electron identification is performed using xenon

Wheel number	$z$ position (cm)	Ring types	Active $r_{min}$ (cm)	Active $r_{max}$ (cm)	$\phi$ rotation degrees
1	83.5	1, 2, 4	26.0	56.0	0
2	92.5	1, 2	33.4	56.0	2.3
3	107.2	1, 2, 4	26.0	56.0	-2.3
4	126.0	1, 2, 4	26.0	56.0	0
5	146.0	1, 2, 4	26.0	56.0	2.3
6	169.5	1, 2, 4	26.0	56.0	-2.3
7	213.5	1, 2	33.4	56.0	0
8	252.8	1, 3	39.9	56.0	2.3
9	277.8	1	43.8	56.0	-2.3

Table 4.7: End-cap SCT wheel parameters.

gas to detect transition radiation photons created in a radiator between the straws.

There are 370,00 straws in total. Each straw is 4 mm in diameter. The barrel straws are 150 cm long and the end-cap straws are between 39 cm and 55 cm long. The straw tube wall consists of 85  $\mu\text{m}$  of Kapton and the gas mixture in the straws is 70% Xe, 20%  $\text{CF}_4$ , 10%  $\text{CO}_2$ . The  $\text{CF}_4$  provides a faster drift-time for electrons than pure xenon, which gives a higher spatial resolution and reduces the effect from neighbouring bunch crossings. The  $\text{CO}_2$  is added as a xenon/ $\text{CF}_4$  mixture is not stable under high voltage and prevents sparks and streamers in the straw. Running along the centre of each straw is a gold covered tungsten anode wire, 30  $\mu\text{m}$  in diameter. The total drift time is expected to be 40 ns compared to the 25 ns bunch crossing time.

There are about 50,000 straws in the barrel. Each straw is divided in two at the centre, to reduce the occupancy and to give a read out at each end.

Each end-cap contains 160,000 straws which are read out at one end only. All charged particles with  $|\eta| < 2.5$  and  $p_T > 0.5$  GeV cross approximately 40 straws.

## 4.4 Triggering

The bunch crossing rate at the LHC is 40 MHz. The ATLAS trigger system [24] has three levels of event selection. The final event storage rate after the three triggers is designed to be 100 Hz. This requires a rejection factor of  $10^7$  against minimum bias events, while keeping the acceptance for rare and new physics events as high as possible.

Initial selection of events is performed using information from only a subset of the detector read outs. The muon trigger chambers are used to find high  $p_T$  muons, reduced granularity information from the calorimeters is used to find high  $p_T$  electrons, photons, jets,  $\tau$  leptons decaying to hadrons and to find any large missing transverse energy. The level 1 trigger decision is based on the presence (and/or absence) of these objects in combination.

The level 2 trigger uses ‘regions of interest’ which are marked by the level 1 trigger. These regions of interest come from the position of objects found by the level 1 trigger. The level 2 trigger then selectively accesses data from the readout buffers, using only the data required to reach a level 2 trigger decision. Although the level 2 trigger can access all of the data for an event, usually only a few percent of the data will be required to make a trigger decision. The final trigger level is the event filter system, which will use adapted offline analysis routines. The event filter will perform the final selection of events to be written to permanent storage for later offline analysis.

## 4.5 Summary

The ATLAS detector has been introduced. The layout and basic operation of the sub detectors has been described and the measurement precisions of the sub detectors of the ID have been given.

## Chapter 5

# Single Track Performance

In this chapter the performance of the ATLAS ID in measuring the parameters of single tracks is evaluated. The properties calculated represent an idealisation of what can be expected in normal LHC operation, independent of the pattern recognition problems associated with multi-track events. The resolutions determined depend on the detector material description and the individual subdetector resolutions. In particular the effect of removing the innermost pixel layer, the B-layer, is investigated.

### 5.1 Overview of ATLAS Software

The software simulates physics events in the ATLAS detector in a number of steps. Initially an event generator such as PYTHIA [37], HERWIG [38] or ISAJET [39] is used to generate the hard process and the resultant particles for simulation through the detector. For example in the  $b$ -tagging and  $t\bar{t}H$  analyses in Chapters 6 and 7 PYTHIA was used to generate events.

The next step is the simulation of particles through the detector and the digitisation of the detector response to the passage of these particles. This is

done using the GEANT [40] package, with the ATLAS geometry description and digitisation subroutines in the DICE [41] package.

The final step is the reconstruction of tracks from the simulated response in the ID, summation of energy measured in the calorimetry and reconstruction of tracks in the muon spectrometer. Here only the track reconstruction in the ID was required. Several reconstruction programs are available, they are iPatRec [42], xKalman [44] and PixlRec [45]. The data from all the separate programs in the simulation sequence is stored in a set of ZEBRA [46] banks (allowing each package to run separately or in sequence).

### 5.1.1 Detector Simulation

The GEANT package (version 3.21) is used to extrapolate the particle four vectors through the ATLAS detector. For single particle studies the particle four vectors are generated within GEANT. The GEANT program allows for the magnetic field provided by the solenoid (either as a uniform field or with a more complex field map), ionisation energy loss, multiple scattering, bremsstrahlung, photon conversions, nuclear interactions of hadrons and the decays of long-lived particles. Energy which is deposited in the sensitive volumes of the detector is recorded in the HITS bank. The GEANT simulation requires an accurate geometrical description of the detector. This description is provided by the ATLAS interface to GEANT called DICE (Detector Integration Code). A list of all the stable particles generated by PYTHIA (or single particles generated by GEANT) and those created by interaction in the detector are stored in the KINE bank.

### 5.1.2 Digitisation

The DICE package also simulates the electronic response of the detector to the particles. The response of the active parts of the detector to the energy deposited in an active region is obtained in a form similar to that expected from the readout electronics after formatting by the online computers.

The channel numbers, times, energies etc are stored in the DIGI banks. The requirement at this stage is for an accurate description of the physical processes by which analogue signals are collected and transformed by the readout electronics to digital signals. The HITS banks from several collisions can be combined to reproduce the effect of the superposition of several events at high luminosity on the digitisations.

### 5.1.3 Reconstruction

The digitisations from DICE are used to find tracks in the ID and from these to calculate the momenta and direction of the track. The ID tracking volume extends out to  $|\eta| < \pm 2.5$ . For the ID there are three track reconstruction algorithms, these are iPatRec, xKalman and PixlRec. Any track reconstruction algorithm has two basic requirements: to find the tracks of particles in the detector, introducing the minimum number of fake tracks and to give the best estimation of the tracks' actual momenta and direction. For precision detectors with multiple active layers track finding is done by first combining hits in a limited number of active layers to form track candidates. These track candidates are then extended out to other active layers to try and find hits in these layers which lie along the extended track candidate. Track candidates are then accepted as tracks if they satisfy some minimum criteria such as minimum number of hits on the track, maximum number of

hits shared with other tracks, minimum  $p_T$ , etc.

### iPatRec

The iPatRec pattern recognition algorithm [42] is designed to exploit the greater two-track resolution of the pixel and SCT tracking layers. The program begins track finding from the space-points in the high precision tracking layers. During the initialisation phase a geometry database which describes each module of the precision tracker, the layers of the TRT and the inert support/service material is built up. In each case the details of the geometry, material thickness and detector resolution are generated, as well as keys to the appropriate hit decoding, clustering and space-point building algorithms.

Reconstruction is performed in a conical road which joins the vertex region to a seed region on the outer surface of the Inner Detector. Several types of seed can be used: electron/photon candidates from the EM calorimeter, jets from the hadron calorimeter and muon tracks found in the external muon detectors. In addition, for test purposes the Monte Carlo truth information can also be used as a seed.

The space-points contained in the road are collated into four partitions dependent on their relative distances to the vertex region. By design, each track in the ID is expected to have six or more space-points. The first and last partitions are defined such that, in the absence of detector inefficiency and secondary interactions, a track from the vertex region would have a least two space-points in both partitions. Track candidates are found by taking space point combinatorials from three different partitions. A space point in the first partition is obligatory, which in general requires a hit in the first two pixel layers. Primary tracks which undergo a secondary interaction can be recovered by performing reconstruction only in the first three layers providing

there are sufficient hits.

A local helix interpolation between these space-points is used to associate the remaining hits and to find any holes (an active detector region traversed without a hit) on a track. This gives the precision of interpolation with the ability to follow ‘catastrophic’ processes such as an electron bremsstrahlung close to an intermediate point.

To select hits in the TRT, which are a continuation of the track from the precision layers, a histogramming technique [43] is used, which also resolves left/right drift ambiguities. To limit high luminosity and jet core effects where hit densities can be large in the TRT tight cuts are made on the straw residuals and on the ratio of found to expected hits in the straws.

Additional parameters are included in the track fitting to allow for multiple Coulomb scattering and in the case of an EM calorimeter seed to allow for electron bremsstrahlung. The shape of the clustered hit pattern in each discrete detector layer is examined in a track dependent context to allocate a weight to the cluster. Tracks are then ranked by a quality factor. This factor is defined according to the radial track length, the absence of holes, the track fit  $\chi^2$  and the presence of TRT confirmation. The search strategy then extracts the highest quality track candidates from the remaining unused space-points.

### **PixlRec**

PixlRec [45] exploits the high precision space-points and good two track resolution of the pixel detectors. Track finding is initiated from the inner most pixel layers and goes outwards. A combinatorial search is performed using hits from the pixel layers to find track candidates. The track candidate finding algorithm uses an abstraction of the actual detector which relies on

a hyperplane concept. Here a hyperplane is a set of different parts from various subdetectors, built according to some symmetry and periodicity rules which are defined in the ATLAS reconstruction software. Some allowance for inefficiencies in the precision detectors can be made by introducing some redundancy into each hyperplane.

Once the track candidates have been found, remaining precision hits from the SCT layers within a narrow road around the track candidate are associated using the Kalman [49] filter algorithm. Precision is improved using TRT hits with the conformal mapping method developed for xKalman.

### **xKalman**

Unlike iPatRec and PixlRec, the xKalman [44] algorithm initiates pattern recognition by finding track segments in the TRT. Two techniques are used to perform the reconstruction: a histogramming method and the Kalman filter-smoother formalism. The histogramming technique is used for track finding in the TRT and the Kalman technique for the high granularity precision detectors.

There are three steps in the xKalman track finding process. First a global pattern recognition in the TRT is performed, which generates a set of possible track candidate trajectories. The algorithm is applied in 2D projections of the TRT, in the  $r\phi$  plane for the barrel TRT and in the  $z\phi$  plane for the end-cap. This straight-line track representation allows the same histogramming method to be used in both parts of the TRT. The drift time information from the straws is not used in the first step. Each of the track trajectories found is defined as a helix which is used to define a track road through the precision tracker, along which all the measured hits in each precision layer are collected.

In the second step all possible helix trajectories within the initial road, with a sufficient number of precision hits, are found. The tracking and fitting are performed simultaneously using the Kalman filter-smoother formalism. An essential part of the algorithm is the treatment of multiple scattering noise contributions and bremsstrahlung energy losses during the track search procedure, which can be conveniently implemented using the Kalman filter.

For each of the candidate trajectories a so-called  $\mu$ -fit, which accounts only for multiple scattering and ionisation energy losses, is produced. If the TRT identifies the track candidate as an electron then xKalman also produces an  $e$ -fit, which includes bremsstrahlung energy losses. The result of the  $e$ -fit is used only if the fit increases the number of accepted measurement points from the precision layers. A cut is then applied at this stage based on the total number of hits each track candidate has in the precision layers.

For the final, third, step the accepted track trajectories are then extrapolated back into the TRT. A narrow road around all hits in the TRT are then included for the final track updating and fitting.

## 5.2 Track Parameter Resolutions

For these single track studies muons are used in the simulation, which are typically affected only by multiple scattering and ionisation energy losses. Electrons, being lower in mass than muons, are not used as they emit a significant amount of bremsstrahlung radiation as they move through the ID magnetic field. This reduces the momentum of the electron which can introduce ‘kinks’ on the track. Hadrons are not used as hadronic interactions can lead to the particle track ending, making reconstruction impossible. However, in general, a hadron will not interact in the ID and then the reconstructed

track parameters are similar to those from muons.

The nominal ATLAS vertex spread of  $15\ \mu\text{m}$  in the  $xy$  plane and  $5.6\ \text{cm}$  in  $z$  was used to remove any acceptance effects due to tracks at exactly the same  $\eta$ . The uncertainty on the impact parameter will then be the sum in quadrature of the measurement error on the impact parameter and the beam spot spread. Typically this degrades  $\sigma(d_0)$  from  $16\ \mu\text{m}$  to  $22\ \mu\text{m}$  for high ( $p_T > 20\ \text{GeV}$ ) tracks and from  $24\ \mu\text{m}$  to  $28\ \mu\text{m}$  for lower momentum tracks. However for the impact parameter resolutions given later the degradation due to the beam spot spread is removed by determining the impact parameter with respect to the actual generation point, not the nominal vertex position. This is done so that the given uncertainty on the impact parameter is due only to measurement errors.

### 5.2.1 Track Parameterisation

The trajectory of a particle moving in a uniform magnetic field with no multiple scattering and negligible bremsstrahlung radiation, is described in the bending plane (the  $r\phi$  plane in the ATLAS detector) by a helix

$$r\phi = -d_0 + \phi_0 r + \frac{1}{2\rho} r^2 \quad (5.1)$$

and in the  $rz$  plane by a straight line

$$z = z_0 + \cot(\theta) r \quad (5.2)$$

where  $d_0$  is the impact parameter,  $\phi_0$  is the  $\phi$  coordinate of the track in the  $xy$  plane at the point of closest approach to the coordinate origin,  $\rho$  is the radius of curvature (see Figure 5.1) and  $z_0$  is the  $z$  perigee defined as the  $z$  value of the point on the track where the impact parameter is calculated.

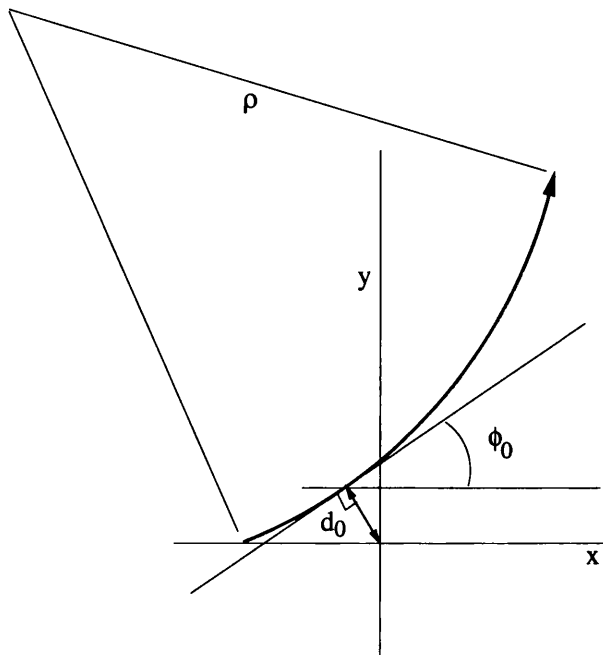


Figure 5.1: The helix parameters of a track moving through the bending plane of a uniform magnetic field.

### 5.2.2 Momentum Resolution

The relevant quantities in the physics of hadron collisions are the transverse momentum  $p_T$  and pseudorapidity  $\eta$  of the tracks. The ATLAS ID has a solenoidal field and measures the curvature ( $1/\rho$ ) of charged tracks. In the absence of multiple scattering the error on the track curvature resulting from  $N$  individual position measurements is constant and equal to [47]

$$\sigma(1/\rho) = \frac{\epsilon}{L^2} \sqrt{A_N} \quad (5.3)$$

where  $\epsilon$  is the error on each position measurement,  $L$  is the distance between the two end point measurements and  $A_N$  is a constant depending on the number and separation of the individual measurement points. With no energy

loss, in a uniform field  $B$  the radius of curvature  $\rho = p_T/eB$ . Therefore

$$\sigma(1/p_T) = e B \sigma(1/\rho) = \frac{e B \epsilon}{L^2} \sqrt{A_N} \quad (5.4)$$

Hence the uncertainty on  $1/p_T$  is constant without multiple scattering. With multiple scattering an additional term is added in quadrature to the measurement error term and the uncertainty on  $1/p_T$  takes the form [48]

$$\sigma(1/p_T) = A_{pt} \oplus \frac{B_{pt}}{p_T \sqrt{\sin \theta}} \quad (5.5)$$

where  $A_{pt}$  and  $B_{pt}$  are constants, with  $A_{pt} = \frac{eB\epsilon}{L^2} \sqrt{A_N}$

Figure 5.2 shows the resolution on  $1/p_T$  for tracks with  $p_T = 200$  and 20 GeV as a function of  $|\eta|$ . At  $p_T = 200$  GeV the detector resolution is dominated by the constant term and is hence quite uniform in  $|\eta|$ . At the lower  $p_T = 20$  GeV the effect of the material in the services ‘dogleg’ can be seen as a bump on the resolution curve around  $|\eta| = 1.5$ . This is seen for 20 GeV and not 200 GeV tracks since tracks at the lower momentum are affected more by the multiple scattering.

Reducing the  $p_T$  further (see Figure 5.3) to 5 and 1 GeV, clearly shows the effect of multiple scattering at all  $|\eta|$  with a marked degradation in resolution and with degrading resolution with increasing  $|\eta|$ .

### 5.2.3 Angular Resolution

Figure 5.4 shows the  $\phi$  resolution for  $p_T = 200, 20, 5$  and 1 GeV as a function of  $|\eta|$ . At high  $p_T$  the  $\phi$  resolution is fairly constant with  $|\eta|$  as there are sets of  $r\phi$  measurements at approximately the same radii for  $|\eta| \leq 2.5$ .

Figure 5.5 shows the resolution on  $\cot(\theta)$  for the same transverse momentum values. Over the precision barrel region ( $|\eta| \leq 1.0$ ) the resolution for  $\cot(\theta)$  is approximately constant. Further out in  $\eta$  in the end-cap region, the precision measurements are in  $r$ . Hence the resolution rises like  $\cot(\theta)$ .

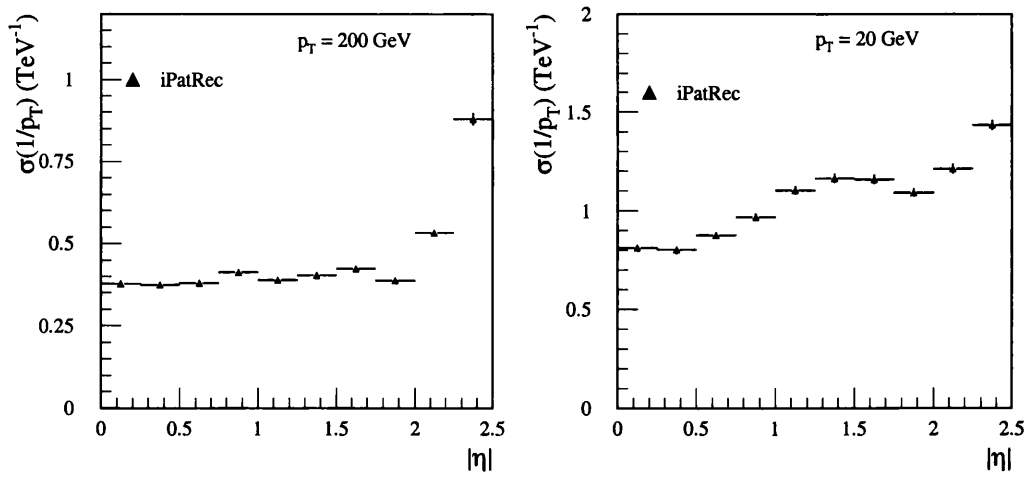


Figure 5.2:  $p_T$  resolution for  $p_T = 200$  GeV (left) and 20 GeV (right), without beam constraint.

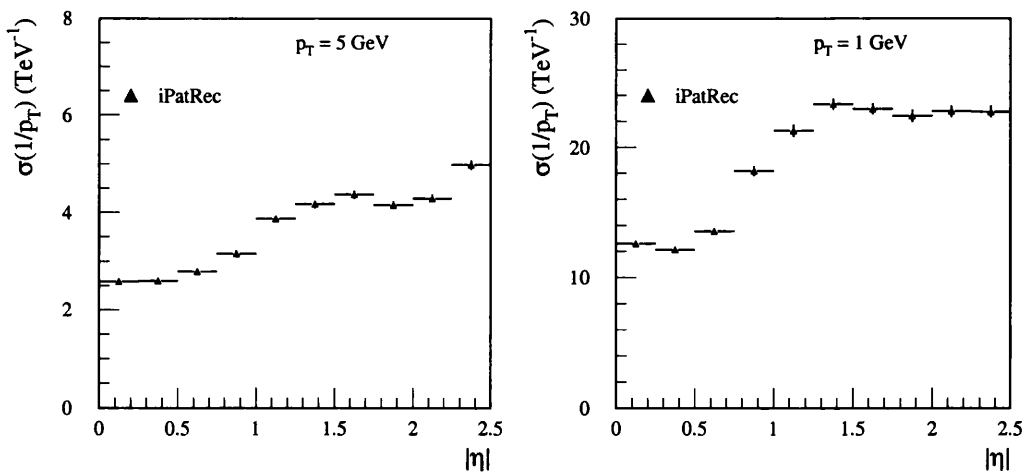


Figure 5.3:  $p_T$  resolution for  $p_T = 5$  GeV (left) and 1 GeV (right), without beam constraint

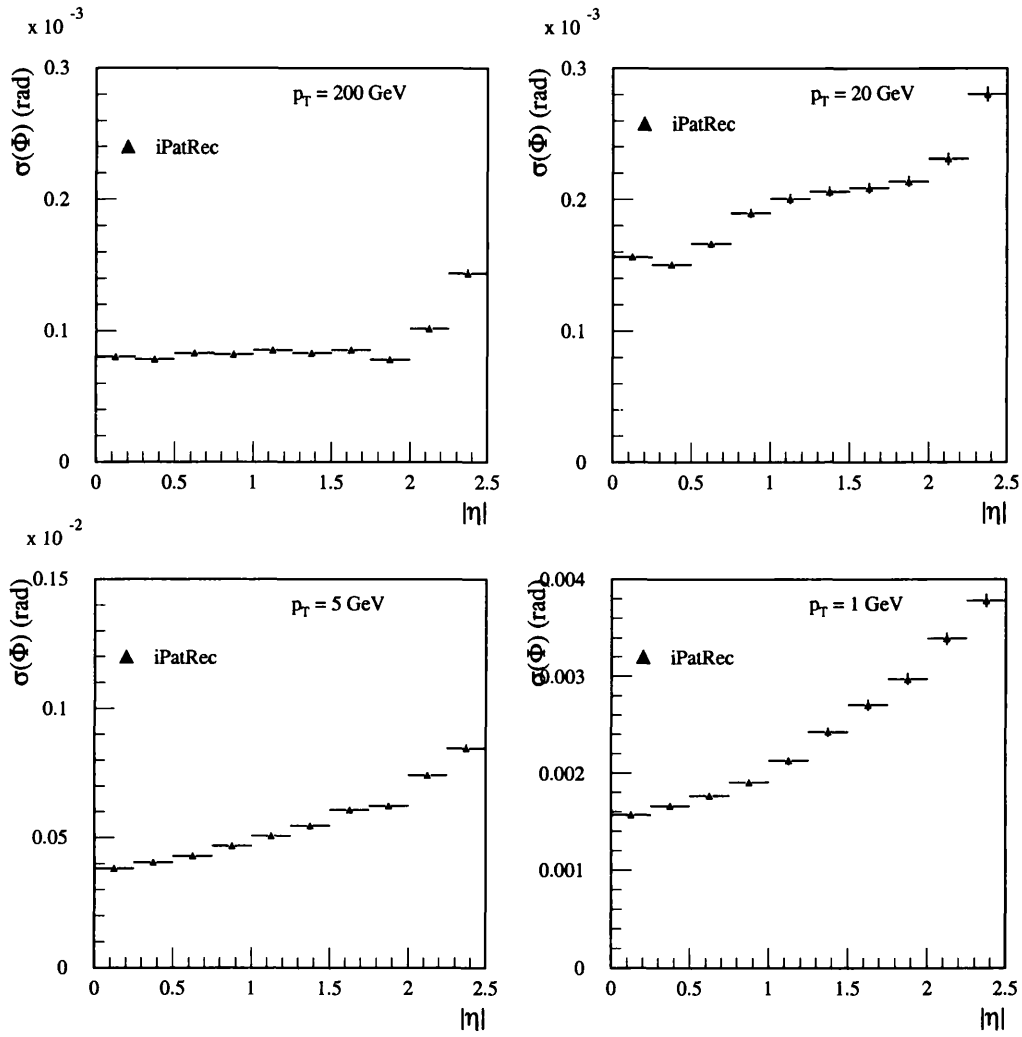


Figure 5.4:  $\phi$  resolution for  $p_T$  of 200, 20, 5 and 1 GeV.

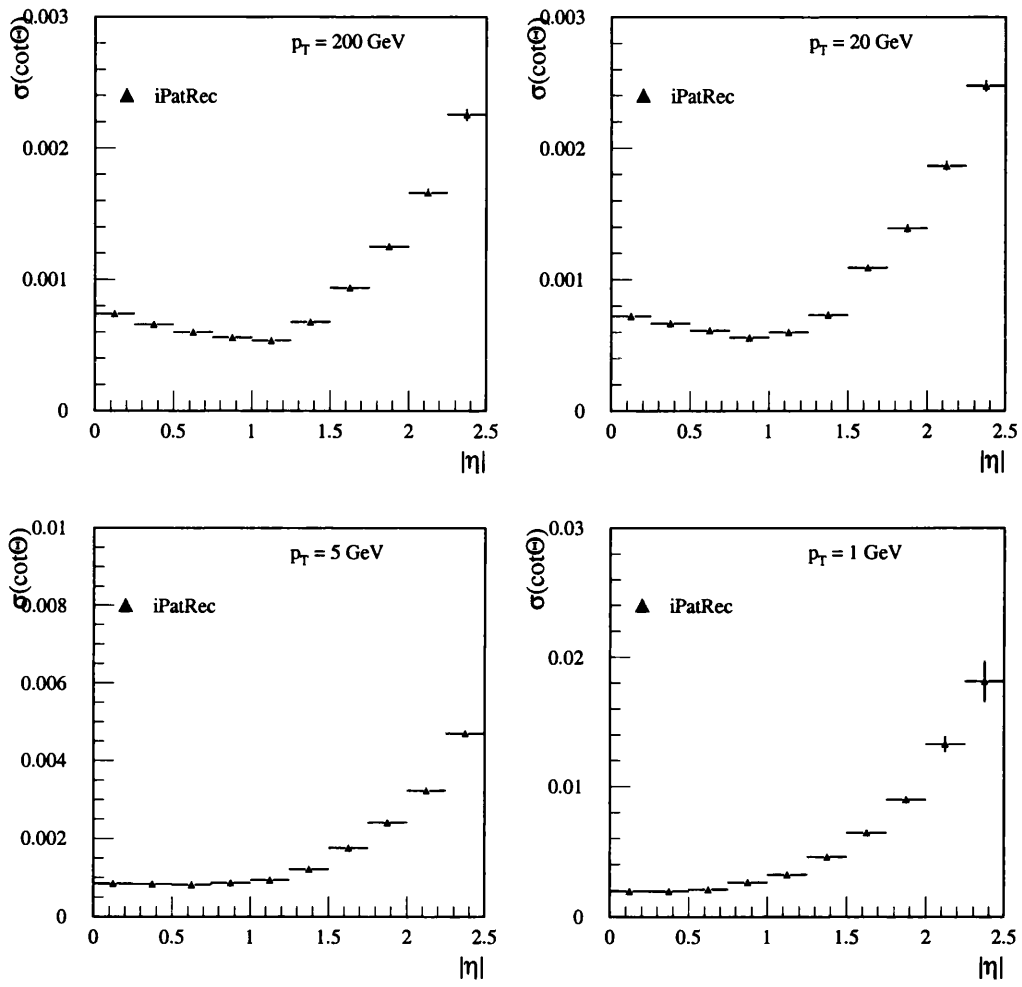


Figure 5.5:  $\cot(\theta)$  resolution for  $p_T$  of 200, 20, 5 and 1 GeV.

## 5.3 Impact Parameter

The measurement of the transverse impact parameter,  $d_0$ , of a track is essential for the reconstruction of secondary vertices, e.g. from B decays; heavy flavour tagging; lifetime measurements and associating tracks to the correct primary vertex. As will be shown, at high momenta the resolution is determined by individual measurement resolutions and is dominated by the precision of the first detector layer, the B-layer at  $r = 4$  cm.

### 5.3.1 Parameterisation

The calculation of the impact parameter resolution is, in general, a non trivial calculation <sup>1</sup>. For two measuring planes the impact parameter resolution can be parameterised as  $A \oplus B/p_T$ . The plausibility of this parameterisation can be seen for the  $z_0$  resolution for a particle traversing two detector planes, as shown in Figure 5.6.

By geometry  $z_0$  is given by

$$z_0 = \frac{r_1 z_2 - r_2 z_1}{r_1 - r_2} \quad (5.6)$$

When multiple scattering occurs only at the measuring planes, then  $z_1$  and  $z_2$  are uncorrelated and only the multiple scattering which occurs at the first plane contributes to the measurement error.

The shift in position of measurement  $z_2$  caused by multiple scattering is  $(r_2 - r_1)\delta_1$  and the RMS value of  $\delta_1$  is  $C/p_T$ , where  $C$  contains the dependence on detector width and material and is equal to [52]

$$C = \frac{13.6 \text{ MeV}}{\beta c} q_n \sqrt{x/X_0} [1 + 0.038 \ln(x/X_0)]. \quad (5.7)$$

---

<sup>1</sup>for a detailed description of the general calculation method see Haywood [50].

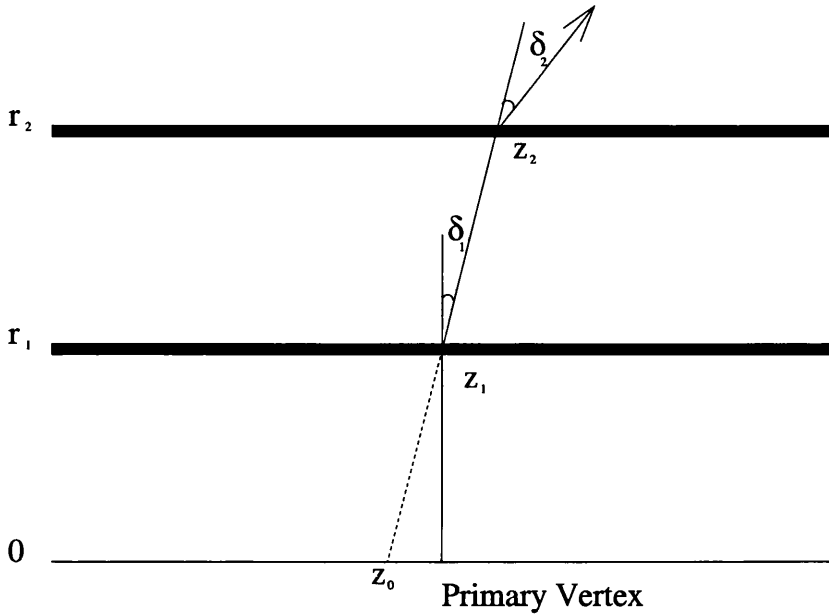


Figure 5.6: Multiple scattering in measuring the  $z$  perigee resolution with two detection planes.

where  $\beta c$  is the velocity,  $q_n$  the charge number of the incident particle and  $x/X_0$  the thickness of the scattering medium in radiation lengths.

For intrinsic measurement errors,  $\sigma_{1,2}$ , the resolution on  $z_0$  becomes

$$\sigma(z_0)^2 = \frac{r_1^2 \sigma_2^2 + r_2^2 \sigma_1^2}{(r_1 - r_2)^2} + \left(\frac{r_1 C}{p}\right)^2 \quad (5.8)$$

Rewritten explicitly in the  $A \oplus B$  form and including a  $\sqrt{(\sin \theta)^3}$  [51] to allow for the increased material thickness travelled through by particles at an angle to the measurement plane this becomes

$$\sigma(z_0) = A \oplus \frac{B}{p_T \sqrt{(\sin \theta)^3}} \quad (5.9)$$

with

$$A = \frac{r_2}{r_2 - r_1} \sigma_1 \oplus \frac{r_1}{r_2 - r_1} \sigma_2 \quad (5.10)$$

and

$$B = 13.6 \sqrt{\frac{x}{X_0}} \left( 1 + 0.038 \ln\left(\frac{x}{X_0}\right) \right) \cdot r_1 \quad (5.11)$$

The expression for  $\sigma(d_0)$  cannot be reduced to a simple formula similar to (5.8), even for the case of only two measuring planes. The  $A \oplus B$  parameterisation is still valid [50] and for two measurement planes is

$$A = \frac{r_2}{r_2 - r_1} \sigma_1 \oplus \frac{r_1}{r_2 - r_1} \sigma_2 \oplus 0.3 r_1 \cdot r_2 \sigma(1/p_T) \quad (5.12)$$

$$B = 13.6 \sqrt{\frac{x}{X_0}} \left( 1 + 0.038 \ln\left(\frac{x}{X_0}\right) \right) \cdot r_1 \oplus 0.3 r_1 r_2 \cdot \sigma(1/p_T) \quad (5.13)$$

where  $r_1$  is the radius of the first layer,  $r_2$  is the radius of the second layer,  $\sigma_1$  and  $\sigma_2$  are the point resolutions of the respective layers,  $x$  is the vertex layer thickness and  $X_0$  is the vertex layer radiation length.

For the ATLAS experiment the  $A \oplus B$  parameterisation is still a good approximation to the actual resolution, the values of  $A$  and  $B$  depend on the geometry of the detector layers used in the simulation.<sup>2</sup> Although the parameterisation is only approximate for the ATLAS detector it is nevertheless useful and explicit fits to the parameterisation will be shown. Figure 5.7 shows the essential parts of the barrel region of the ATLAS inner detector. There are seven silicon layers in the barrel, three layers of pixel detectors and four layers of strip detectors.

### 5.3.2 Simulation Results

Figures 5.8 and 5.9 show the transverse and longitudinal impact parameter resolutions as a function of  $|\eta|$ . The figures show the results obtained from

<sup>2</sup> $A$  depends on the layer resolutions while  $B$  depends on the amount of material in the layers.

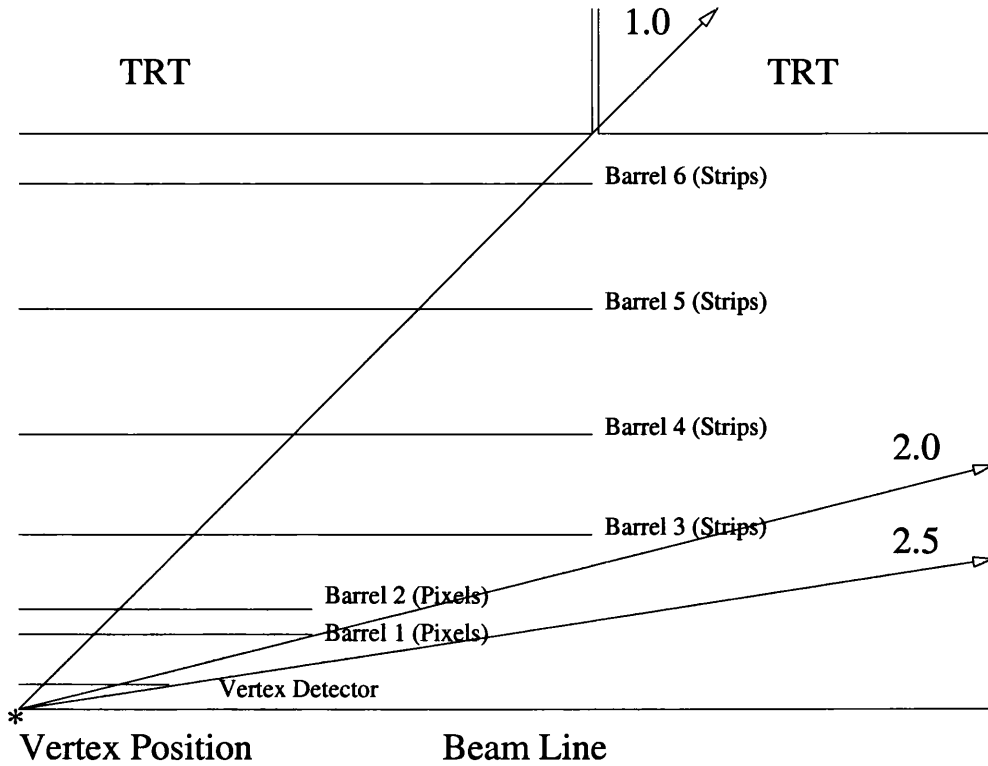


Figure 5.7: Essentials of the barrel region of the ATLAS ID.

each of the three reconstruction algorithms at  $p_T = 200$  GeV.

The small differences between the algorithms can be understood in the way hit clusters are treated. The impact parameter is very sensitive to the resolution of the innermost pixel layer, or B-layer. In any detector layer, including the B-layer the charge induced by a track can be spread out over several pixels. This can result in several pixels giving a signal for a single track. These pixels are termed a cluster and how the cluster pattern is turned into a position coordinate and error varies between the reconstruction algorithms, which leads to the observed small differences in  $d_0$  resolution. This clustering leads to improvements in the effective resolution of the pixels in certain circumstances.

For example for a row of pixels (see Figure 5.10), with particles travelling

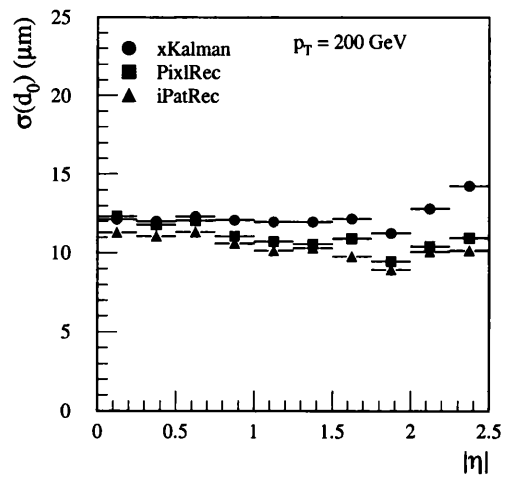


Figure 5.8: Transverse impact parameter resolution for each reconstruction program as a function of  $|\eta|$  for a  $p_T$  of 200 GeV.

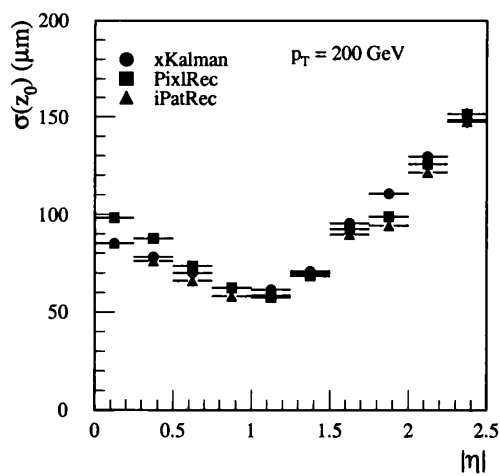


Figure 5.9: Longitudinal impact parameter resolution for all three reconstruction programs as a function of  $|\eta|$  for a  $p_T$  of 200 GeV.

into the page then in case (a) for a single pixel hit the position of the hit is the middle of the pixel with an error of the pixel width divided by  $\sqrt{12}$ . In case (b) when two pixels are hit then the two pixels are treated as a single pixel of width  $2w$  so that position of the hit is the point midway between the pixels with an error of twice the pixel width divided by  $\sqrt{12}$ . However if for 50% of tracks one pixel fires and for the remaining tracks two pixels fire then the resolution can be improved. Assuming that a single pixel fires when the particle passes through the middle half of the pixel and for two pixels firing the particle passes between the two pixels then if one pixel fires (case (c) Figure 5.10) the hit position is the middle of the pixel, the same as (a) but the error is now half the pixel width divided by  $\sqrt{12}$ . Since if the particle had passed through the end quarter of a pixel both it and the neighbouring pixel would have fired. When two pixels fire the position is the same as (b), the point midway between the pixels but the error is again reduced to half the pixel width divided by  $\sqrt{12}$ .

At low  $p_T$  when the resolution is dominated by multiple scattering in the B-layer, there are no significant differences between the reconstruction algorithms. For the following figures the resolutions shown are from the iPatRec algorithm as the iPatRec algorithm gives the (marginally) better resolutions due to optimised use of the cluster patterns.

The critical effect on the measurement of the impact parameter by the B-layer is shown in Figures 5.11 to 5.14. For this study the effect of a dead B-layer was obtained by ignoring the measurements from the B-layer, but the material of the B-layer was still in the simulation. Compared to removing the B-layer from the detector completely this results in a slightly pessimistic effect on the resolution at low  $p_T$  but there is no difference at high  $p_T$ . Also plotted in the figures is a fit to analytical calculation of the impact parameter

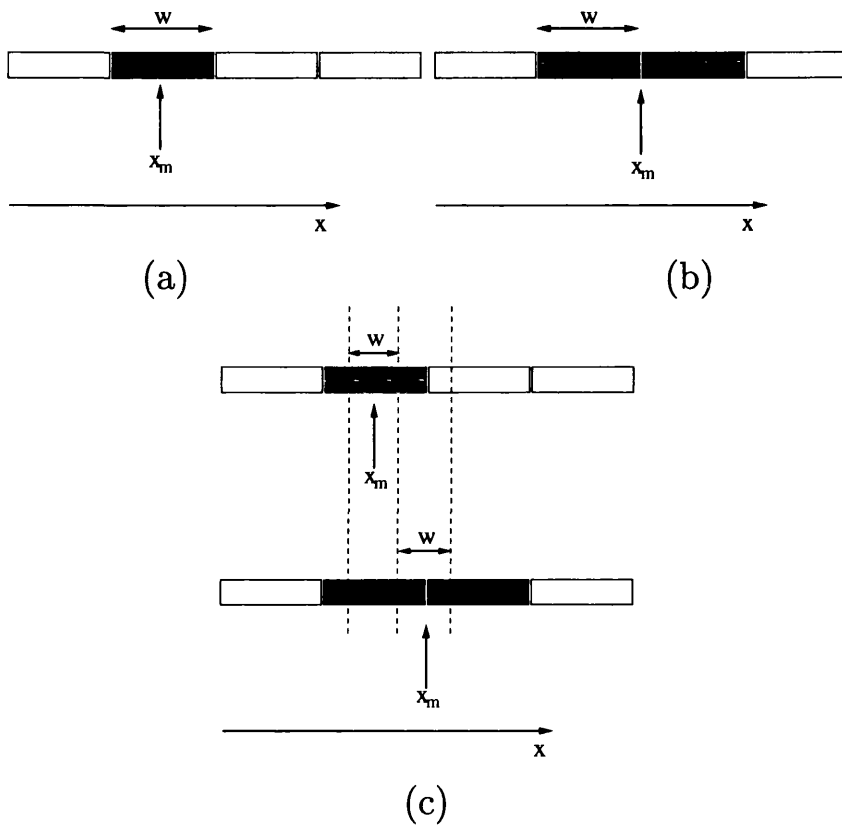


Figure 5.10: The change in effective resolution when 50% of tracks cause one pixel to fire and 50% of tracks cause two pixels to fire, see main text.

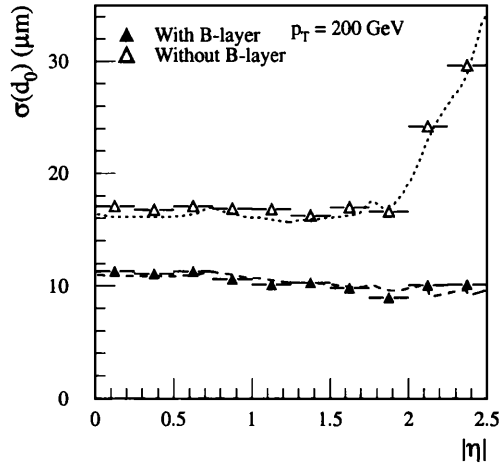


Figure 5.11: Transverse impact parameter resolution as a function of  $|\eta|$  with and without B-layer for  $p_T = 200$  GeV. The function plotted is a fit to an analytical calculation of the resolution (see main text).

resolution. This calculation uses a simplified description of the detector where the material present in the ID is represented as homogeneous cylinders and wheels. Covariance matrices for track fits are analytically calculated for different values of  $|\eta|$  and include multiple scattering. At  $p_T = 200$  GeV, as shown in Figure 5.11, the effect of the B-layer can be seen as an improvement of about 50% in resolution up to  $|\eta| \leq 2.0$ .

The first pixel layer in the barrel (at 11 cm in radius) extends out to  $|\eta| = 2$ . Hence without the B-layer for  $2.0 < |\eta| < 2.5$  the impact parameter resolution would quickly degrade as the radius of the first measurement (now one of the end cap wheels) would be larger than 11 cm. The slight improvement of the resolution with  $|\eta|$  from 0 to 2.5 in the curve with the B-layer is due to the increased cluster size with increasing  $|\eta|$ .

Figure 5.12 shows the transverse impact parameter resolution for  $p_T = 1$

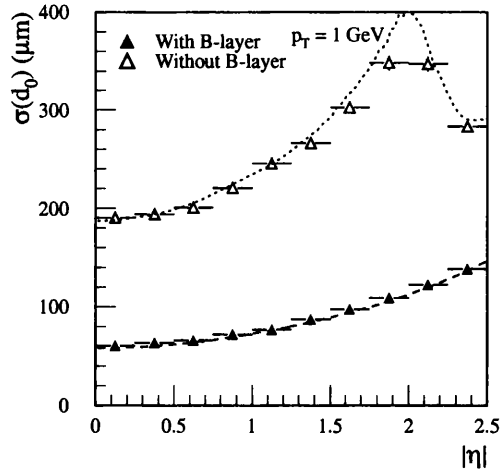


Figure 5.12: Transverse impact parameter resolution as a function of  $|\eta|$  with and without B-layer for  $p_T = 1$  GeV.

GeV. The presence of the B-layer improves the resolution by a factor of 3. The bump in the curve without the B-layer at around  $|\eta| = 2$  is due to the track missing the end of the first pixel layer. However, as the resolution is affected much more strongly by multiple scattering the effect of missing the pixel layer is less pronounced than at low  $p_T$ . The analytical calculation does not agree with the simulation in this region, over estimating the error on  $d_0$ . Slightly further out in  $|\eta|$  there is a small improvement in resolution due to the track passing through the end-cap wheels more optimally, giving pixel clusters with smaller position resolutions.

Figures 5.13 and 5.14 show the longitudinal impact parameter resolution for  $p_T = 200$  GeV and  $p_T = 1$  GeV. The resolution is worse than that of the transverse impact parameter since the B-layer and the other pixel layers have a poorer  $z$  resolution than  $r\phi$  resolution. The resolution has a minimum at  $|\eta| = 1.0$  when a track has a probability of approximately 50% of generating

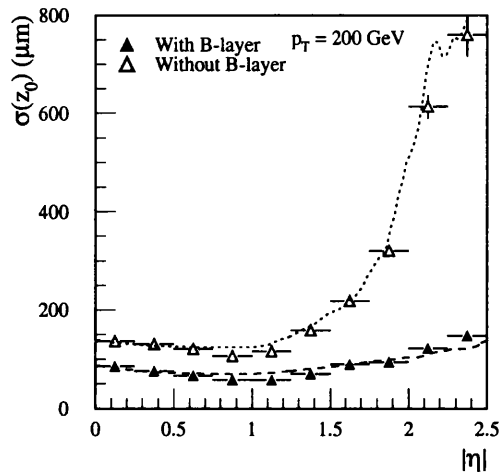


Figure 5.13: Longitudinal impact parameter resolution as a function of  $|\eta|$  with and without B-layer for  $p_T = 200$  GeV.

a two pixel cluster (see Figure 5.10). The shape of the pixel clusters enables the reconstruction algorithm to obtain the best effective resolution from the pixel layers. Again the resolution without the B-layer is degraded and for  $|\eta| > 2.0$  the resolution becomes poor. With increasing  $|\eta|$  the track passes through more material, increasing the multiple scattering and degrading the resolution.

Figures 5.15 and 5.16 show the resolution of the longitudinal impact parameter multiplied by  $\sin \theta$ . For lifetime-related measurements the interesting quantity is the projection of the impact parameters onto a plane transverse to the track direction, i.e.  $z_0 \sin \theta$ . When multiple scattering completely dominates the resolution then the resolution of  $d_0$  and  $z_0 \sin \theta$  should be the same. This is not seen even for  $p_T = 1$  GeV, as the required  $p_T$  for equality is lower than can be measured by the ID. The analytical function does not fit the measured  $z_0 \sin \theta$  points well in either plot, over estimating the error on

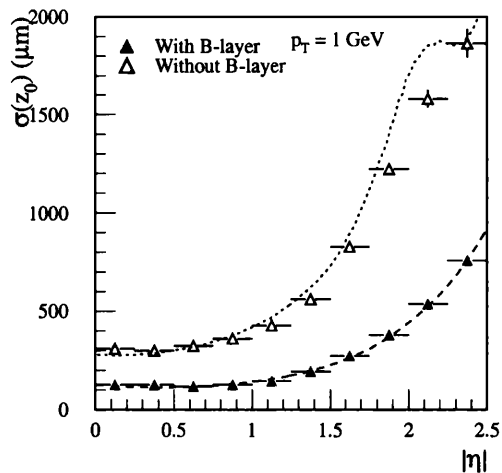


Figure 5.14: Longitudinal impact parameter resolution as a function of  $|\eta|$  with and without B-layer for  $p_T = 1$  GeV.

$z_0 \sin \theta$  between  $1.5 < |\eta| < 2.0$  for  $p_T = 1$  GeV.

Figures 5.17 and 5.18 show the impact parameter resolutions as a function of  $p_T$  for central tracks with  $|\eta| < 0.5$ , with and without the B layer. Also shown on the plots are curves which correspond to the  $A \oplus B/p_T$  parameterisation, where  $A$  has been determined from the asymptotic high  $p_T$  value and  $B$  adjusted such that the curve passes through the  $p_T = 1$  GeV data. For  $d_0$   $A_{d_0} = 11$  and  $B_{d_0} = 59$  and for  $z_0$   $A_{z_0} = 85$  and  $B_{z_0} = 94$ .

As can be seen from the figures the  $A \oplus B/p_T$  curve fits the points with B-layer slightly better, and is also a slightly better fit to the  $z_0$  resolution than the  $d_0$  resolution.

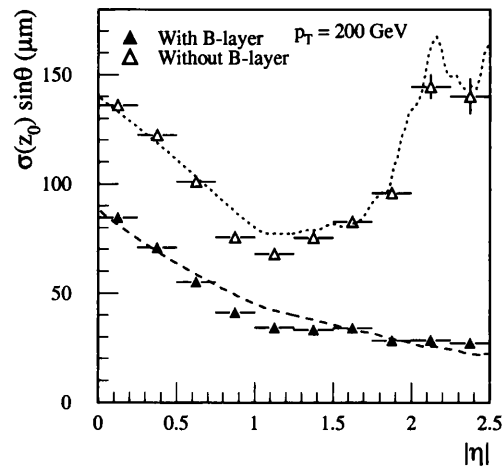


Figure 5.15:  $\sigma(z_0) \sin \theta$  resolution as a function of  $|\eta|$  with and without B-layer for  $p_T = 200$  GeV.

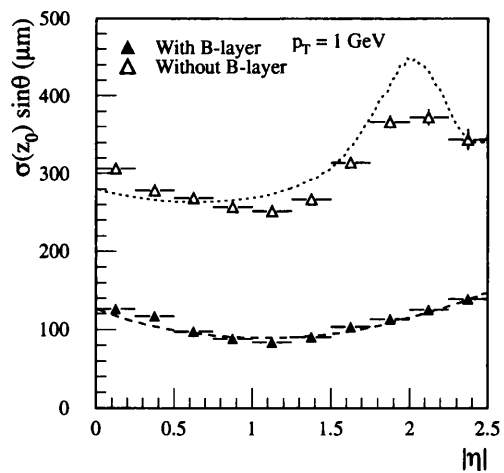


Figure 5.16:  $\sigma(z_0) \sin \theta$  resolution as a function of  $|\eta|$  with and without B-layer for  $p_T = 1$  GeV.

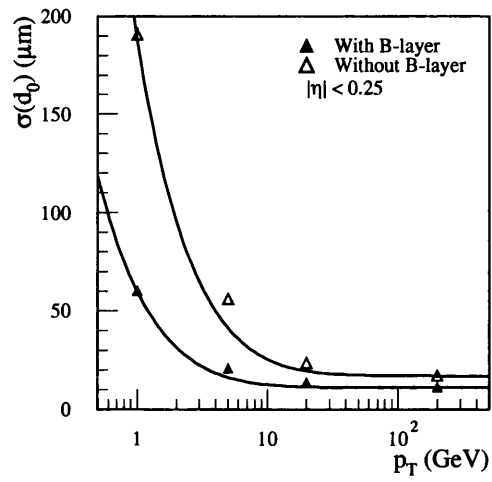


Figure 5.17: Transverse impact parameter resolution for  $|\eta| \leq 0.5$  as a function of  $p_T$ . The function plotted is a fit to the  $A \oplus B$  parameterisation.

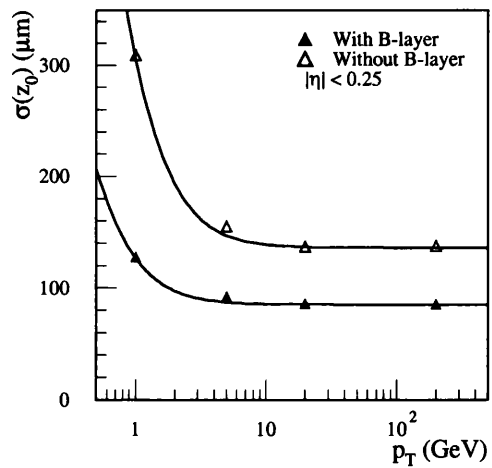


Figure 5.18: Longitudinal impact parameter resolution for  $|\eta| \leq 0.5$  as a function of  $p_T$ . The function plotted is a fit to the  $A \oplus B$  parameterisation.

## 5.4 Summary

The single track reconstruction performance of the ATLAS detector has been investigated using the simulation of muons. The resolution on  $1/p_T$  was found to be  $0.4 \text{ TeV}^{-1}$  for  $p_T = 200 \text{ GeV}$ . The impact parameter resolutions for both  $d_0$  and  $z_0$  have been shown to be approximated by the function  $A \oplus B/p_T$ . The B-layer improves the the  $d_0$  resolution by a factor of 3 at low (1 GeV)  $p_T$  and by 1.6 at high (200 GeV)  $p_T$ . For  $z_0$  the B-layer improves the resolution by a factor of at least 2.5 at low  $p_T$  and by 1.6 at high  $p_T$ .

# Chapter 6

## *b* quark tagging

### 6.1 Introduction

This chapter describes *b*-tagging using the ATLAS detector. The fundamental method and particular application are described. The effect of detector misalignment is discussed as is the *b*-tagging performance of three ID layouts.

### 6.2 Overview

The accurate measurement of the impact parameter of a track is fundamental for a *b*-tagging analysis. Hadrons formed at the initial interaction point which contain a *b*-quark will travel typically several hundred to a thousand  $\mu\text{m}$  before decaying. Most other objects formed will decay immediately and their decay products will come directly from the initial interaction vertex.

The decay products from a *b*-hadron will emanate from a displaced secondary vertex. These displaced vertices can be tagged either by explicitly reconstructing the vertex or by examining the impact parameters of the daughter particles, as the impact parameter of such tracks will be large compared

to tracks coming from the initial vertex. Hence a jet of particles consisting of tracks mostly with high impact parameters can be attributed a probability of coming from a  $b$ -quark. This is a basic method of  $b$ -tagging [53] and is the method used here.

The ATLAS Inner Detector is well suited for  $b$ -tagging as the transverse impact parameter can be measured with an accuracy of  $20\ \mu\text{m}$  for the typically low (5 GeV) transverse momentum tracks and the position of the initial interaction has an r.m.s uncertainty of  $15\ \mu\text{m}$  in the  $xy$  plane.

For the work described in this chapter the impact parameter method has been used to perform the  $b$ -tagging. The physics process simulated is the decay of a Higgs boson into either a  $q\bar{q}$  pair or a gluon pair. Three detector situations are studied, the baseline ‘idealised’ detector, the baseline with an estimate of the uncertainties due to detector misalignment added and a detector with detection layers removed.

## 6.3 Simulation Procedure

The simulation uses the decay of a 400 GeV Higgs particle. The decay is forced into either a  $u\bar{u}$ ,  $c\bar{c}$ ,  $b\bar{b}$  pair or a gluon pair (Figure 6.1). Each event therefore contains two jets which are simulated in the ID only, no calorimeter or muon chamber simulation was done. Higgs decay is used to provide a direct comparison of  $b$ -jets and non- $b$ -jets with the same kinematics. A Higgs mass of 400 GeV gives 200 GeV per jet. At this energy the jets produced provide a useful test of two track separation due to the track density in the jets and the pattern recognition in general.

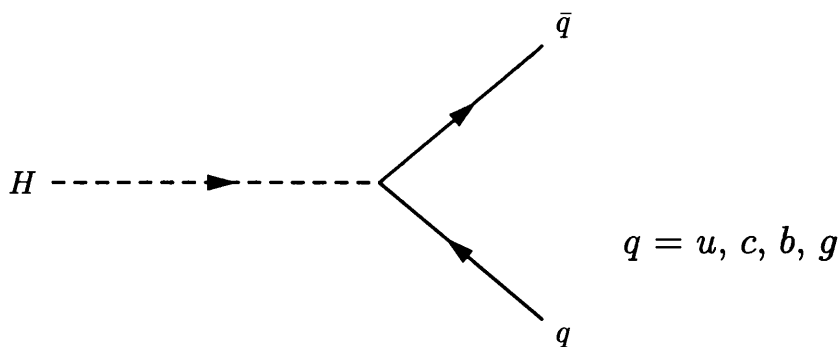


Figure 6.1: Higgs decay used for  $b$ -tagging analysis, with  $m_H = 400$  GeV, two 200 GeV jets are produced.

### 6.3.1 Primary Vertex

In order to determine the impact parameter of a track a point of origin is required. In principle this should be the primary vertex of the event, reconstructed from the prompt tracks.

For this  $b$ -tagging work the Higgs is generated at the nominal ATLAS origin point. However the position of the primary vertex in ATLAS will have a spread of  $15 \mu\text{m}$  in the  $xy$  plane. In order to simulate this the initial position of the Higgs, and hence the initial position of its decay products, is smeared by a Gaussian of width  $15 \mu\text{m}$ .

### 6.3.2 Significance distribution

The significance of the impact parameter is defined as the ratio of the signed impact parameter to its total error, i.e.  $S = d_0/\sigma(d_0)$ . The sign of the impact parameter is defined as positive if the track appears to originate from in front of the primary vertex (i.e. the track crosses the jet-axis in front of the primary vertex) and negative if it appears to originate from behind.

Positive significance arise from jets from  $b$ -quarks as the  $b$  travels around  $500 \mu\text{m}$ . Jets from  $c$  quarks are similar to jets from  $b$ -quarks but with shorter

impact parameters and hence smaller significances. For  $u$  quarks the significance is small and the spread in significance values is symmetrical due to resolution smearing on the track. For the gluon significance distribution the shape is similar to the  $u$  quark distribution, but slightly wider due to gluon splitting to  $b\bar{b}$  and  $c\bar{c}$ .

The jet axis will be determined by the calorimeter, however as the calorimeter has not been simulated here the jet axis is taken from the  $b$ -quark direction smeared by  $\pm 1^\circ$  to simulate the accuracy of the calorimeter. Tracks are reconstructed within a cone of  $0.4 R$  of this direction.

Figure 6.2 shows the significance distribution for tracks coming from  $b$  and  $u$  quark jets. There are significant ‘cores’ in both distributions which represent correctly reconstructed tracks coming from the primary vertex. The  $b$ -jet distribution contains tracks with large positive significance, corresponding to tracks with genuine lifetime content. The  $u$ -jet distribution has a much smaller number of tracks with positive significance which can arise from daughters of  $V^0$ 's, daughters of heavy quarks formed in the fragmentation and interactions with material e.g. photons converting to  $e^+e^-$  pairs or pions having nuclear interactions.

Both the  $b$  and  $u$ -jet significance distributions have tails on the negative side of the distributions. For the  $b$ -jets these are due to incorrect determination of the impact parameter sign (corresponding to the uncertainty in determining the  $b$ -hadron direction) and complications from secondary decays of charmed states. In the  $u$ -jet distribution the tail is dominated by secondary interactions in the detector.

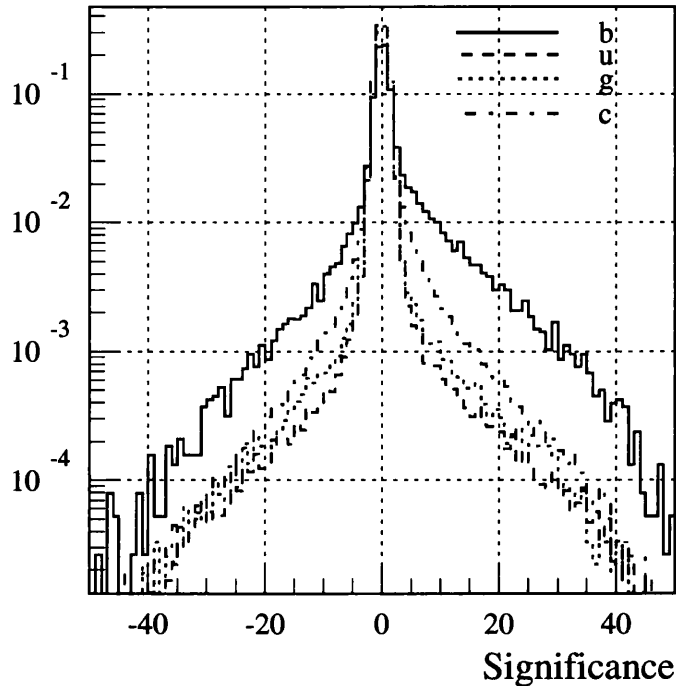


Figure 6.2: Significance distribution for tracks from  $b$ ,  $c$ ,  $u$  and gluon jets. Curves are normalised to the same area.

### 6.3.3 Tagging Methods

Many methods are available to use the significance distribution to determine if a jet was produced from a  $b$ -quark. Methods currently used by ATLAS include:

- Track counting method [54] - this algorithm simply counts the number of tracks with  $S > 3$  with  $|d_0| < 1$  mm. Discrimination between jets containing long-lived particles and those which do not is obtained by cutting on the number of these high significance tracks in each jet.
- ALEPH method [55] - invokes the probability for all tracks in a jet to

come from the primary vertex. First a one-sided Gaussian probability for each track is defined

$$w = \frac{2}{\sqrt{2\pi}} \int_d^\infty \exp -\frac{x^2}{2\sigma_d^2} dx \quad (6.1)$$

where  $\sigma_d$  is the measurement error on  $d_0$ . The product of all these probabilities is then formed

$$P = \prod_i^n w_i \quad (6.2)$$

The product is then normalised so that it is then insensitive to the number of tracks considered

$$\Omega = P \sum_{j=0}^{n-1} \frac{(-\ln P)^j}{j!} \quad (6.3)$$

Discrimination between jets containing long lived particles and those which do not is then obtained by cutting on  $\Omega$ .

- Likelihood ratio method - which is used and described below.

For the work described here the likelihood ratio method was used as it offered the best overall performance, in terms of tagging efficiency and light quark rejection [54].

### Likelihood Method

- For each track  $i$  in the jet which satisfies the track selection, the significance  $S_i$  of transverse impact parameter is calculated.
- The ratio of the fraction of tracks from  $b$ -jets with significance  $S_i$  to the fraction of tracks from non  $b$ -jets with significance  $S_i$  is computed

$$r_{x,i} = \frac{f_b(S_i)}{F_x(S_i)} ; x = u, c, g. \quad (6.4)$$

- A jet weight is constructed from the sum of the logarithms of the ratios

$$W = \sum \log r_i \quad (6.5)$$

- By retaining jets above some value of  $W$  (a value which can be varied), the efficiency for different jet samples can be obtained. Typically values of  $W$  of 2 to 3 tag 50% of jets from  $b$ -quarks as  $b$ -jets.

### 6.3.4 Track Selection

The iPatrec pattern recognition algorithm was used for track finding and reconstruction. iPatrec performs reconstruction in ‘roads’ which join the vertex region to a ‘seed’ region defined on the outer surface of the Inner Detector. For this work the Monte Carlo truth was used as the seed. The Monte Carlo truth was used as a seed because simulating the electromagnetic calorimeter would increase the processing time by a factor of 3 when the only information required from the calorimeter simulation is the direction of the jet axis. This can be obtained from the quark or gluon direction with a  $\pm 1^\circ$  smearing introduced to allow for measurement uncertainties in the electromagnetic calorimeter.

Tracks are ranked by *quality* which is defined according to the radial track length, the absence of holes and the track fit  $\chi^2$  (in order of precedence). The ranking ensures that tracks with TRT confirmation are found first.

To be accepted a track has to fulfill the following:

- Track  $p_T > 1$  GeV;
- At least 3 space points on the track of which 2 must be unique;
- A hit in the first partition (first two layers);

- $\geq 7$  discrete hits;
- $\leq 3$  holes in discrete detectors upstream of last hit;
- $< 50\%$  discrete hits shared with other tracks;
- Fit  $\chi^2$  per degree of freedom  $< 3.0$ .

### 6.3.5 Track reconstruction efficiency and quality

The  $b$ -tagging performance depends heavily on the track reconstruction efficiency and on the quality of the reconstructed tracks which come out of the pattern recognition algorithm. To illustrate the quality of the pattern recognition, three types of precision layer hits are associated with a reconstructed track:

- Unique Hit - hits which were produced by one KINE track which also produced the majority of precision hits on the track;
- Spoilt Hit - hits which were produced by two or more KINE tracks, or by one KINE track and noise or by pure noise;
- Wrong Hit - hits which were produced by one KINE track which was different from the one which produced the majority of the hits.

Figure 6.3 shows the total number of hits, unique hits, spoilt hits and wrong hits for both the barrel pixels and SCT barrel layers. On average 3.3 pixel hits are associated with each track, of which 98% are unique. This is slightly more than one hit per layer as tracks can cause more than one pixel per layer to activate. Of the reconstructed tracks 2.5% have no unique hits in the pixels. These arise from tracks produced in secondary interactions or from decays of  $V^0$ 's which start beyond the pixel layers but where the

pattern recognition algorithm has associated sufficient hits to a track for it to be accepted. 3.5% of all tracks have at least one wrong hit assigned to the track and 6.5% have at least one spoiled hit.

Unlike the pixel layers, described above, slightly above two hits per SCT layer are expected as each SCT layer is composed of two back-to-back strip detectors. For the SCT, each track has associated to it an average of 8.11 hits, of which 97% hits are unique. 2.5% of tracks have at least one wrong hit in the SCT layers and 18% of tracks have at least one spoiled hit.

Figure 6.4 shows the primary track reconstruction efficiency as a function of  $|\eta|$ . The average track reconstruction efficiency is 93%. The dip in reconstruction efficiency at around  $|\eta| = 1.75$  is due to increased material in this region.

Figure 6.5 shows the fraction of fake tracks, defined here as a track either corresponding to the same KINE track as another reconstructed track, or as not having at least 50% unique hits. The fake rate increases in the  $|\eta|$  region from 1.0 to 2.0 due to increased material here since this area covers the transition from barrel to end cap detector layers. Finally Figure 6.6 shows the fraction of tracks produced by detector interactions (secondaries) as a function of  $|\eta|$ . Again the effect of material can be seen, in the increased secondary rate from  $|\eta| = 1$ .

The presence of low quality tracks and of secondaries degrades the  $b$ -tagging performance and selection cuts have to be imposed on the reconstructed tracks to reduce them without significant deterioration on the efficiency of the primary tracks.

The following additional selection cuts were imposed to reduce the number of fake and secondary tracks:

- each jet must have at least two tracks;

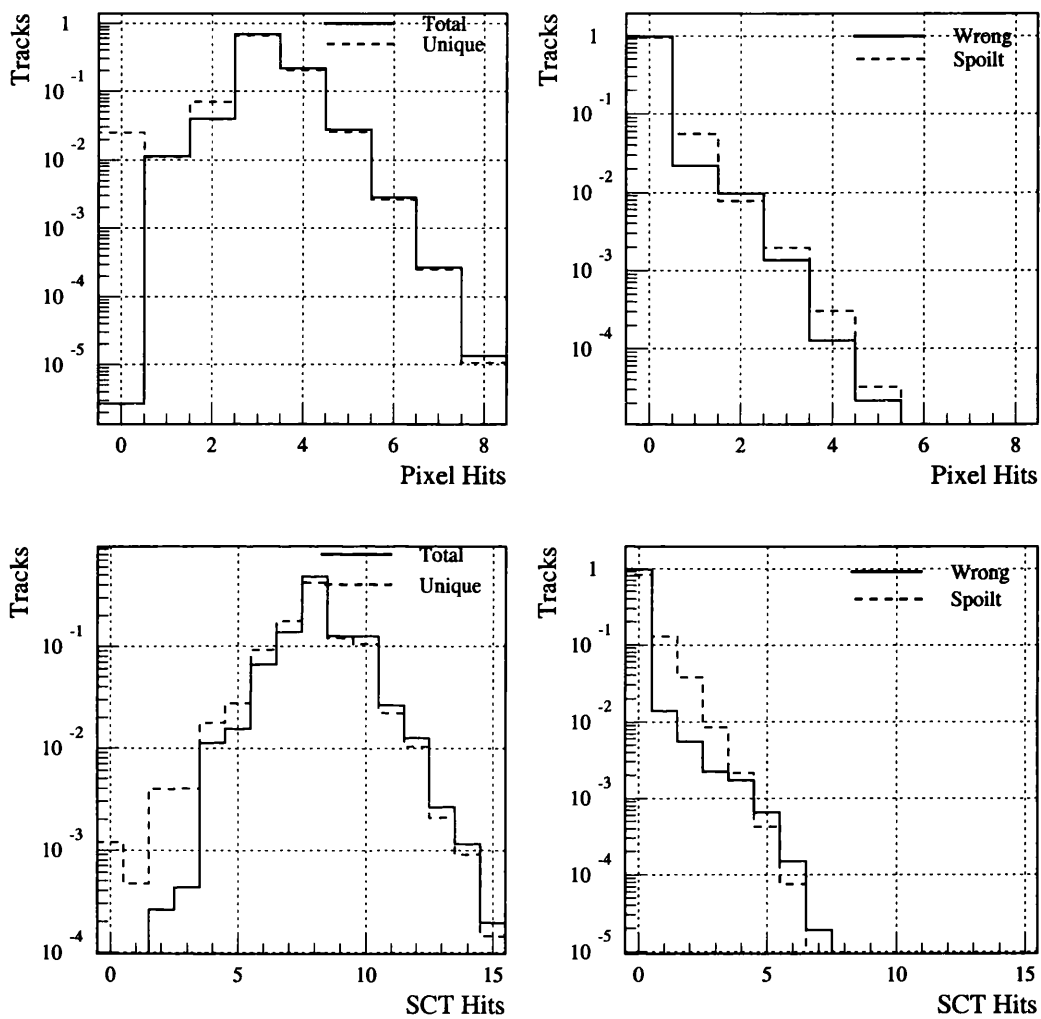


Figure 6.3: Fraction of tracks as a function of the number of total hits, unique hits, wrong hits and spoiled hits on the track.

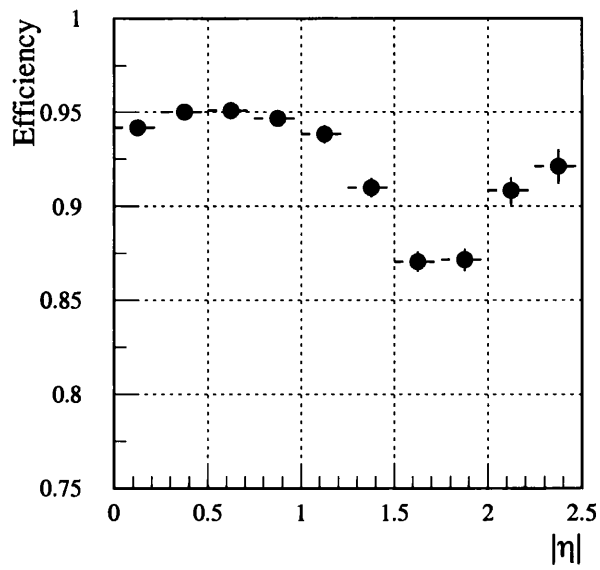


Figure 6.4: Reconstruction efficiency of primary tracks as a function of  $|\eta|$ .

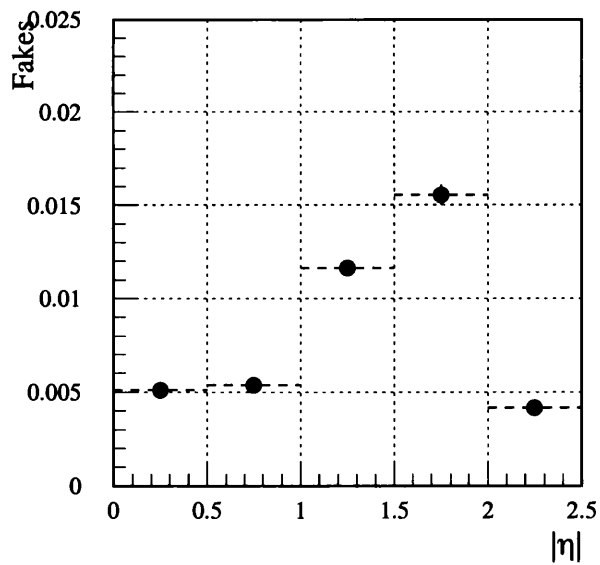


Figure 6.5: Fraction of fake tracks as a function of  $|\eta|$ .

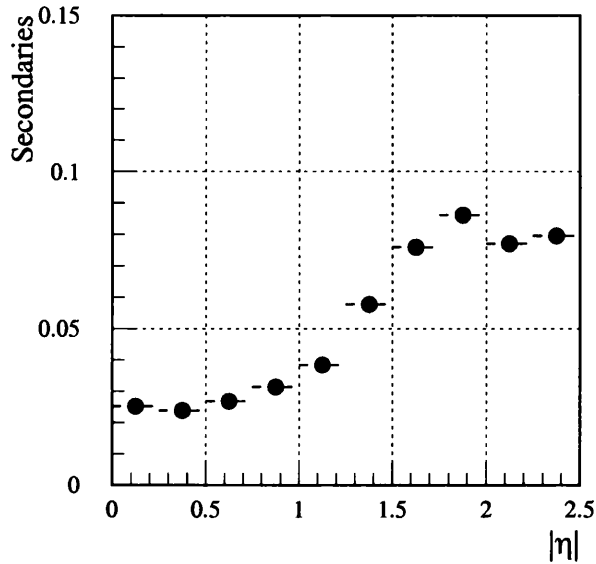


Figure 6.6: Fraction of secondary tracks as a function of  $|\eta|$ .

- $\geq 2$  pixel hits; together with the B-layer requirement this ensures that the best impact parameter resolution is achieved;
- at least one associated hit in the B-layer;
- $|d_0| \leq 1$  mm, this and the following cut suppress the tails of their distributions;
- $\chi^2$  fit probability of greater than 1%.

Figure 6.7 shows the efficiency of primary tracks after the selection cuts. The efficiency has been reduced from 93% without the selection cuts down to 87% with the selection cuts. This small loss in signal is more than compensated for by the reduction of potentially more damaging fake and secondary rates.

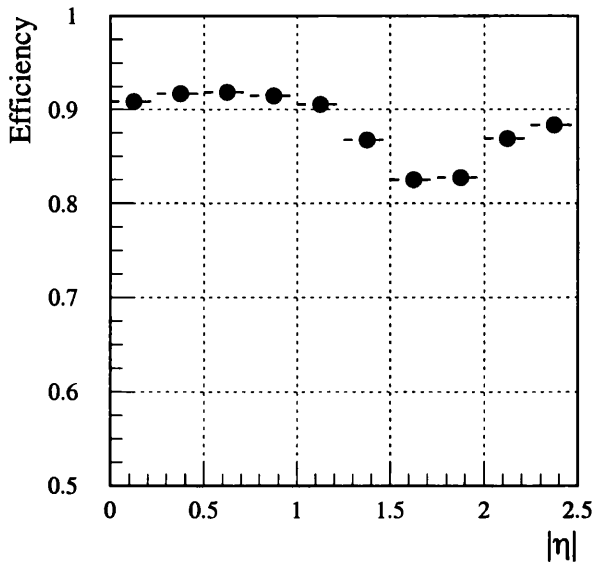


Figure 6.7: Primary track reconstruction efficiency after selection cuts.

Figures 6.8 and 6.9 show the fake and secondaries rates after the selection cuts. The average fake rate is down from 0.82% to 0.33% and the average secondary rate down by a factor of 2 to 3 for all  $|\eta|$

## 6.4 $b$ Tagging Performance

Figure 6.10 shows the jet weight for the four different jets types. The jet weight is the sum of the logarithm of the individual track significances. As tracks from  $b$ -jets have, on average, high significances then jets from  $b$ -quarks will have high jet weights. Light quark jets can be rejected as they have low significances and hence low jet weights.

Identification of jets from  $b$ -quarks is then a trade off between accepting  $b$ -jets and the rejection of non  $b$ -jets. A jet weight value is selected and all jets with that weight or higher are called  $b$ -jets. The higher the jet weight

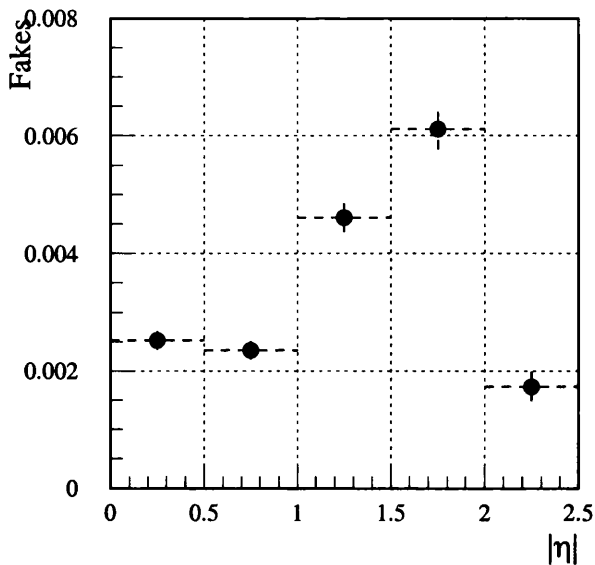


Figure 6.8: Fraction of fake tracks after selection cuts as a function of  $|\eta|$ .

cut, the higher the purity of the  $b$ -jets identified, but the fewer real  $b$ -jets that will be identified as  $b$ -jets.

The rejection of background jets as a function of  $b$ -jet efficiency ( $\epsilon_b$ ) is shown in Figure 6.11. The offset from  $\epsilon_b = 1$  arises from the 6.6% loss of jets with less than two tracks. The rejection of  $c$ -jets is poorer than the rejection of light quark and gluon jets. This is due to the longer lifetime of  $c$  hadrons: e.g.  $c\tau D^\pm = 317 \mu\text{m}$ ,  $c\tau D^0 = 124 \mu\text{m}$ . Hence jets from  $c$  quarks will have higher jet weights on average than light quark jets and will be misidentified as  $b$ -jets more often. The rejection of gluons is limited by the gluon splitting:  $\text{BR}(g \rightarrow c\bar{c}) = 6\%$  and  $\text{BR}(g \rightarrow b\bar{b}) = 4\%$ .

The rejections obtained for 50%  $b$ -tagging efficiency are summarised in Table 6.1. The rejections as a function of  $|\eta|$  are shown in Figure 6.12. The gluon and  $c$  quark rejections are both relatively flat in  $|\eta|$ , whereas the  $u$  jet rejection falls from a high of 108 at  $|\eta| = 0$  to a low of 41 at  $|\eta| = 1.75$  rising

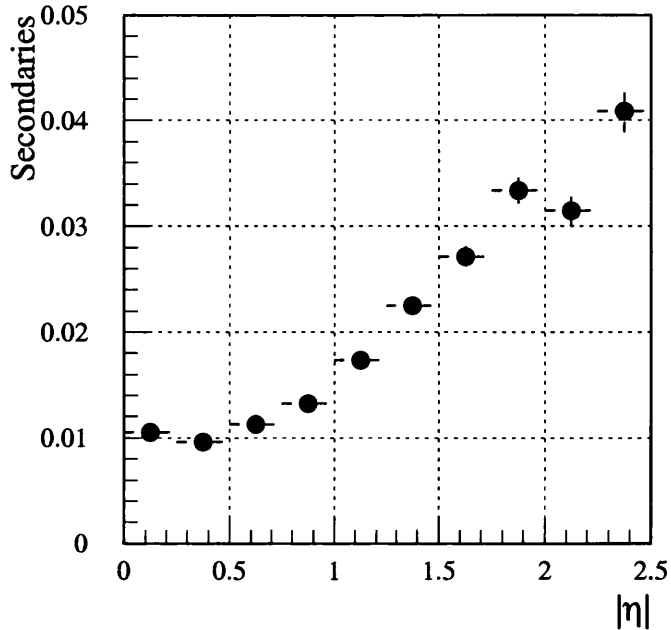


Figure 6.9: Fraction of secondary tracks after selection cuts as a function of  $|\eta|$ .

slightly at higher  $|\eta|$  values. The low rejection at  $|\eta| = 1.75$  is caused by the increase in material in the range  $1.5 < |\eta| < 2.0$ . This extra material results in a decrease in reconstruction efficiency, an increase in the fake and secondary rates and a poorer impact parameter significance. All these factors combine to reduce the  $u$ -jet rejection.

### 6.4.1 Detector Misalignment

Residual detector misalignment was introduced by offsetting the position of each detector module before reconstruction. The offset given was constant between events but changed between reconstruction runs to ensure that different sets of module offsets gave similar results. The value of the offsets were

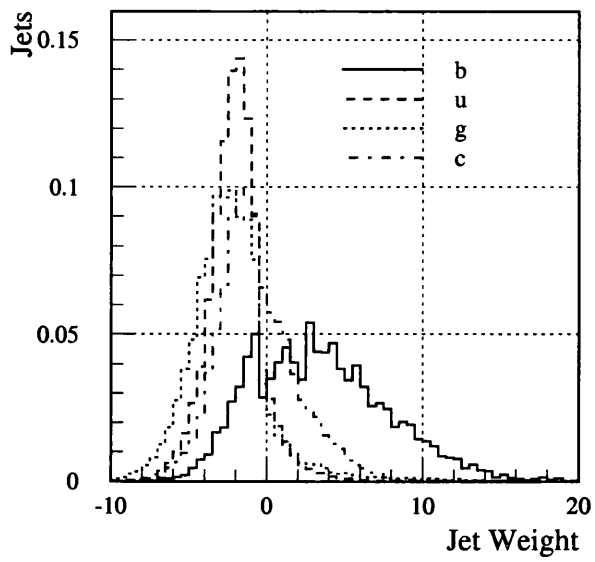
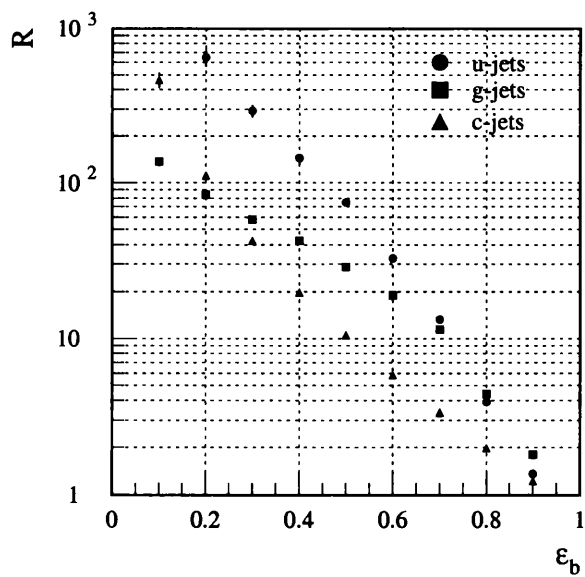
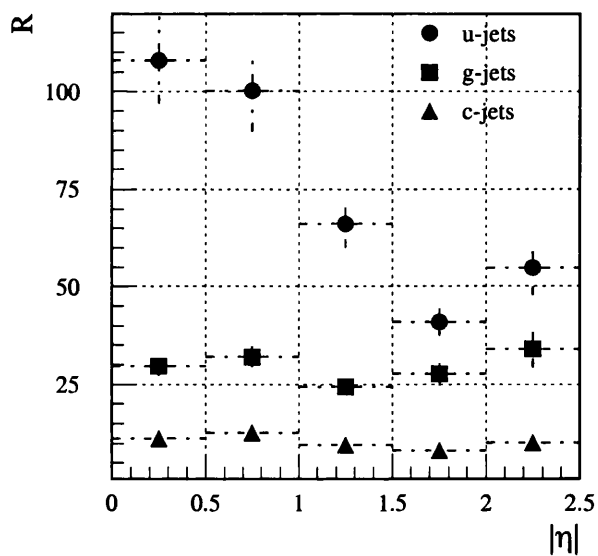


Figure 6.10: Jet weight distribution, normalised to unit area.

Figure 6.11:  $u$ ,  $c$  and gluon jet rejection as a function of  $b$ -jet efficiency.

Background jet	No misalignment	With Misalignment
$R_u$	$75 \pm 3$	$63 \pm 3$
$R_g$	$29 \pm 1$	$28 \pm 1$
$R_c$	$10.5 \pm 0.2$	$9.9 \pm 0.2$

Table 6.1: Summary of rejections at 50%  $b$ -tagging efficiency.Figure 6.12:  $u$ ,  $c$  and gluon jet rejection as a function of  $|\eta|$  with no misalignment.

Module	$\sigma(r)$ $\mu\text{m}$	$\sigma(z)$ $\mu\text{m}$	$\sigma(r\phi)$ $\mu\text{m}$
Pixel B-layer	10	20	7
Pixel barrel	20	20	7
Pixel wheels	20	100	7
SCT barrel	100	50	12
SCT wheels	50	200	12

Table 6.2: Residual module misalignments.

taken from the expected residual misalignment given in the ATLAS Inner Detector TDR [22], see Table 6.2. The misalignment offsets were generated using a gaussian distribution with the expected residual misalignment being the one sigma value. During the reconstruction procedure with iPatRec each space-point was then given the appropriate module offset. Reconstruction then proceeded as for the standard analysis.

Figure 6.13 shows light quark, gluon and  $c$  quark rejection as a function of  $|\eta|$  with residual detector misalignment included. The shapes of the rejection factors with and without residual misalignment are similar and differ only by an overall scaling factor. The average light quark rejection falls by 18%, the gluon rejection by 7% and the  $c$  quark rejection by 2%. Even with residual misalignment included the light quark rejection was still above 50, the minimum performance benchmark.

## 6.5 Reduced Layout Performance

The amount of material in the ID is a cause for concern for the electromagnetic calorimeter design group as more realistic estimates (better mass estimates of the detectors and an improved treatment of the services re-

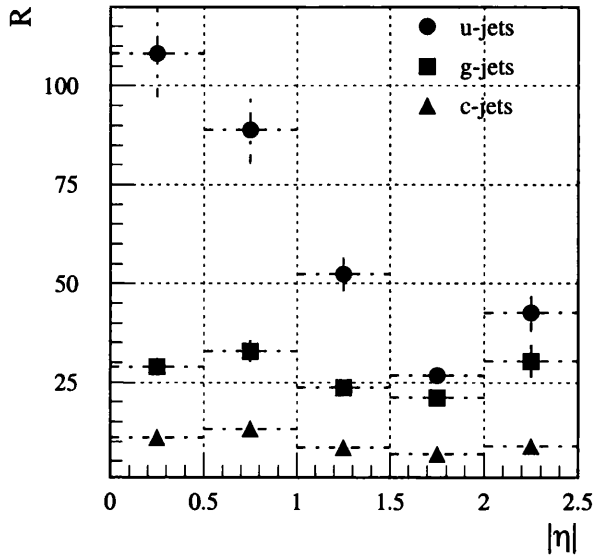


Figure 6.13:  $u$ -jet rejection as a function of  $|\eta|$  with misalignment.

quired) have increased the expected mass of the ID. The amount of mass in the ID is now at the limit of what is deemed acceptable in front of the calorimeters [57].

Increasing the ID mass leads to a poorer energy resolution of the EM calorimeter. The main effect is the production of a low energy tail in the calorimeter energy measurement (Figure 6.14). When a particle enters the calorimeter a shower is produced which spreads out over several calorimeter cells. In order to obtain a good energy resolution the total energy deposited in a cluster of cells ( $3 \times 5$  cells in  $\Delta\eta \times \Delta\phi$ ) is summed. However if a particle interacts with the material of the ID then any shower produced will be opened in  $\phi$  by the presence of the magnetic field. The opening is larger for small particle energies and small interaction radii. In order to collect the total shower energy the cluster size is enlarged to  $3 \times 7$ ; despite this there are still low energy tails. Larger cluster sizes are not used due to the contribution

of the electronic and pile up noise to the energy resolution [58]. Interactions at small radii produce larger tails in the calorimeter energy resolution as shown in Figure 6.14. Therefore a request was made to the ID group to reduce the mass of the ID if possible or to produce strong evidence that any removal of mass from the detector will degrade the ID performance below acceptable levels. The only way to make significant savings in the mass of the Inner Detector is to remove a detector layer, either a pixel or an SCT layer. Removal of the TRT is not a consideration as it has little effect on the calorimeter. Removing a pixel layer would give the greatest help to the calorimeter as the inner-most mass degrades the calorimeter resolution the most. The removal of an SCT layer will have less effect on the ID but will also benefit the calorimeter less.

### 6.5.1 Layouts

The baseline layout of the precision layers of the ID is described in chapter 4 and consists of 7 precision layers (3 pixel and 4 SCT). A small number of changes were made to the ID layout from those used for the preceding  $b$ -tagging analysis. These were:

- the material in the pixel barrels (disks) had been increased, on average from 1.39% (0.94%) to 1.63% (1.63%)  $X_0$  [59];
- the angle between the normal to each module and the radial direction in the  $xy$  plane (module tilt) of the barrel pixel has been changed, to give a smaller average cluster size in  $r\phi$  improving the point resolution of the barrel pixel;
- the routing of the B-layer services has changed to along the beam pipe and then out in front of the end-cap cryostat;

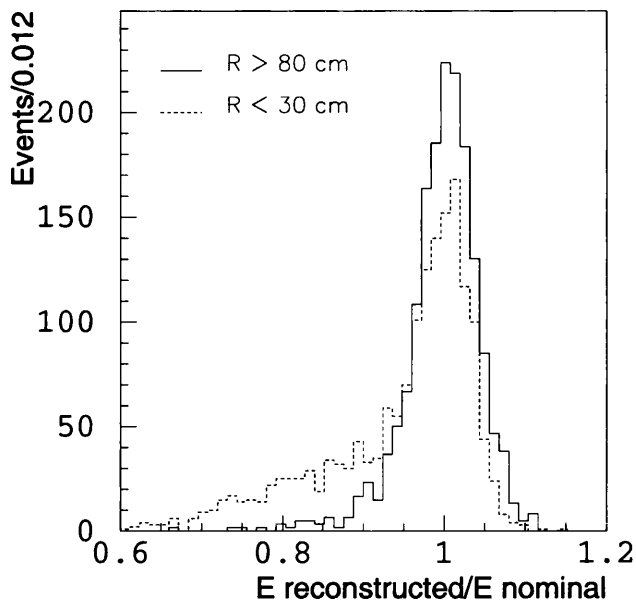


Figure 6.14: Reconstructed energy [60], normalised to generated energy, for electrons with  $E_T = 10$  GeV, at  $\eta = 1.2$ . The solid histogram is for electrons with an interaction radius greater than 80 cm and the dashed for electrons interacting at  $r < 30$  cm.

- at the outer radius of the end-cap TRT straws the material thickness has been increased by  $5\% X_0$ .

The increases in material come from an improved understanding of the detector module requirements. Three layouts have been studied:

- the baseline layout or 3+4 layout as shown in Figure 6.15;
- a layout without the 2nd pixel barrel, the 2nd and 4th endcap pixel disks and their services, the 2+4 layout is shown in Figure 6.16;
- a layout with only 3 equally spaced SCT barrels and 7 SCT wheels, the 3+3 layout, shown in Figure 6.17.

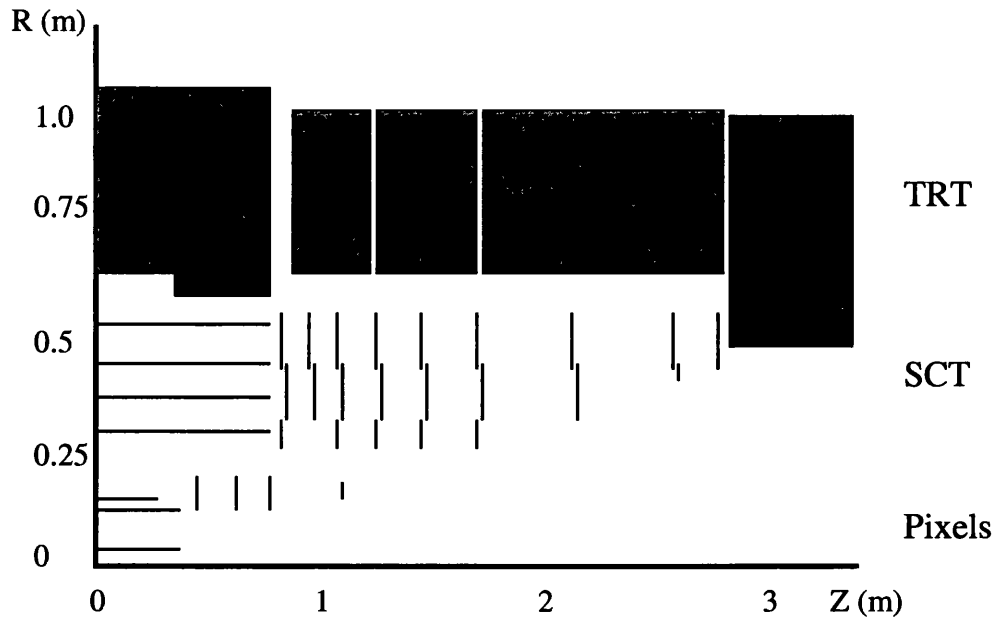


Figure 6.15: Schematic diagram of the Inner Detector 3+4 layout showing the pixel layers ( $0.04 < r < 0.20$ ), the SCT layers ( $0.3 < r < 0.6$ ) and the TRT (shaded).

### 6.5.2 Simulation

For this analysis two data sets were generated using PYTHIA to generate the particle four vectors and then using GEANT to simulate the particles through each geometry. The data sets consisted of 2,500  $H \rightarrow b\bar{b}$  events and 10,000  $H \rightarrow u\bar{u}$  events for each geometry. The simulated digitisation data were then reconstructed using the iPatRec reconstruction algorithm.

### 6.5.3 Track Selection

The track selection cuts used here are similar to the previous selections cuts used in section 6.3.5. The only addition was a cut on the impact parameter in the  $rz$  plane to remove tracks from secondary interactions, which tend to

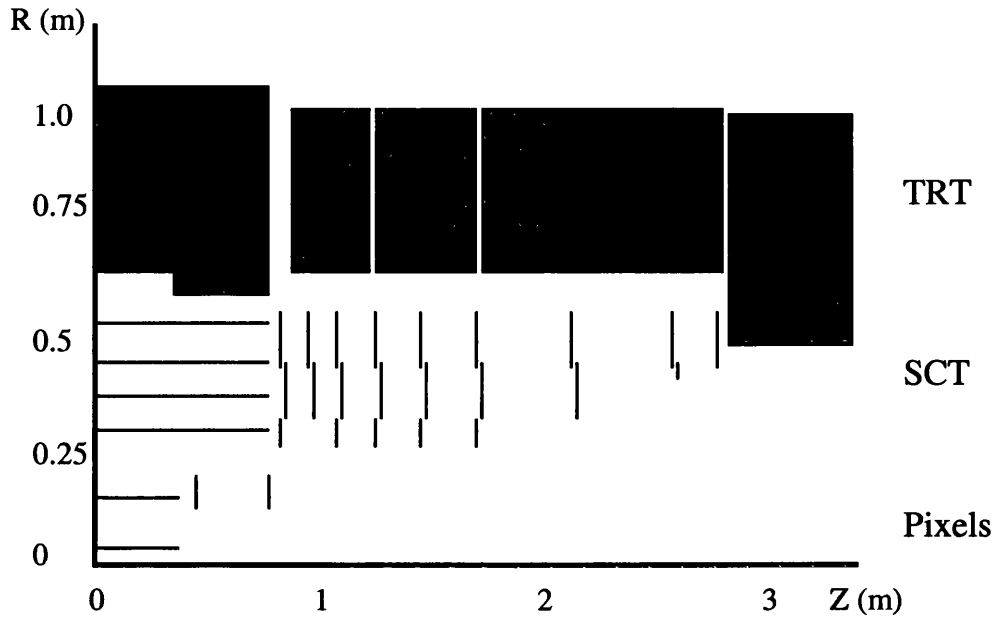


Figure 6.16: Schematic diagram of the Inner Detector 2+4 layout. One of the pixel barrel layers at  $r = 11$  cm and two of the pixel endcap wheels at  $z = 64$  and  $107$  cm have been removed compared to the 3+4 layout.

have large impact parameters

- impact parameter in the  $rz$  plane less than 2 mm relative to the intersection of the highest  $p_T$  track with the beam axis.

The selection cuts are not critically sensitive to the removal of one precision layer, with the exception of the removal of the B-layer, which is not considered for removal here. Only two of the cuts are potentially sensitive to the removal of a precision layer. They are:

- $\geq 7$  discrete hits. The cut is required to be well below the the average number of discrete hits on a track for all layouts otherwise tracks could be cut if there were insufficient active layers to give the required number of hits. The requirement of seven precision hits is correct as the pixel

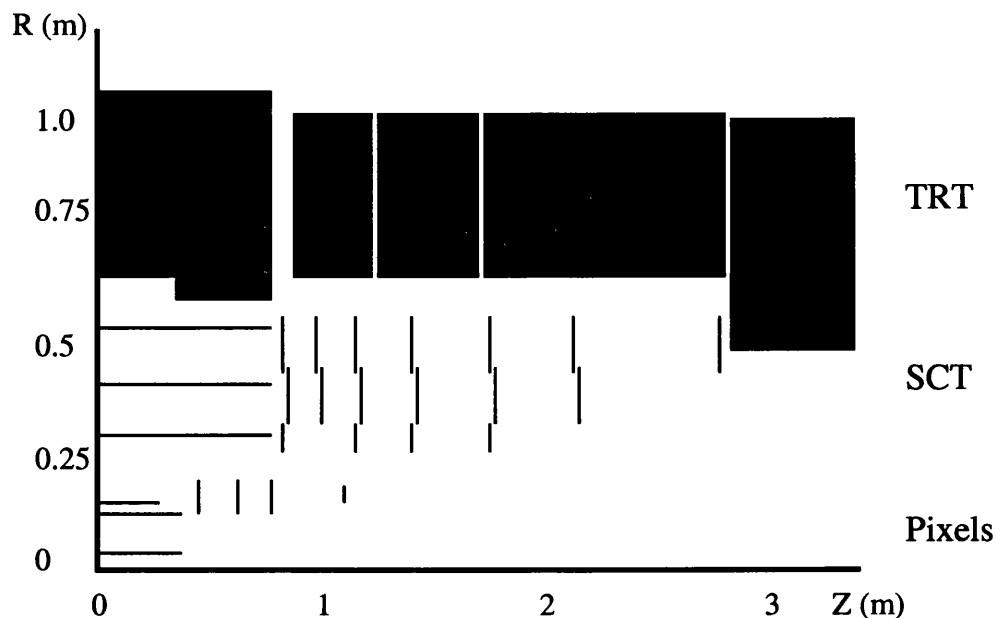


Figure 6.17: Schematic diagram of the Inner Detector 3+3 layout. One of the SCT barrel layers and two of the SCT endcap wheels have been removed compared to the 3+4 layout. The positions of the remaining SCT layers were then reoptimised.

layers give one hit per layer to a track and the SCT layers give two hits (the SCT layers are double sided) per layer per track. For the 3+4 layout this gives 11 hits for tracks traversing the ID barrel, 10 for the 2+4 layout and 9 for the 3+3 layout.

- $\geq 2$  pixel hits. This removes removes more tracks from the 2+4 layout than the 3+3 or 3+4 layouts. In all cases an inner B-layer hit must be associated to a track then at least one more pixel hit is required. For the 3+3 or 3+4 layouts this requires a hit in either of the two outer pixel layers, but in the 2+4 layout there is only one other pixel layer for this second hit. The pixel layers have a 97% efficiency thus 3% of

tracks with a B-layer hit will not have a second pixel hit for the 2+4 layout, while for the 3+3 and 3+4 layouts only 0.09% fail to give a second pixel hit.

The track cuts are a compromise to allow the cuts to be similar for the three different layouts and to have reasonable  $b$ -tagging performance. In principle the cuts could be re-optimised for each layout.

#### 6.5.4 Analysis

The results for each of the three layouts are given for two efficiency conditions, (a) the default 97% hit efficiency in the precision detectors without pileup and (b) for a hit efficiency reduced to 90% in the precision detectors, by introducing in addition to the default 3% hit inefficiency a 3.5% inefficiency in the readout chips and a 3.5% inefficiency to the whole detector modules, again without pileup, a possible scenario near the end of the ATLAS experimental lifetime of 10 years.

The results for the light quark rejection factor  $R_u$  as a function of  $b$ -tagging efficiency  $\epsilon_b$  averaged over  $|\eta|$  are shown in Figure 6.18. Over the range of  $b$ -tagging efficiencies the 2+4 layout has a 20% reduction in light quark rejection over the 3+4 layout. The 3+3 layout has a slightly higher rejection over the 3+4 layout at low and high  $b$ -tagging efficiencies while at  $\epsilon_b = 50\%$  the 3+4 layout has the slightly higher rejection.

Figure 6.19 shows the  $u$ -jet rejection as a function of  $|\eta|$  for a  $b$ -tagging efficiency of 50%. As would be expected the 2+4 layout, with only two pixel layers gives the poorest rejection factor. The 3+4 layout gives the best rejection factor over the whole range, except for  $|\eta| = 1.25$ , here the 3+3 layout gives the higher rejection factor.

The  $u$ -jet rejection for 50%  $b$ -tagging efficiency for the default and reduced

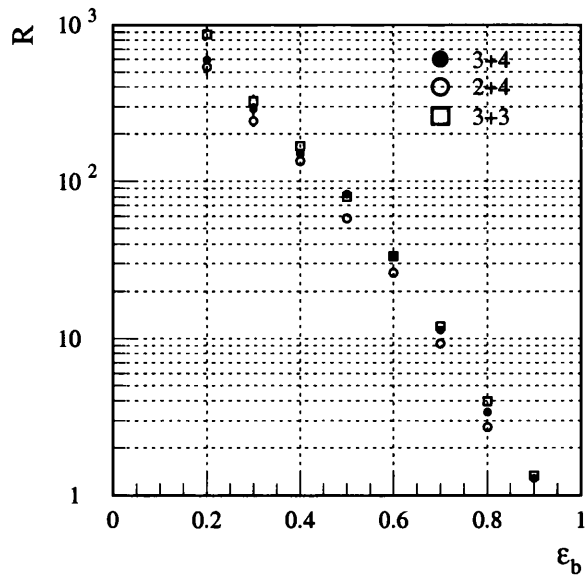


Figure 6.18:  $u$ -jet rejection as function of  $b$ -tagging efficiency.

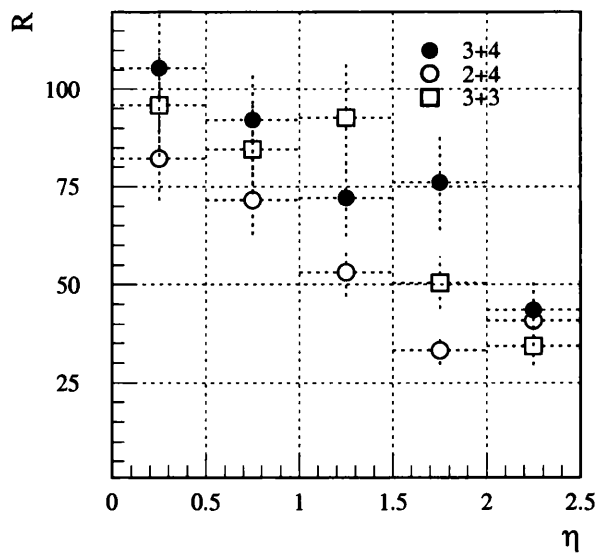


Figure 6.19:  $u$ -jet rejection for 50%  $b$ -tagging efficiency as a function of  $|\eta|$ .

Layout	$\varepsilon = 97\%$	$\varepsilon = 90\%$
3+4	$83 \pm 6$	$61 \pm 4$
2+4	$58 \pm 3$	$38 \pm 2$
3+3	$79 \pm 5$	$51 \pm 3$

Table 6.3:  $u$ -jet rejection for 50%  $b$ -tagging efficiency.

efficiency conditions are shown in Table 6.3. The 2+4 layout gave the poorest average light quark rejection and the 3+4 and 3+3 layout averages were, within errors, equal for 97% detector efficiency.

The two reduced layouts suffer a larger drop in rejection factor compared to the 3+4 layout for 90% detector efficiency. This is expected since layers are removed where there is little redundancy in the design and thus the reduced layouts would cope less well with decreased detector efficiency.

Figure 6.20 shows a direct comparison of the  $u$ -jet rejection between the 97% and 90% detector efficiencies for the 3+4 layout. As would be expected the lower detector efficiency run has a lower light quark rejection, with a reduction of 27% for the 3+4 layout, 35% for the 2+4 and 3+3 layouts. A light quark rejection of less than 50, for these 200 GeV jets is considered unacceptable. The 3+3 layout would be borderline to give this performance, the 2+4 layout would not and only the 3+4 layout would perform satisfactorily.

### 6.5.5 Track Quality

The  $u$ -jet samples were used to evaluate the overall quality of reconstructed tracks from the iPatrec reconstruction program. The dependence of the track quality on the three layouts and the two detector efficiencies is shown in Table 6.4. The 2+4 layout gave a poorer track reconstruction efficiency

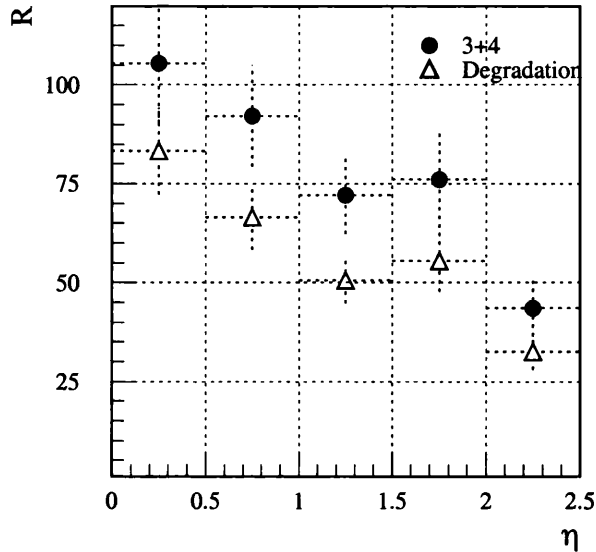


Figure 6.20:  $u$ -jet rejection for 97% and 90% detector efficiency.

compared to the other two layouts. At 90% detector efficiency the 2+4 layout primary track reconstruction efficiency fall to 68.4%. With one less pixel layer the 2+4 layout generates only half the secondaries after the B-layer than the two other layouts. At 90% efficiency the 2+4 layout gives a fake rate 33% higher than the 3+3 and 3+4 layouts. The only clear difference between the 3+3 and 3+4 layouts for 97% efficiency, was the number of spoilt SCT hits, 16.6% for the 3+4 layout and 13.2% for the 3+3 layout. The 3+3 would have less spoilt hits simply because of one less layer with which to produce hits. The primary track reconstruction percentage for 90% detector efficiency is 79.2% for the 3+4 layout and 76.1% for the 3+3 layout. This shows again that as the detector performance is degraded the 3+3 layout is affected before the 3+4 layout as there is less redundancy in the 3+3 layout with respect to the 3+4 layout.

In terms of individual track reconstruction only the degradation of pri-

	97% Efficiency			90% Efficiency		
	3+4	2+4	3+3	3+4	2+4	3+3
primary track efficiency	86.6	81.4	86.3	79.2	68.4	76.1
secondaries after B layer	0.40	0.20	0.38	0.39	0.19	0.36
fake rate	0.07	0.07	0.07	0.06	0.08	0.06
% tracks with:						
spoilt pixel hits	4.8	4.4	4.8	4.7	4.4	4.7
wrong pixel hits	1.1	1.5	1.1	1.2	1.7	1.2
spoilt SCT hits	16.6	14.9	13.2	15.6	13.9	12.4
wrong SCT hits	1.1	1.0	1.0	1.0	1.0	0.9
% tracks in:						
$1/p_T$ tail	5.3	5.1	5.0	5.3	5.1	5.0
$d_0$ tail	1.4	1.8	1.4	1.5	1.9	1.4

Table 6.4: Primary track efficiencies, secondary rates after the B-layer, fake rates for  $u$ -jets, rates for spoilt and wrongly associated hits and non-gaussian tails of primary tracks.

primary track reconstruction efficiency for the 2+4 layout would be unacceptable. The track cuts used keep the fake and secondary rates low for all layouts. Figures 6.21, 6.22 and 6.23 show the primary, secondary and fake rates for 97% detector efficiency.

The primary track reconstruction efficiency is highest for  $|\eta| = 0.75$ . With increasing  $|\eta|$  tracks are more likely to hit more than one pixel or SCT strip, so there is less susceptibility to detector inefficiencies. With less material close to the beam the 2+4 layout generates less secondaries. The average fake rates for each layout are the same at 0.07%. The fake rate  $|\eta|$  dependence is different for each layout. The 2+4 and 3+4 layouts both have higher

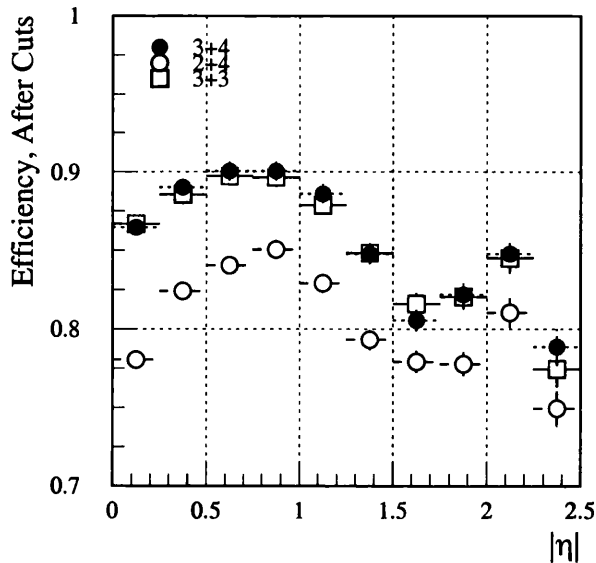


Figure 6.21: Primary track efficiency for 50%  $b$ -tagging efficiency as a function of  $|\eta|$ .

fake rates at large  $|\eta|$  and larger variations across  $|\eta|$ , while the 3+3 layout is more uniform across  $|\eta|$ . This is due to the minimum number of hits requirement. At high  $\eta$  for the 3+4 and 3+3 layouts particles can potentially traverse 4 to 6 SCT layers. For the 3+3 layout a particle will traverse 4 or 5 SCT layers. When track finding, allowing more layers without altering the minimum number of hits required increases the fake rate as more hit combinations will satisfy the minimum number of hits requirement.

The secondary rates, spilt into secondaries produced pre-and by the B-layer and secondaries produced post-the B-layer are shown in Figures 6.24 and 6.25. There is little difference in the pre B-layer secondary rate between the three layouts as there is no difference in the layout geometry from the B-layer inwards. For the post B-layer secondaries the 3+3 and 3+4 layouts are very similar, with the 2+4 layout producing lower numbers of secondaries

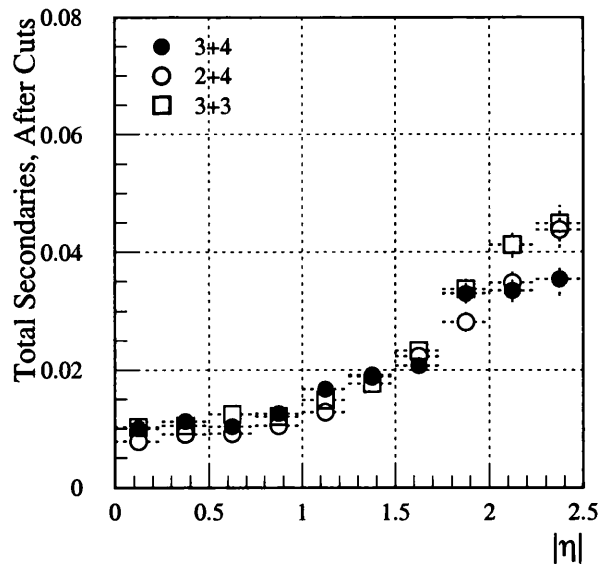


Figure 6.22: Secondary track rate for 50%  $b$ -tagging efficiency as a function of  $|\eta|$ .

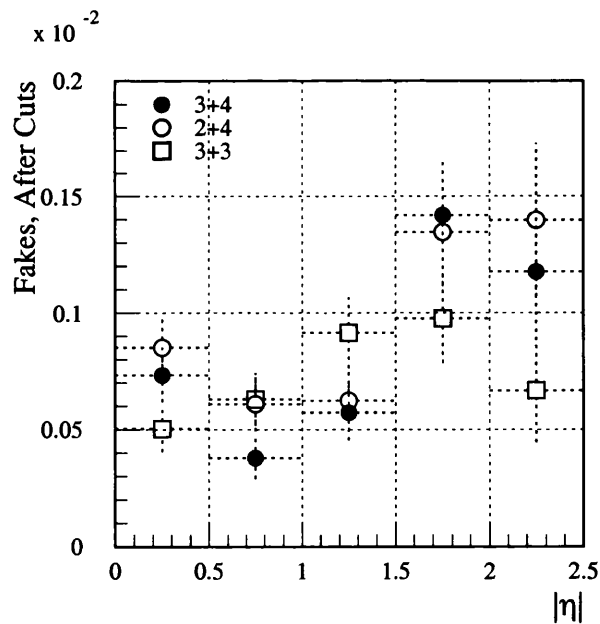


Figure 6.23: Fake track rate for 50%  $b$ -tagging efficiency as a function of  $|\eta|$ .

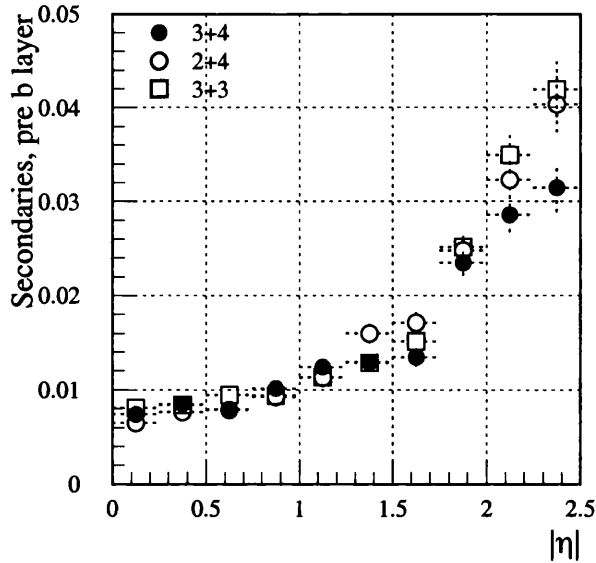


Figure 6.24: Pre B-layer secondary track rate for 50%  $b$ -tagging efficiency as a function of  $|\eta|$ .

simply due to the omitted pixel layers.

## 6.6 Summary

The ATLAS method for  $b$ -tagging has been described and results presented for  $b$ -tagging performance for jets with 200 GeV total energy. A rejection factor (defined as the reciprocal of the efficiency) of  $75 \pm 3$  was achieved with no detector mis-alignment and  $63 \pm 3$  including residual detector misalignment. For the layout study the  $b$ -tagging performance is degraded by 30% when a pixel layer is removed and by 10% if an SCT layer is removed.

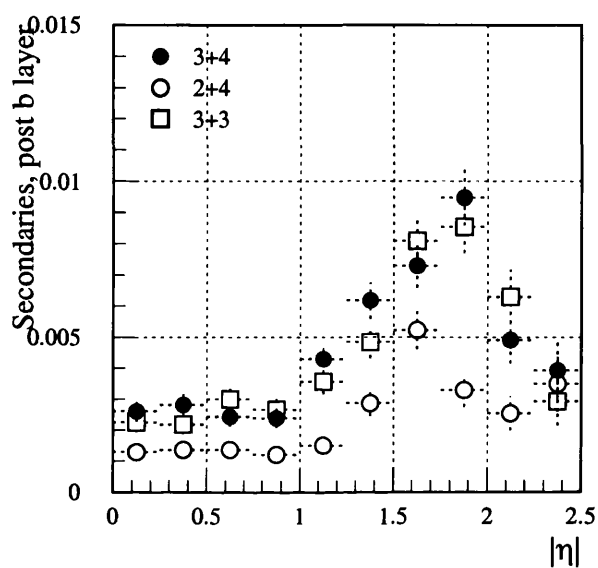


Figure 6.25: Post B-layer secondary track rate for 50%  $b$ -tagging efficiency as a function of  $|\eta|$ .

# Chapter 7

## Higgs Analysis

### 7.1 Introduction

One of the principle reasons for building the LHC and the two general purpose detectors ATLAS and CMS is to search for the Higgs boson predicted by the SM. Due to the wide range of possible Higgs mass, different decay and production modes need to be used for different Higgs mass values. Chapter 3 described the different decay and production modes open to a SM Higgs particle. This chapter concentrates on one channel,  $t\bar{t}H$ , when a low mass Higgs is produced in association with a  $t\bar{t}$  pair. First the simulation procedure is described. The  $t\bar{t}H$  channel is then detailed and the analysis methods described. The backgrounds to this process and methods of background reduction are then stated. The signal significance across the mass range  $80 < m_H < 120$  GeV is given and the systematic effect of uncertainties on the jet energy scale and  $b$ -tagging performance are described.

## 7.2 Simulation

The PYTHIA 5.7 [37] Monte Carlo package was used to generate the signal and background events, including QCD initial and final state radiation, hadronisation and decays of unstable particles. The generation used Higgs mass values from 80 to 120 GeV with a top mass of 175 GeV. The CTEQ [61] parton distributions were used.

The ATLFast [62] simulation package was used to simulate the passage of the PYTHIA generated particles through the ATLAS detector. The full simulation requirements, using DICE and ATRECON requires approximately 100 times longer to simulate an event. To achieve this speed the fast simulation does not perform detailed digitisation and reconstruction.

Starting from the PYTHIA four-vectors ATLFast associates particles to jets and isolated leptons and photons. First the transverse energies of all stable particles except neutrinos and muons are summed up into calorimeter cells. The cells are granulated in  $\eta$  and  $\phi$  with a granularity of  $0.1 \times 0.1$  for  $|\eta| < 3$  and  $0.2 \times 0.2$  for  $|\eta| > 3$ . Clusters of calorimeter cells are then identified where at least one individual cell has  $E_T^{cell} > 1.5$  GeV within a cone of 0.4 in pseudorapidity-azimuthal angle space ( $\Delta R$ ) where  $E_T^{cone} > 10$  GeV.

From the Monte Carlo truth information isolated leptons and photons are identified. The momentum and polar angle information is then smeared by the expected resolutions. The particle four-vectors obtained after smearing are then checked against particle dependent selection criteria to determine if the particle is to be retained in the simulation. For photons the requirements are  $p_T > 10$  GeV and  $|\eta| < 2.5$ , for electrons  $p_T > 5$  GeV and  $|\eta| < 2.5$  and for muons  $p_T > 6$  GeV and  $|\eta| < 3$ . For particles which pass the selection criteria the particle track is then matched to a calorimeter cell. To be classed as an isolated track, the minimum  $\Delta R$  to another cluster in the calorimeter

must be  $> 0.4$  and  $E_T < 10$  GeV within a cone  $\Delta R = 0.2$  of the particle. Once the calorimeter cell clusters have been identified with a lepton or photon then the energy resolution is appropriately smeared for that particle.

The remaining calorimeter clusters, not identified as leptons or photons, are then identified as jets if, after energy smearing, the total transverse cluster energy is  $> 15$  GeV and the cluster has  $|\eta| < 5$ .

Once the jet energy is determined, the PYTHIA four-vectors in a small cone of radius  $0.2 R$  around the jet direction are searched for a  $b$ -quark, with  $p_T > 5$  GeV. If such a quark is found then the jet is labelled as a true  $b$ -jet. A similar search for true  $c$ -quarks is also carried out.

The  $b$ -tagging performance of the Inner Detector is then characterised by the following input functions:

- the fraction of true  $b$ -jets identified as  $b$ -jets, the  $b$ -tagging efficiency  $e_b$ ;
- the fraction of true  $c$ -jets misidentified as  $b$ -jets, the inverse of the  $c$ -jet rejection factor  $1/R_c$ ;
- the fraction of all other jets misidentified as  $b$ -jets, the inverse of the  $u$ -jet rejection factor  $1/R_u$ .

The performance values are determined by selecting the  $e_b$  required and then using the full simulation to obtain the corresponding  $R_u$  and  $R_c$  values. Typical values for  $R_u$  and  $R_c$  are for  $e_b = 0.6$ ,  $R_u = 93$ ,  $R_c = 6.7$ . In addition  $p_T$  dependent correction factors to the identification efficiencies are included. The correction factors vary with different  $e_b$ ,  $R_u$  and  $R_c$  values. Table 7.1 gives the correction factors for the typical set  $b$ -tagging performance values given. Jets with  $p_T \simeq 50$  GeV have the highest correction factors (i.e. have the best  $b$ -tagging performance) due to two factors: (a) at low jet  $p_T$  the impact parameter resolution of individual tracks worsens, leading to poor

Jet $p_T$ (GeV)	$C_u$	$C_c$
< 30	0.48	0.76
30 - 45	1.23	0.90
45 - 60	2.30	1.25
60 - 100	1.70	1.18
> 100	1.08	1.15

Table 7.1: The  $p_T$  correction factors for light quark jets ( $C_u$ ) and charm jets ( $C_c$ ). The rejection factor is multiplied by the correction factor to obtain the effective rejection factor. Hence higher correction factors give better  $b$ -tagging performance.

tagging performance and (b) at high jet  $p_T$  the track density and multiplicity increases, degrading the track finding in the jet and the track parameter resolutions obtained.

The energies of the jets are then rescaled on average to the original parton energies, using  $p_T$  dependent scaling factors, which are different for  $b$ -jets and non- $b$  jets. This procedure shifts the invariant mass distributions for  $b\bar{b}$  pairs from  $H \rightarrow b\bar{b}$  decays such that the peak is within 1% of the correct mass value. The scaling factors are determined from the simulation of  $W \rightarrow jj$  decays as this decay will be used experimentally to determine jet scaling factors.

## 7.3 Signal

The Higgs production mechanism for the signal is associated production with a  $t\bar{t}$  pair. An example production diagram for this process is shown in Figure 7.1. Initially either gluon fusion or quark anti-quark annihilation leads to

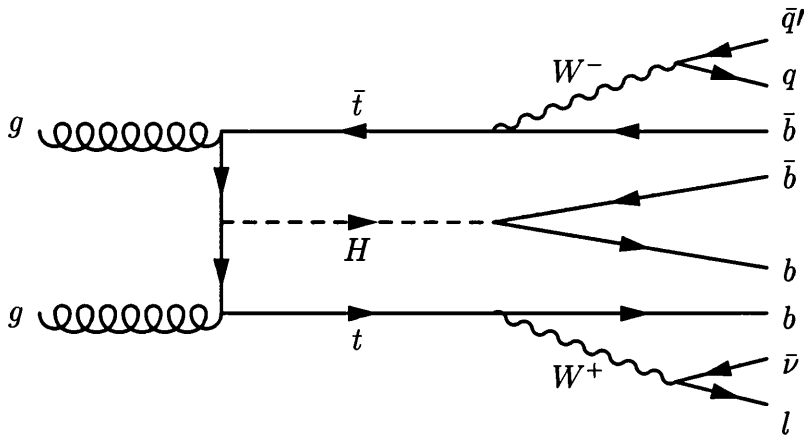


Figure 7.1: An example  $t\bar{t}H$  production diagram

the production of a  $t\bar{t}$  pair. Gluon fusion dominates with the ratio of gluon fusion to quark anti-quark annihilation being approximately 25 to 1. This is due to the invariant mass of the  $t\bar{t}$  pair typically being 350 GeV. The momentum of the parton emitted from the proton for this interaction then has only 1/40th of the total centre of mass energy. The partons at low momentum fractions are mostly gluons. The Higgs is radiated from a top quark. Each of the produced top quarks then decays into a bottom quark and a  $W$  boson. One of the  $W$  bosons is required to decay leptonically, to provide an isolated lepton for a trigger. For  $10 < m_H < 130$  GeV the dominant decay of the Higgs is to a  $b\bar{b}$  pair. This gives a final state with four hadron jets originating from the four  $b$ -quarks, an isolated lepton and either two additional hadronic jets (70%) or a second isolated lepton (30%), depending on the decay of the second  $W$  boson.

### 7.3.1 Event Characteristics

The  $b$ -jets originating from the top decays have similar properties to those from the Higgs decay. The following describes the event characteristics for events with  $m_H = 100$  GeV (events with  $m_H = 80$  or  $m_H = 120$  GeV are similar).

Figures 7.2, 7.3 and 7.4 show the  $p_T$ ,  $\eta$  and total energy  $E$  for  $b$ -jets from the Higgs ( $b_H$ ) and top decays ( $b_t$ ). For both  $b_H$  and  $b_t$  the  $p_T$  distribution rises rapidly to peak at around 50 GeV then falls off exponentially as  $p_T$  increases. The peak at 50 GeV is a consequence of the fact that decays of on-shell tops and a 100 GeV Higgs both give  $b$ -jets of typically 50 GeV in the rest frame of the decaying particle.  $b_H$  is roughly constant with  $|\eta|$  to 0.5 and then falls off linearly to  $|\eta| = 2.5$ . Beyond  $|\eta| = 2.5$  no  $b$ -tagging can be done. For  $b_t$  there is a similar linear drop off between  $|\eta| = 0.5$  and  $|\eta| = 2.5$ . The total jet energy plots are again very similar for  $b_H$  and  $b_t$ . Both rise initially to a peak at around 50 GeV and then fall off, with tails extending out past 400 GeV. This is again due to the similar energies imparted by both the top and Higgs decays to the  $b$ -jets. This similarity between the two types of  $b$ -jet in the event leads to combinatorial problems later in the analysis. Hence instead of forming the invariant mass of two  $b$ -jets identified with the Higgs decay all the  $b$ -jet combinations must be used.

Figure 7.5 shows the total jet multiplicity. One expects typically six jets from the underlying Higgs production process, as the second  $W$  decay is predominantly (70%) hadronic.

Figure 7.6 shows the  $b$ -jet multiplicity and the number of  $b$ -jets from the Higgs found after ATLFAST processing. The  $b$ -jet multiplicity distribution has a mean of 2.2. Given that most events have four real  $b$ -jets and a  $b$ -tagging efficiency of 60% this is consistent with expectations. 19% of events

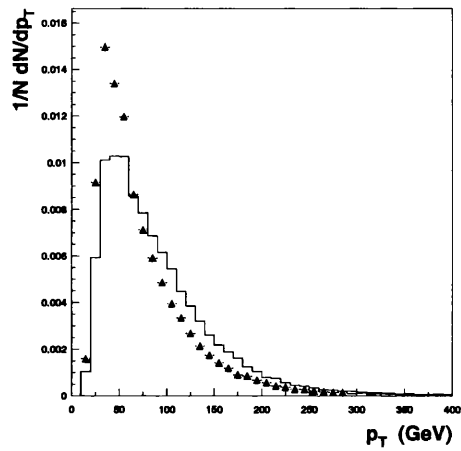


Figure 7.2:  $p_T$  of  $b$ -jets from top decay (open histogram) and Higgs decay (points).

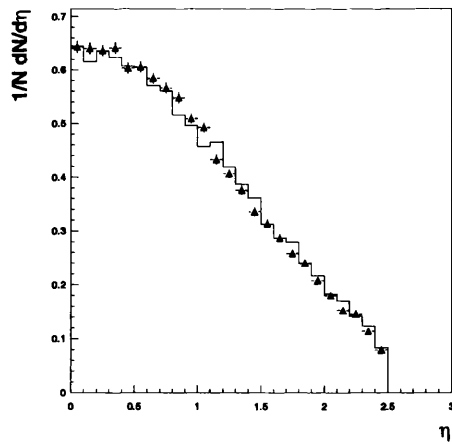


Figure 7.3:  $\eta$  of  $b$ -jets from top decay (open histogram) and Higgs decay (points).

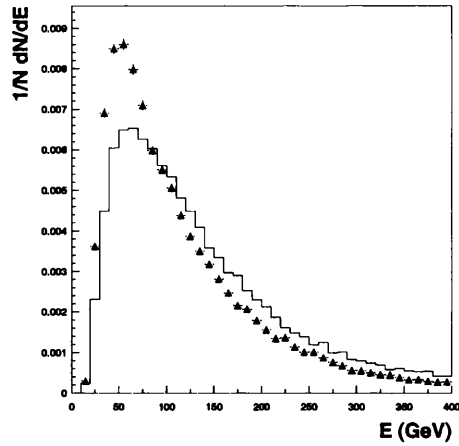


Figure 7.4: Energy of  $b$ -jets from top decay (open histogram) and Higgs decay (points).

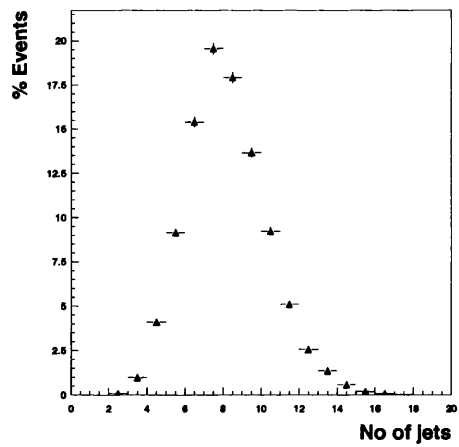


Figure 7.5: Jet multiplicity, after  $b$ -tagging.

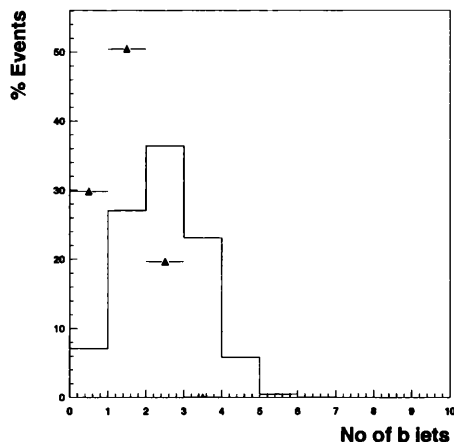


Figure 7.6:  $b$ -jets multiplicity (open histogram) and  $b$ -jets from Higgs (points), after  $b$ -tagging.

have both  $b$ -jets from the Higgs within the detector acceptance and tagged as  $b$ -jets.

Approximately 31% of all events have an isolated electron or muon which provides a trigger. From the branching ratios of the  $W$  and given two  $W$ s in the event 39% of the events would be expected to have a single electron or muon: the difference is due to the limited trigger acceptance for an electron or muon. 23% of events have three jets tagged as  $b$ -jets and 6% of events have four jets tagged as  $b$ -jets. Table 7.2 summarises this information. The overall acceptance of signal events with a trigger lepton and four tagged  $b$ -jets is 1.9%.

### 7.3.2 Higgs Signal

In principle the Higgs signal can be found as a peak in the invariant mass distribution of reconstructed  $b$ -jet pairs. However each signal event has four

Events With	Percentage
Trigger Lepton	30.6
3 $b$ -jets	23.2
4 $b$ -jets	6.1
2 $b$ -jets from Higgs	19.5

Table 7.2: Event characteristics summary, the percentage of events with a trigger lepton, the number of events with 3 and 4  $b$ -jets found in an event, after tagging and the number of events where both  $b$ -jets from the Higgs decay are found and tagged as  $b$ -jets.

$b$ -jets which gives six possible  $b$ -jet combinations, which must all be included in the invariant mass distribution.

Even if the underlying event is a Higgs event then the two  $b$ -jets from the Higgs may not be in the detector acceptance and/or the jets may not be tagged as  $b$ -jets. In this case if another real  $b$ -jet is present (from e.g.  $W$  decay) then this gives rise to a background (i.e. events in which the Higgs mass cannot be measured) from signal events.

Before looking at separating the potential Higgs signal from similar looking background events, there are two questions. Can the Higgs signal be seen in the signal events and is the cross-section high enough for the channel to be viable?

The cross-section for associated Higgs production with  $t\bar{t}$  is of the order of 1 pb for a Higgs mass of  $\simeq 100$  GeV [19]. For three years' low luminosity running ( $3 \cdot 10^4 \text{ pb}^{-1}$ ) this gives a potential data sample of 30,000 signal events. The requirement from the trigger that at least one of the  $W$ 's decay to either an electron or a muon reduces this to 11700 events. A  $b$ -tagging efficiency of 0.6 would leave 1520 events while a slightly lower tagging efficiency

of 0.5 would leave 730 events. The number of events is further reduced by the detector acceptance for the trigger lepton and the  $b$ -jets, leaving of the order of 450 - 1200 events for three years low luminosity running.

Figure 7.7 shows the invariant  $b\bar{b}$  mass distribution for  $b$ -jet pairs from events with four tagged  $b$ -jets, for  $b$ -jet pairs only from top and Higgs decays and for  $b$ -jet pairs only from Higgs decays, for a Higgs mass of 100 GeV. For  $b_H$  the invariant mass plot has a mean of 96 GeV, an RMS 27 GeV and the peak has a one sigma width of 17 GeV ( $\sigma_{H \rightarrow b\bar{b}}$ ). The Higgs decay width is a few GeV at 100 GeV, small compared to peak width in the figure which is due to measurement errors on the jet energy. Plotting all six  $b$ -jet pair combinations from Higgs and top decays gives a mean of 129 GeV and an RMS of 74 GeV.

### 7.3.3 $b_H$ identification

In the Higgs rest frame when the Higgs decays the decay products are produced isotropically in  $\theta$ ,  $\phi$ . The Higgs does have a boost with respect to the  $t\bar{t}$  production rest frame. Hence in the  $t\bar{t}$  rest frame the Higgs decay products have a smaller average angular distribution than the  $b$ -quarks from  $t$  and  $\bar{t}$  decay. However the  $t\bar{t}$  rest frame then has a larger boost with respect to the lab frame. This boost masks differences in jet properties of  $b$ -jets from top decays and  $b$ -jets from Higgs decays. Thus there is no simple way to identify which two out of the four  $b$ -jets in a signal event originated from the Higgs decay. The following describes an angular separation method and a reconstruction method.

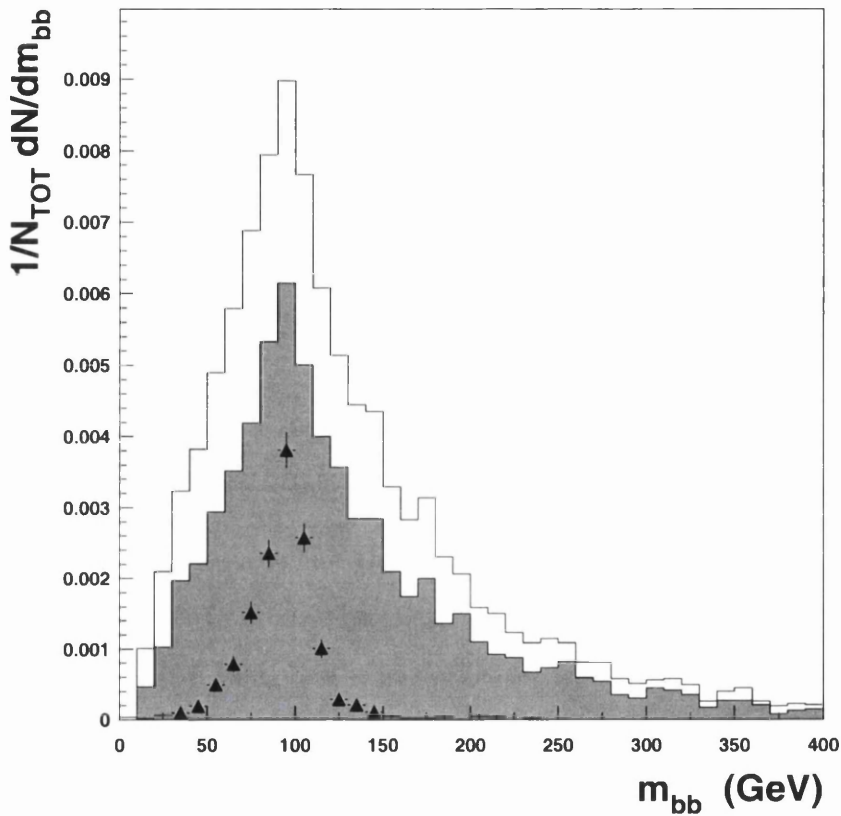


Figure 7.7: Invariant  $m_{bb}$  mass for all events with four tagged  $b$ -jets (open histogram), four  $b$ -jets from top and Higgs decays (filled histogram) and from the Higgs only (points).  $N_{TOT}$  is the total number of  $b$ -jet pair combinations.

### Angular Separation

A first attempt was made to identify good and/or bad combinations from the characteristics of the jets. As seen in section 7.3.1 the  $b$ -jets from top and Higgs decays have very similar properties. There is no obvious cut one can place on  $p_T$ ,  $\eta$  or  $E$  to separate the two types of  $b$ -jet.

The Higgs decay is, in general, boosted with respect to the lab frame. The two  $b$ 's which result from the decay will (due to the Higgs boost) have a smaller angular separation, on average, than two random jets. The  $b$ 's from the top decays will, in general, have a wider angular separation as they are the result of gluon fusion to a  $t\bar{t}$  pair then subsequent decay of the tops.

This can be seen in Figure 7.8 which shows the angular separation ( $R_{sep}$ ) of the  $b$ -jets resulting from the top decays and the  $b$ -jets from the Higgs decay ( $m_H = 100$  GeV). For the  $b$ -jets from the top decays there is a broad angular spread out to  $R_{sep} = 2$  which then falls as  $R_{sep}$  increases. The separation of the  $b$ -jets from the Higgs peaks more sharply and drops off somewhat faster. The difference in angular separation suggests a cut at around 2 to 2.5 will be effective in separating the  $b$ -jets from the Higgs decay from the  $b$ -jets from the top decays.

Graphically, the effect on  $m_{bb}$  of cutting on the angular separation of the  $b$ -jets is shown in Figure 7.9. Four plots are shown for different values of  $R_{sep}^{max}$ . Cutting tightly on the angular separation greatly reduces the number of  $b$ -jet combinations with high invariant mass values. However, in addition to removing most of the combinations in the range 200 - 400 GeV, some are removed in the range 100 - 200 GeV. This moves the position of the peak down in mass.

As the cut on angular separation is relaxed more combinations appear in the high mass range, and on the higher mass side of the peak. The

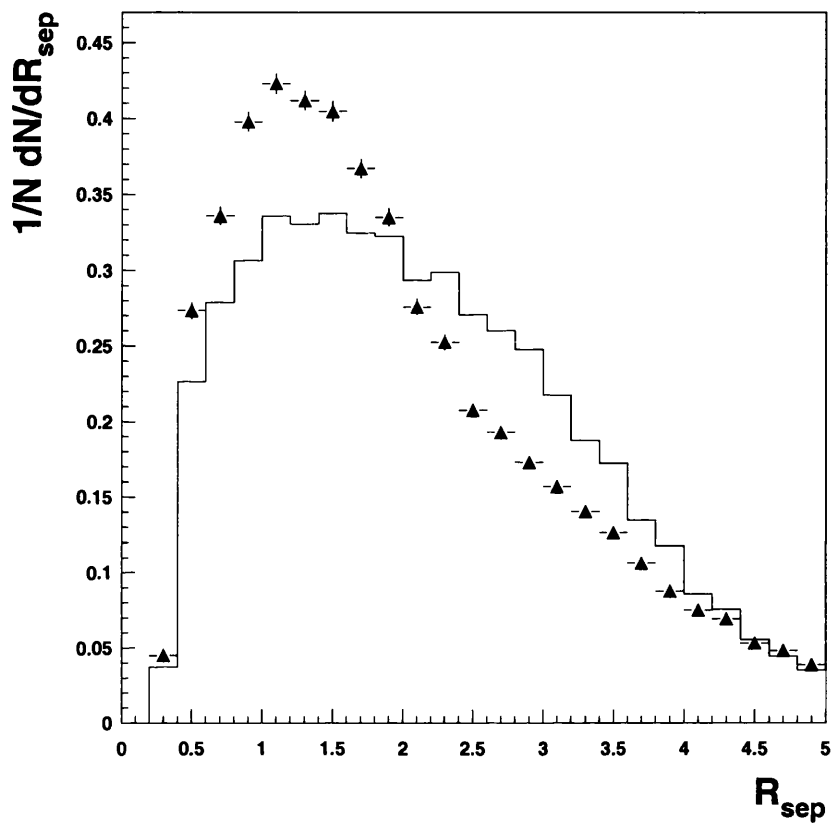


Figure 7.8: Angular distance  $R_{sep}$  between  $b$ -jets from Higgs decays (points) and top decays (histogram).

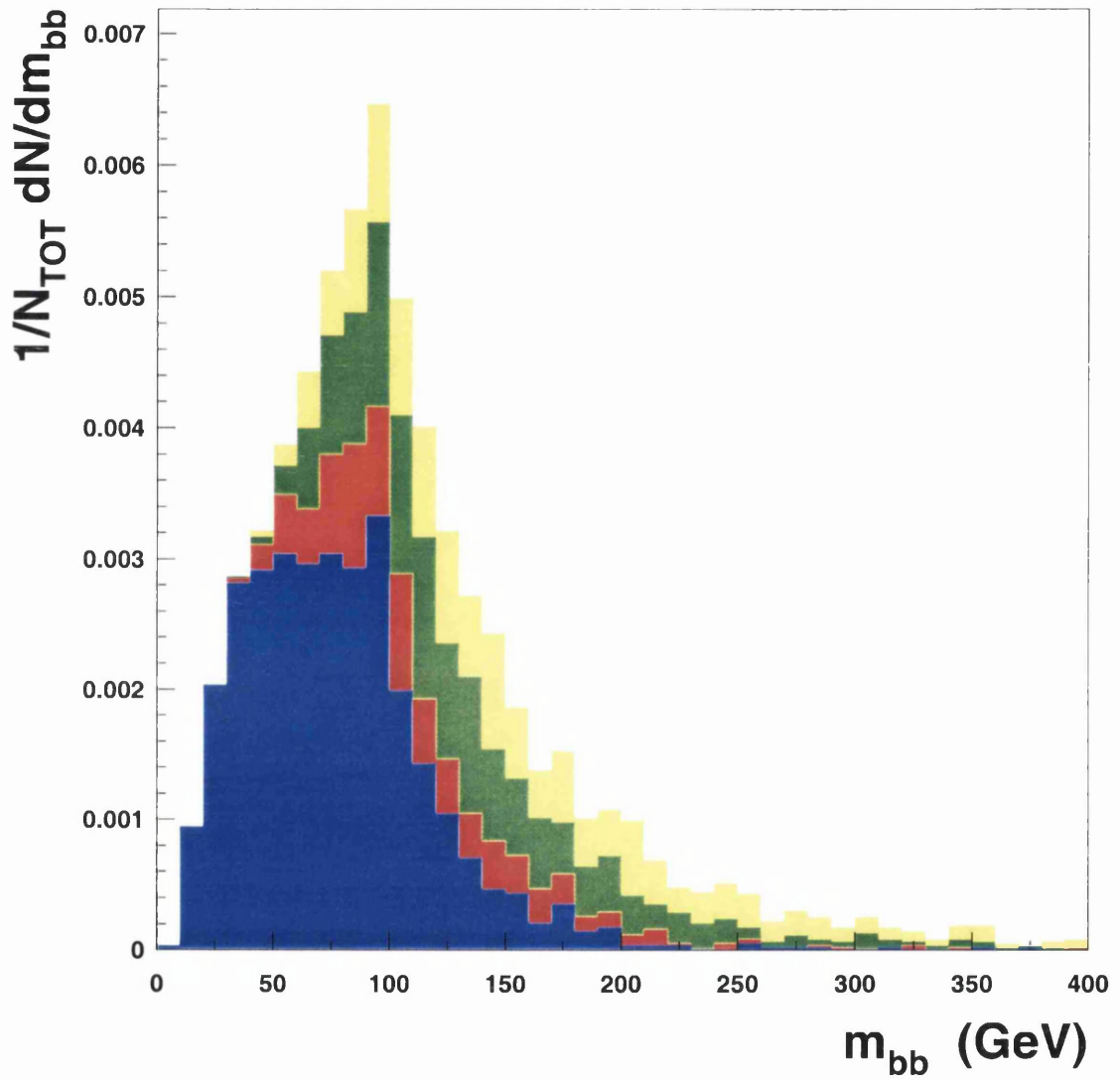


Figure 7.9: Invariant  $m_{bb}$  mass for jets with  $R_{sep}^{max} = 1.75$  (blue), 2.0 (red), 2.5 (green) and 3.0 (yellow).  $N_{TOT}$  is the total number of  $b$ -jet pair combinations.

combinations in the mass plot above 200 GeV are from wrong combinations so the truncated mean and RMS of the  $m_{bb}$  distribution was calculated for  $m_{bb} < 200$  GeV only. Table 7.3 gives the truncated mean and acceptance for the various  $R_{sep}^{max}$  cuts. The acceptance is the fraction of correct  $b$ -jet pair combinations that pass the  $R_{sep}^{max}$  cut. The fraction of correct events is given for all  $m_{bb}$  value and for  $m_{bb}$  within  $\pm 30$  GeV of the nominal Higgs mass. The fraction of correct  $b$ -jet pair combinations would be 0.167 for events with two  $b$ -jets from Higgs decay and two  $b$ -jets from top decays. For events with no  $R_{sep}^{max}$  the fraction of correct combinations is 0.14. This is due to events with four  $b$ -jets found but where only one of the  $b$ -jets from the Higgs decay is both in the detector acceptance and tagged as a  $b$ -jet. From the table the mean shifts from 75 GeV for  $R_{sep}^{max} = 1.75$  up to 95 GeV for  $R_{sep}^{max} = 3.0$ , with a mean for all combinations of 102 GeV. The cut does boost the fraction of correct  $b$ -jet pairs ( $b_{cor}$ ) in the peak from 0.25 for all combinations to 0.29 for  $R_{sep}^{max} = 1.75$ . However, this small increase in correct  $b$ -jet pair choice comes with a low acceptance of 0.31 for  $R_{sep}^{max} = 1.75$  to the  $b$ -jet pairs from the Higgs. Angular separation is thus a poor method to identify the  $b$ -jet pair from the Higgs.

### Reconstruction

A second method of identifying the origin of a  $b$  is to reconstruct the intermediate  $W$ 's and hence the top quarks. The  $b$ -jets not used to reconstruct the top quarks are then identified as coming from the Higgs.

Full reconstruction is non-trivial, since one of the  $W$  bosons in the event is required to decay leptonically to give the trigger lepton: this leads to missing momentum from the neutrino from the  $W$  decay. For full reconstruction the second  $W$  must decay hadronically because if the second  $W$  decays leptoni-

$R_{sep}^{max}$	Mean	RMS	Acceptance	Correct	Correct $\pm 2\sigma_{H \rightarrow b\bar{b}}$
1.75	75	36	0.31	0.18	0.29
2.00	81	38	0.39	0.18	0.28
2.50	89	41	0.52	0.17	0.27
3.00	94	42	0.65	0.15	0.26
None	102	43	1.00	0.14	0.25

Table 7.3:  $m_{bb}$  invariant mass mean and RMS (in GeV) for different values of  $R_{sep}^{max}$ . The mean and RMS are calculated over the mass range 0 to 200 GeV. The final columns gives the fraction of correction  $b$ -jet combinations in the whole plot and within a mass window of  $\pm 2\sigma_{H \rightarrow b\bar{b}}$  (30 GeV) of the actual Higgs mass.

cally then two neutrinos will contribute to the missing momentum and no  $W$  reconstruction could be performed. Also the decay products of the second  $W$  must be found in the detector, further reducing the number of events to be analysed.

### $W \rightarrow l\nu$ Reconstruction

In order to reconstruct the leptonically decayed  $W$  the momentum of the neutrino from the decay must be calculated. The missing transverse momentum is identified as the neutrino transverse momentum and the longitudinal momentum is recovered by solving the equation for the  $W$  mass

$$m_W^2 = (E^\nu + E^l)^2 - (p_x^\nu + p_x^l)^2 - (p_y^\nu + p_y^l)^2 - (p_z^\nu + p_z^l)^2 \quad (7.1)$$

Two solutions for  $p_z$  are obtained and both were used in the top mass reconstruction. Figure 7.10 shows the difference between the reconstructed neu-

trino and true neutrino momentum. For  $\Delta p_z$  only the reconstructed value for  $p_z$  which was closest to the actual neutrino  $p_z$  is plotted.

### $W \rightarrow jj$ Reconstruction

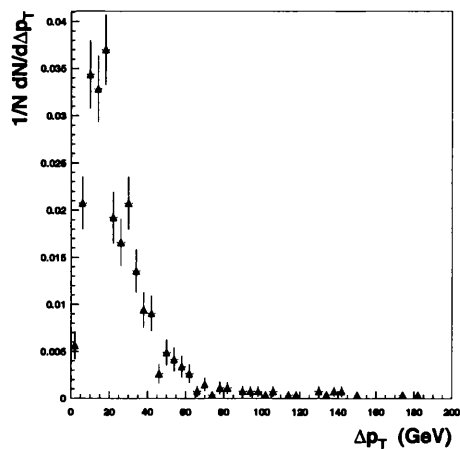
The second  $W$  is required to decay hadronically. First the non- $b$ -jets present in the event were looped through. The pair which gave an invariant mass closest to the  $W$  mass were selected as having come from the second  $W$  decay. Figure 7.11 shows the difference between reconstructed and actual  $W$  momentum and the reconstructed  $W$  mass.

### Top Reconstruction

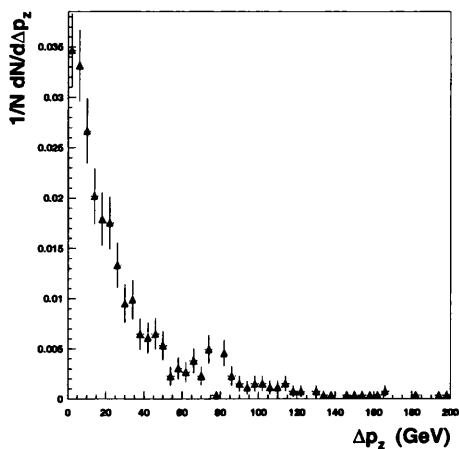
Top reconstruction was performed by looping over  $b$ -jets and calculating the reconstructed top mass using both reconstructed  $W$  bosons. Figure 7.12 shows the reconstructed top masses for all  $W$  and  $b$ -jet combinations for top decays with  $W \rightarrow l\nu$  ( $m_{l\nu b}$ ) and with  $W \rightarrow q\bar{q}'$  ( $m_{jjb}$ ). For the correct  $b$ -jet from the top decays the reconstructed top mass distributions have means of 174 and 182 GeV for  $m_{l\nu b}$  and  $m_{jjb}$  respectively and an RMS of 53 and 56 GeV. For all combinations the distributions are wider, with RMS of 77 and 68 GeV for  $m_{l\nu b}$  and  $m_{jjb}$  respectively.

### Higgs Reconstruction

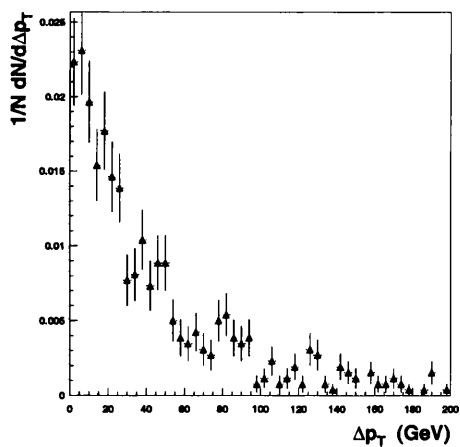
Four methods of selecting the  $b$ -jets to match to the top quark decays were used. In Method I the leptonically decayed  $W$  was reconstructed and then the  $b$ -jets were looped through to find the  $b$ -jet which gave the reconstructed top mass closest to 175 GeV. The hadronically decayed  $W$  was then reconstructed. The remaining three  $b$ -jets were then looped through with the hadronically decayed  $W$  and the  $b$ -jet  $W$  combination which gave the recon-



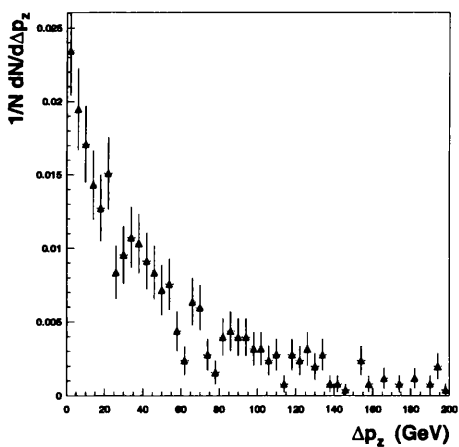
(a)



(b)

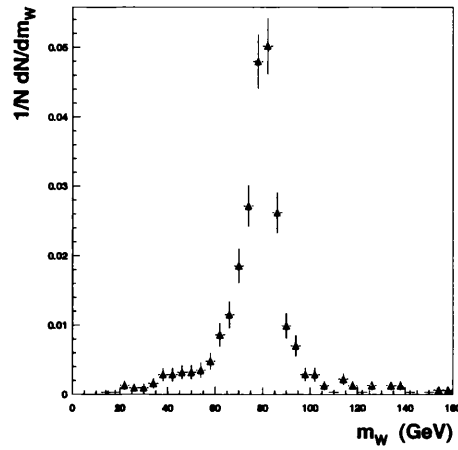


(c)

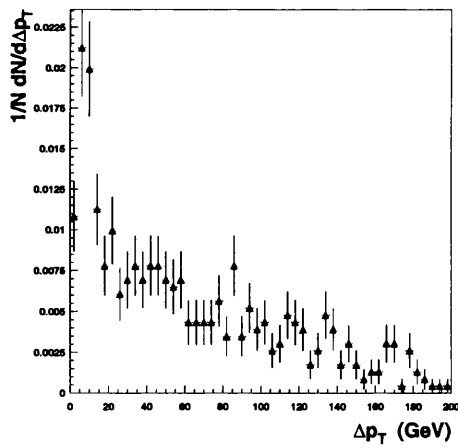


(d)

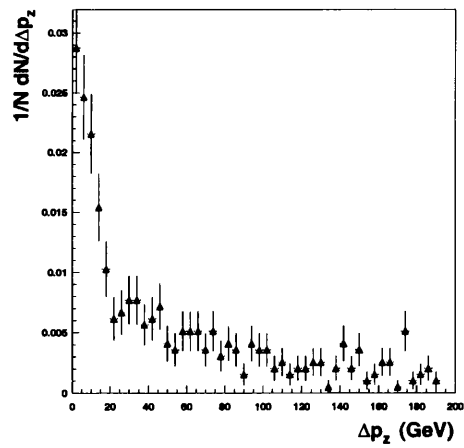
Figure 7.10:  $W \rightarrow l\nu$  reconstruction, difference (in GeV) between missing  $p_T$  and neutrino  $p_T$  (a), difference between calculated neutrino  $p_z$  and actual  $p_z$  (b), and difference between reconstruction and actual  $W$   $p_T$  (c) and  $p_z$  (d).



(a)



(b)



(c)

Figure 7.11:  $W \rightarrow jj$  reconstruction, reconstructed  $W$  mass (a) and difference between reconstructed and actual  $W$   $p_T$  (b) and  $p_z$  (c).

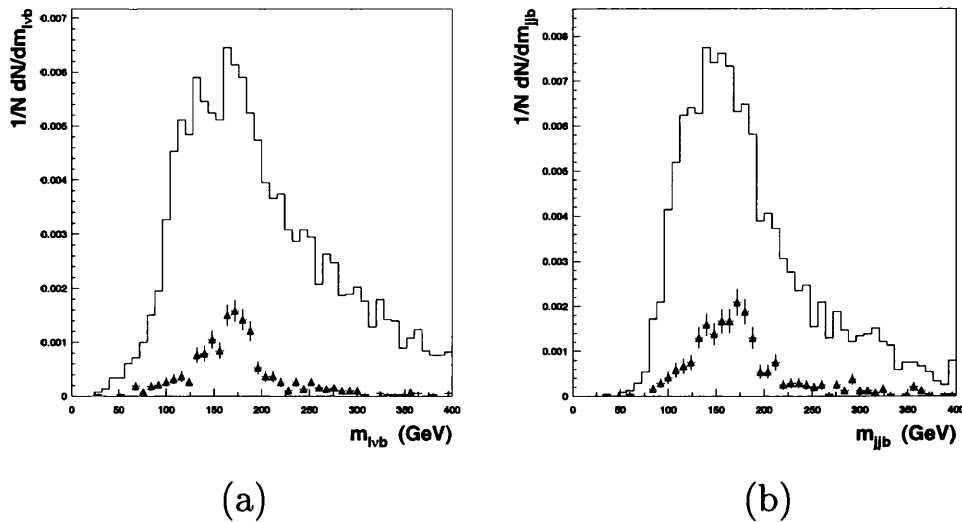


Figure 7.12: Top mass reconstruction for both  $W$  bosons and all  $b$ -jet combinations. (a) top mass from leptonic  $W$  decay, (b) top mass from hadronic  $W$  decay. In the case of the leptonically decaying  $W$  two  $p_z$  values of the  $W$  are obtained and hence two  $m_t$  values, both of which are plotted. The points show the top mass from the correct  $b$ -jet and  $W$  combination only.

constructed top mass closest to 175 GeV was found. The remaining two  $b$ -jets were identified as from the Higgs decay.

For Method II both  $W$  bosons were first reconstructed. The quantity  $\chi^2 = (m_{t1} - M_{TOP})^2 + (m_{t2} - M_{TOP})^2$ , where  $m_{t1}$ ,  $m_{t2}$  are the reconstructed top masses and  $M_{TOP}$  is the input top mass (175 GeV), was calculated for each  $b$ -jet pair combination. The  $b$ -jet pair which minimised  $\chi^2$  was selected as coming from the top decays and the remaining two as coming from the Higgs decay.

In Method III both top quarks were reconstructed as for Method I, however instead of selecting only one combination all  $b$ -jet pair combinations where the reconstructed top masses were both in the range 125 GeV to 200

GeV were selected. For  $b$ -jet pairs which passed the top mass cut regardless of which  $b$ -jet was used to reconstruct which top then only the combination which minimised  $\chi^2 = (m_{t1} - M_{TOP})^2 + (m_{t2} - M_{TOP})^2$  was retained. This selection of multiple  $b$ -jet pairs gave multiple  $b$ -jet pairs as Higgs decay candidates.

For Method IV both  $W$  bosons were first reconstructed. As with Method II the quantity  $\chi^2 = (m_{t1} - M_{TOP})^2 + (m_{t2} - M_{TOP})^2$  was calculated. The  $b$ -jet pairs which gave  $\chi^2 > C_V$  were removed.  $C_V$  was chosen as twice the top mass width (for correct combinations) squared. The combinations passing the cut were selected as coming from top decays and the remaining  $b$ -jets were selected as coming from the Higgs decay. Again if a  $b$ -jet pair passed the cut regardless of which  $b$ -jet was used to reconstruct which top only the combination minimising  $\chi^2$  was retained.

### Performance

Figure 7.13 shows the reconstructed top and Higgs masses for Method I. The other methods give visually similar plots. The effectiveness of the reconstruction methods was characterised by the fraction of correct  $b$ -jet pair combinations in the Higgs mass plot, the number within  $\pm 2\sigma_{H \rightarrow b\bar{b}}$  ( $\pm 30$  GeV) of the Higgs mass and the acceptance to correct pair combinations.

The effectiveness of the various methods to select the correct  $b$ -jet pair from the Higgs decay is summarised in Table 7.4. Methods I and II gave the highest fraction of correct combinations (33% and 34%), however the acceptance to correct combinations is less than 20% for both methods. Methods III and IV gave higher acceptances, with Method IV giving the highest acceptance of 66%.

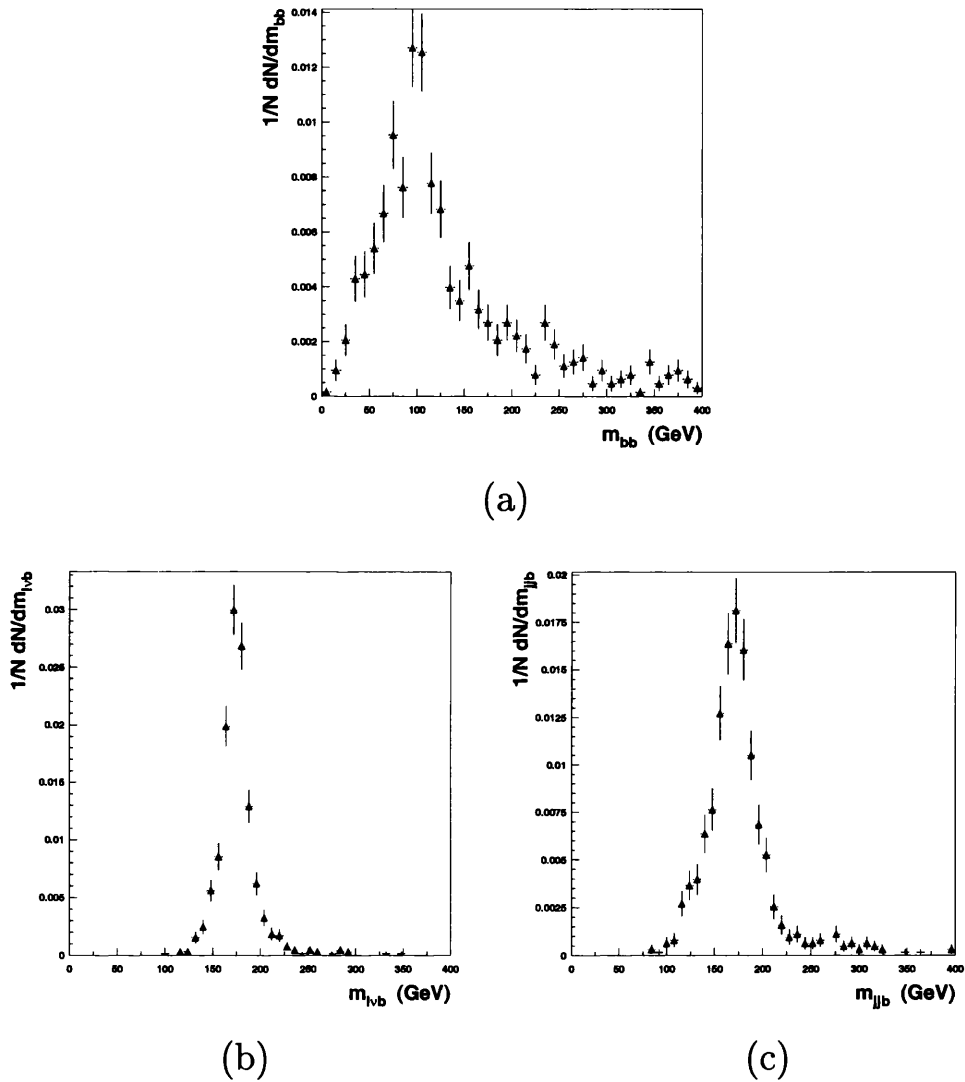


Figure 7.13: Reconstructed masses using Method I, (a) Higgs mass, (b) top mass from leptonically decayed  $W$  and (c) top mass from hadronically decayed  $W$ .

Method	$m_{t1}$	$m_{t2}$	$m_H$	Acceptance	Correct	Correct $\pm 2\sigma_{H \rightarrow b\bar{b}}$
I	173	169	98	0.18	0.18	0.33
II	173	170	100	0.19	0.19	0.34
III	162	162	102	0.37	0.16	0.27
IV	171	167	102	0.66	0.13	0.24

Table 7.4: Performance of the four top quark based reconstruction methods.

### 7.3.4 Signal Summary

The  $t\bar{t}H$  process ignoring any backgrounds is a challenging study in itself. The  $b$ -jets from the top and Higgs decays have similar jet properties and are difficult to differentiate. Reconstructing the  $W$  bosons from the top decays and then the tops themselves gave the best identification of  $b$ -jet origin. Within  $\pm 2\sigma_{H \rightarrow b\bar{b}}$  ( $\pm 30$  GeV) one third of all  $b$ -jet pair combinations in the invariant  $bb$  mass plot were actually from the Higgs decay.

## 7.4 Background

The  $t\bar{t}H$  signal in the detector is an isolated lepton, to provide a trigger, four tagged  $b$ -jets and, for top decay reconstruction, two or more non  $b$ -jets. Any event which has a single isolated lepton is a potential source of background. All the background processes to be described contain at least one  $W$  which is required to decay leptonically to give the trigger lepton.

The background processes for the  $t\bar{t}H$  channel are  $t\bar{t} + \text{jets}$ ,  $t\bar{t}Z$ , single  $W$  production+ jets,  $W$  pair production + jets and  $WZ$  production + jets. The leading order cross-sections for the signal and background processes are shown in Table 7.5 as obtained with PYTHIA 5.7 and the CTEQ2 parton

Process	Cross-section [pb]	Events
$t\bar{t}H$		
$m_H = 80 \text{ GeV}$	1.9	$5.8 \cdot 10^4$
$m_H = 100 \text{ GeV}$	1.0	$3.0 \cdot 10^4$
$m_H = 120 \text{ GeV}$	0.51	$1.5 \cdot 10^4$
$t\bar{t}Z$	$7.1 \cdot 10^{-2}$	$2.1 \cdot 10^3$
$t\bar{t}$	$5.9 \cdot 10^2$	$1.8 \cdot 10^7$
$Wj$	$3.0 \cdot 10^5$	$9.1 \cdot 10^9$
$WZ, WW$	97	$2.9 \cdot 10^6$

Table 7.5: Signal and background production cross-sections and number of events expect for three years' low luminosity running ( $\mathcal{L} = 3 \cdot 10^4 \text{ pb}^{-1}$ ).

distributions. The leading order cross-section values will be used in the following to evaluate strategies for background reduction and then the next to leading order cross-section will be used with the final choice of cuts to obtain the signal significance.

The generation of the background depends on the initial and final state radiation and hadronisation simulation to generate the required number of jets to fake a signal event. No  $b$  partons are generated as part of the hadronisation as heavy quark production during hadronisation is heavily suppressed [63]. The backgrounds can be divided into the irreducible background,  $t\bar{t}Z$ , the semi-irreducible backgrounds  $t\bar{t}b\bar{b}$  and  $Wbbbb$  and the reducible backgrounds  $t\bar{t}jj$ ,  $Wjjjj$ ,  $WZjj$  and  $WWjj$ .

### 7.4.1 Irreducible Backgrounds

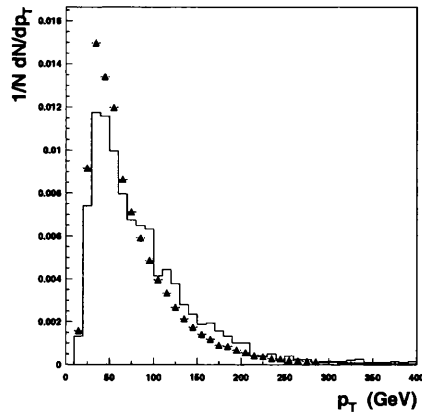
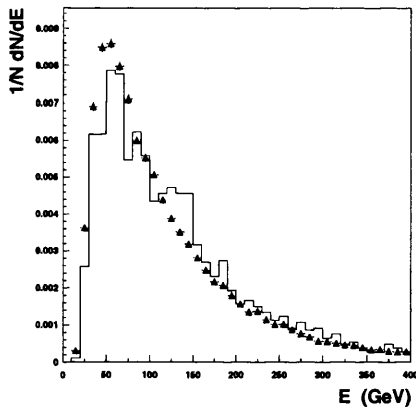
The irreducible background for the  $t\bar{t}H$  signal is  $t\bar{t}Z$ . This background mimics the signal exactly when the  $Z$  boson decays to a  $b\bar{b}$  pair. Figure 7.14 shows a comparison between the  $b$ -jets from the  $Z$  decay in  $t\bar{t}Z$  and the Higgs decay in  $t\bar{t}H$ . Clearly the  $b$ -jets from the  $Z$  cannot be separated from the  $b$ -jets from the Higgs. Fortunately the leading order  $t\bar{t}Z$  production cross-section is only 0.07 pb and including the branching ratio for  $Z \rightarrow b\bar{b}$  reduces this to 0.01 pb. The total number of events from  $t\bar{t}Z$  is only 2,000 in three years' low luminosity running, an order of magnitude less than for  $t\bar{t}H$ .

### 7.4.2 Semi-irreducible Backgrounds

The semi-irreducible backgrounds are so called as there is some reduction possible in the backgrounds but not of the same magnitude as for the reducible backgrounds. These backgrounds all generate a single lepton and four  $b$ -quarks to mimic the signal.

$t\bar{t} + \text{jets}$  is classified as a semi-irreducible background when the jets produced are from  $b$ -quarks. In these events two  $b$ -jets are produced from the top decays and the other  $b$ -jets are generated in initial and final state radiation. The comparison between  $b$ -jets produced in the Higgs decay and  $b$ -jets produced by initial and final state radiation is shown in Figure 7.15. The  $b$ -jets produced by initial and final state radiation tend to be lower in  $p_T$  and produced at higher  $|\eta|$  than  $b$ -jets from Higgs decay.

The  $W + \text{jets}$  background also contributes to the semi-irreducible background when four additional  $b$ -jets are produced in the initial and final state radiation. Figure 7.15 shows the comparison between  $b$ -jets produced by initial and final state radiation from  $W + \text{jets}$  and  $b$ -jets produced in the Higgs

(a) Jet  $p_T$ 

(b) Jet Energy

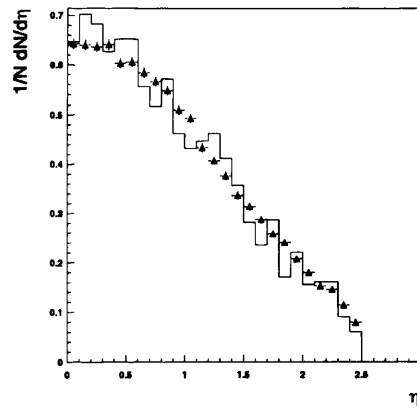
(c) Jet  $|\eta|$ 

Figure 7.14: Jet characteristics for  $b$ -jets from  $Z$  decays in  $t\bar{t}Z$  (histogram) and  $b$ -jets from Higgs decay in  $t\bar{t}H$  (points).

decay.  $b$ -jets from  $W$  decay are not included as the  $W$  is required to decay leptonically to give a trigger. The production cross-section for  $W + \text{jets}$  is very high at  $3 \cdot 10^5$  pb, although only a small fraction of these events give a trigger and four  $b$ -jets.

Both of these backgrounds have some potential to be reduced. The production of  $b$ -quarks during initial and final state radiation is approximately uniform in  $|\eta|$  while  $b$ -quarks from Higgs decays are mainly produced at low  $|\eta|$ .

### 7.4.3 Reducible Backgrounds

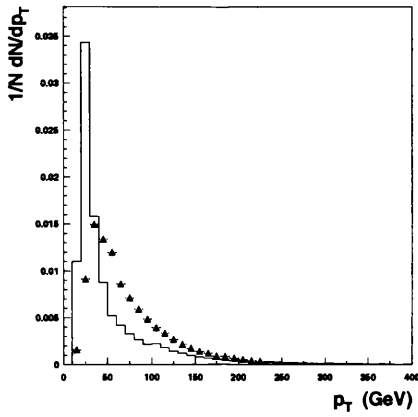
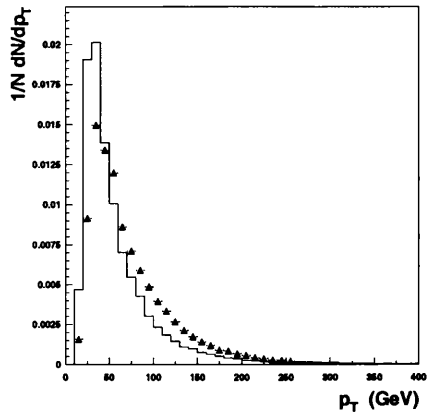
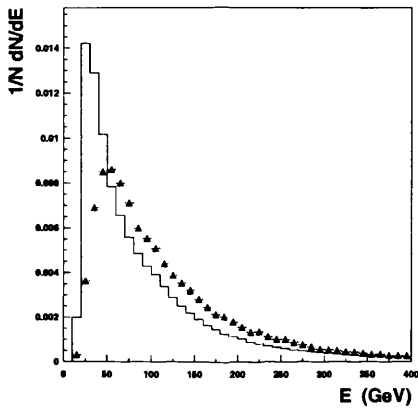
As with the other backgrounds the reducible backgrounds contain a  $W$  which is required to decay leptonically to provide a trigger. These backgrounds are  $t\bar{t} + \text{jets}$ ,  $W + \text{jets}$ ,  $WW + \text{jets}$  and  $WZ + \text{jets}$ , where at least one of the jets is a non  $b$ -jet.

The additional jets in these background processes are produced from initial and final state radiation and hadronisation. The majority of jets originate from light quarks so these backgrounds can be suppressed by a factor  $(R_u)^2 \sim 10^{-4}$  for  $t\bar{t} + \text{jets}$  and  $(R_u)^4 \sim 10^{-8}$  otherwise. This factor is large if the  $b$ -tagging performed has a low mis-tagging of light quark jets as  $b$ -jets.

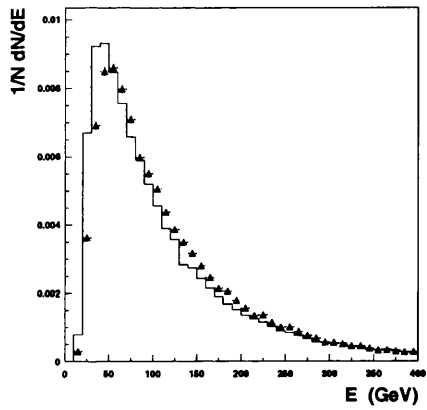
The jet characteristics for the  $WW$  and  $WZ$  backgrounds are shown in Figure 7.16. The jets from the  $WW$  and  $WZ + \text{jets}$  background have a lower average  $p_T$  and a slower drop off in  $|\eta|$  than  $b$ -jets from Higgs decay.

Figure 7.17 shows the non  $b$ -jet  $p_T$ ,  $|\eta|$  and energy from  $W + \text{jets}$  compared to the  $b$ -jets from the Higgs in  $t\bar{t}H$ . The non  $b$ -jets from the  $W + \text{jets}$  background have a low average  $p_T$  and a more uniform distribution in  $|\eta|$ .

The light quark jets in the  $t\bar{t} + \text{jets}$  background are shown in Figure 7.17. The differences between the light quark jets from  $t\bar{t} + \text{jets}$  and the  $b$ -jets

(a) Jet  $p_T$ (d) Jet  $p_T$ 

(b) Jet Energy



(e) Jet Energy

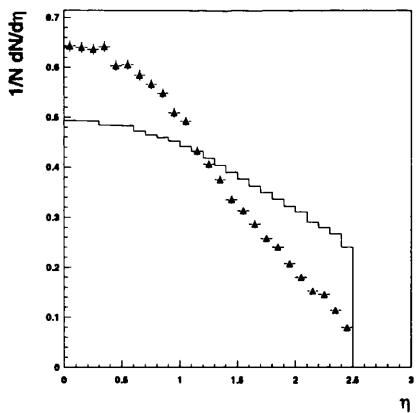
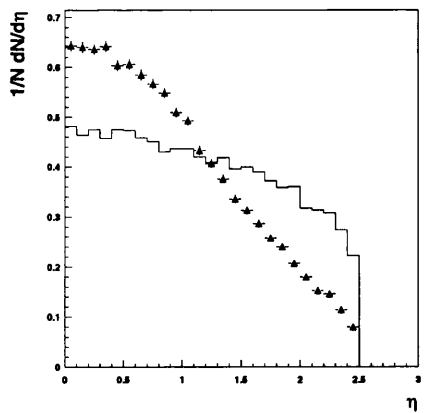
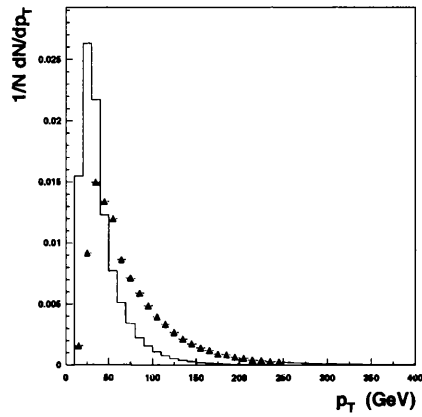
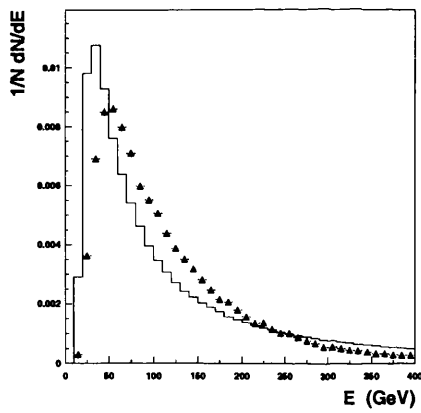
(c) Jet  $|\eta|$ (f) Jet  $|\eta|$ 

Figure 7.15: Jet characteristics for  $b$ -jets from initial and final state radiation in (a)-(c)  $t\bar{t}$  + jets (histogram) and (d)-(f)  $W$  + jets (histogram), the points in all plots are  $b$ -jets from Higgs decay in  $t\bar{t}H$ .

(a) Jet  $p_T$ 

(b) Jet Energy

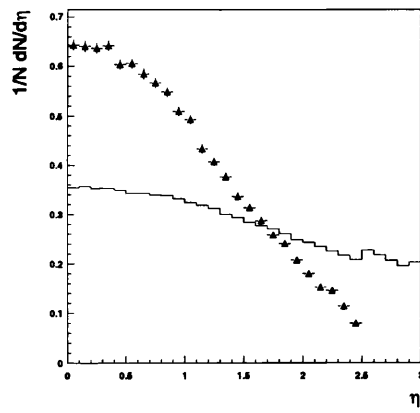
(c) Jet  $\eta$ 

Figure 7.16: Jet characteristics for non  $b$ -jets in  $WW$  and  $WZ + \text{jets}$  (histogram) and  $b$ -jets from Higgs decay in  $t\bar{t}H$  (points).

from Higgs decay are less pronounced than for the other backgrounds. The  $p_T$  of the light quark jet background is only slightly lower on average than  $b$ -jets from Higgs decay and the background jet production rate decreases with increasing  $|\eta|$  although at a lesser rate than for  $b$ -jets from Higgs decay.

## 7.5 Background Reduction

Background reduction was achieved primarily through  $b$ -tagging, removing jets originating from light quarks. The semi-irreducible background was reduced through the use of cuts on the  $b$ -jet  $p_T$  and  $|\eta|$ . The following section describes these cuts.

### 7.5.1 Tagging Efficiency

The reduction of the reducible background depends on the rate of mis-tagging light quark jets as  $b$ -jets. Three sets of  $b$ -tagging efficiency ( $e_b$ ), light quark and  $c$  quark rejection factors ( $R_u$  and  $R_c$ ) were used to study this channel.

These were:

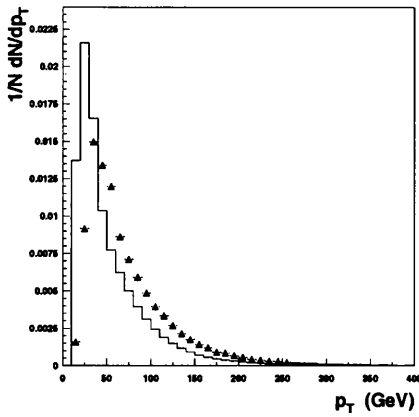
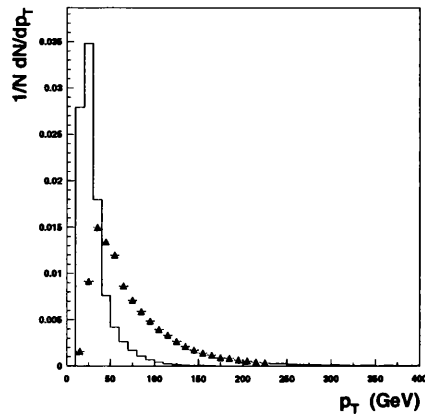
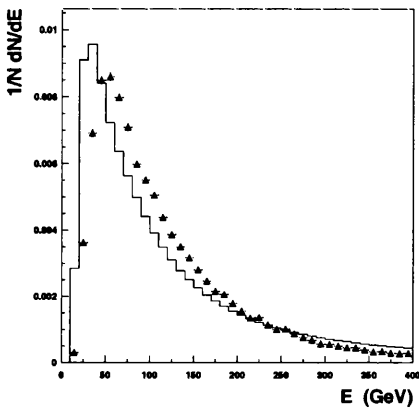
A  $e_b = 0.6$ ,  $R_u = 93$  and  $R_c = 6.7$ ;

B  $e_b = 0.5$ ,  $R_u = 231$  and  $R_c = 10.7$ ;

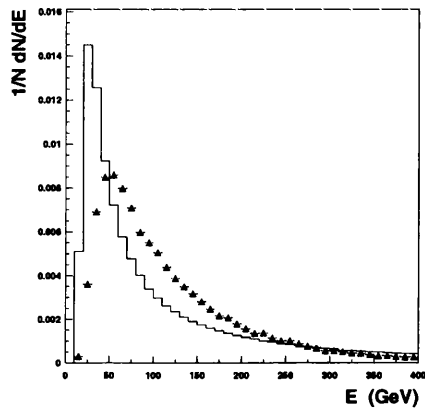
C  $e_b = 0.53$ ,  $R_u = 91$  and  $R_c = 6.7$ .

Sets A and B represent the best currently expected performance for the detector for  $e_b = 0.6$  and  $e_b = 0.5$ . Set C is an earlier, more pessimistic, expectation of rejection factors to give an idea of performance if the best  $b$ -tagging is not achieved.

Table 7.6 gives the expected number of events for three years' low luminosity running for each of the three  $b$ -tagging performance values (for  $m_H = 100$

(a) Jet  $p_T$ (d) Jet  $p_T$ 

(b) Jet Energy



(e) Jet Energy

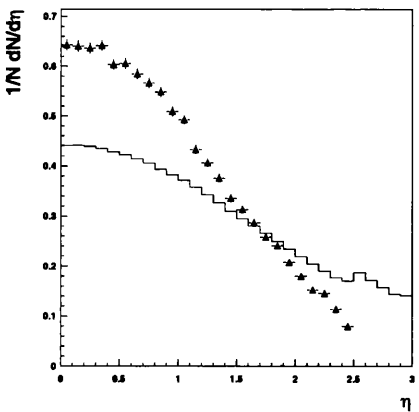
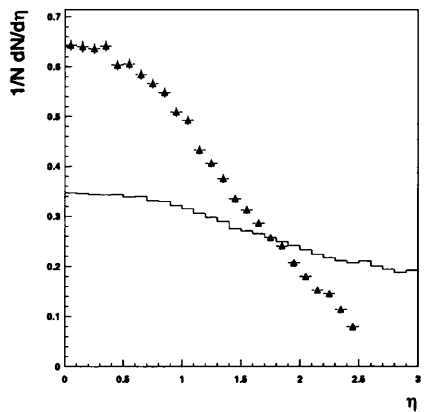
(c) Jet  $|\eta|$ (f) Jet  $|\eta|$ 

Figure 7.17: Jet characteristics for non  $b$ -jets from initial and final state radiation in (a)-(c)  $t\bar{t}$  + jets (histogram) and (d)-(f)  $W$  + jets (histogram), the points in all plots are  $b$ -jets from Higgs decay in  $t\bar{t}H$ .

Process	1 $l$ , 4+ jets	Set A	Set B	Set C
$t\bar{t}H$	9100	490	220	360
$t\bar{t}Z$	620	48	20	27
$t\bar{t}$	$4.4 \cdot 10^6$	6900	2100	8000
$WW, WZW$	$1.3 \cdot 10^5$	3	2	4
$W + \text{jet}$	$3.4 \cdot 10^7$	830	250	1140
Total Background	$3.4 \cdot 10^7$	7800	2400	9200
S/B	-	0.063	0.094	0.040
$S/\sqrt{B}$	-	5.6	4.6	3.8

Table 7.6: Expected number of signal and background events and signal significance for three years' low luminosity running for  $m_H = 100$  GeV and for three  $b$ -tagging performance values described in the text.

GeV).  $S/B$  is the signal divided by the total background and  $S/\sqrt{B}$  is the signal significance, the signal divided by the square root of the total background. The largest background, by an order of magnitude, comes from  $t\bar{t} + \text{jets}$ . The other significant background comes from  $W + \text{jets}$ . The total background is over an order of magnitude larger than the signal. The  $W + \text{light quark jets}$  background was reduced by a factor of  $10^4$ . The best signal significance was from  $b$ -tagging values set A with a significance of 5.6. Even after  $b$ -tagging the total background is 25 to 10 times larger than the signal (depending on  $b$ -tagging performance).

### 7.5.2 $p_T$ Cut

The  $b$ -jets produced by initial and final state radiation in the  $t\bar{t} + \text{jets}$  background have a lower  $p_T$  distribution than  $b$ -jets from the Higgs decay in the

Process	No Cut	$p_T > 20$	$p_T > 30$	$p_T > 40$	$p_T > 50$
$t\bar{t}H$	490	460	290	136	63
$t\bar{t}Z$	48	44	28	11	5
$t\bar{t} + \text{jets}$	6900	5700	2500	1000	510
$WW, WZ + \text{jets}$	3	0	0	0	0
$W + \text{jets}$	830	610	230	0	0
Total Background	7800	6300	2800	1100	520
S/B	0.063	0.073	0.105	0.123	0.120
$S/\sqrt{B}$	5.6	5.8	5.6	4.1	2.8

Table 7.7: Expected number of signal and background events and signal significance as a function of minimum jet  $p_T$  (in GeV) for three years' low luminosity running for  $m_H = 100$  GeV, using  $b$ -tagging set A.

signal process. There is therefore a potential cut on the  $b$ -jet  $p_T$  to improve the significance. The ATLFAST reconstruction already includes a cut on the jet  $p_T$  since only jets with a minimum  $p_T$  of 15 GeV, before the jet  $p_T$  is recalibrated, are reconstructed. The effect of cutting on the jet  $p_T$  after the recalibration is shown in Table 7.7. Increasing the  $p_T$  cut up to 40 GeV increases the signal/background but the significance is only increased over no cut for a  $p_T > 20$  GeV.

### 7.5.3 $\eta$ Cut

The fraction of  $b$ -jets at high  $|\eta|$  from  $b$ -jets produced by initial and final state radiation in the  $t\bar{t} + \text{jets}$  background is higher than for  $b$ -jets from the signal process Higgs decay. A cut on the  $|\eta|$  of  $b$ -jets could therefore lead to an increase in the signal significance. Table 7.8 gives the signal significance for

Process	No Cut	$ \eta  < 2.25$	$ \eta  < 2.00$	$ \eta  < 1.75$	$ \eta  < 1.50$	$ \eta  < 1.25$
$t\bar{t}H$	490	450	390	300	230	150
$t\bar{t}Z$	48	42	34	29	19	13
$t\bar{t} + \text{jets}$	6900	5800	4600	3500	2300	2300
$WW, WZ + \text{jets}$	3	2	1	1	1	0
$W + \text{jets}$	830	690	520	340	180	36
Total Background	7800	6600	5200	3900	2500	1500
S/B	0.063	0.068	0.074	0.079	0.090	0.103
$S/\sqrt{B}$	5.6	5.5	5.4	4.9	4.6	4.0

Table 7.8: Expected number of signal and background events and signal significance as a function of maximum jet  $|\eta|$  for three years low luminosity running for  $m_H = 100$  GeV, using  $b$ -tagging set A.

a range of cuts on the jet  $|\eta|$ . As with the  $p_T$  cut as more jets and events are removed from the analysis the ratio of signal to background does improve, however the jet  $|\eta|$  cut does not improve the signal significance.

#### 7.5.4 Background Reduction Summary

$b$ -tagging set A gives the highest signal significance, removing the vast majority of the light quark background. The lowest  $p_T$  cut reduced the background by approximately 20% without reducing the signal. No  $|\eta|$  cuts improve the signal significance. Table 7.9 gives the signal significance for the best  $p_T$  cut combined with  $b$ -tagging values sets A and C for  $m_H = 80, 100$  and  $120$  GeV.  $b$ -tagging set A, jet  $p_T > 20$  GeV and no  $|\eta|$  cut were selected as the best tagging and cuts optimisation and used exclusively for the remaining analysis except for comparisons to the more pessimistic  $b$ -tagging values in

Process	Set A	Set C
$t\bar{t}H$	460	370
$t\bar{t}Z$	44	28
$t\bar{t}$	5700	6500
$WW, WZ + \text{jets}$	0	1
$W + \text{jets}$	610	800
Total Background	6300	7400
S/B	0.073	0.050
$S/\sqrt{B}$	5.8	4.3

Table 7.9: Expected number of signal and background events and signal significance for jet  $p_T > 20$  GeV, jet  $\eta < 2.25$ , for  $b$ -tagging values sets A and C, for three years low luminosity running for  $m_H = 100$  GeV.

set C.

## 7.6 Event Reconstruction

The event reconstruction described in section 7.3.3 was applied to the background. This has the potential to reduce the background as it requires two non  $b$ -jets in the events in addition to the four tagged  $b$ -jets. To estimate residual background, only events within two sigma of the Higgs mass were counted, with the processes of assigning  $b$ -jets to top decays and Higgs decays unchanged. Table 7.10 gives the signal and background rates for these modified reconstruction methods. Methods III and IV require special attention as they can generate multiple Higgs candidate masses per event. To calculate the number of signal and background events each event was counted if any one of the  $b$ -jet pairs selected as coming from the Higgs gave an invariant

Process	1 $l$ , 4 $b$ -jets	Reconstruction Method			
	2 non $b$ -jets	I	II	III	IV
$t\bar{t}H$	465	146	147	177	282
$t\bar{t}Z$	43	15	16	13	27
$t\bar{t} + \text{jets}$	5650	1245	1232	1565	2868
$WW, WZ + \text{jets}$	3	0	0	0	0
$W + \text{jets}$	728	127	127	109	218
Total Background	6424	1387	1375	1687	3113
S/B	0.072	0.105	0.107	0.105	0.091
$S/\sqrt{B}$	5.8	3.9	4.0	4.3	5.1

Table 7.10: The significances for events requiring 1 lepton, 4  $b$ -jets and 2 non  $b$ -jets the three (first column) and the four reconstruction methods. Only mass combination with  $\pm 2\sigma$  of the Higgs mass width are counted.

mass in the Higgs mass window.

Simply requiring the extra two non  $b$ -jets improves signal to background ratio but not the significance. Reconstruction Method II gave the highest signal to background ratio of 0.107. Method IV gave the best significance out of the reconstruction methods but still gave no improvement on the significance when requiring only one lepton and four tagged  $b$ -jets.

## 7.7 Leading Order Performance

The leading order performance was evaluated without any top reconstruction, using  $b$ -tagging values Set A. The signal and background in a mass window -30 to +20 GeV of the Higgs was counted and the significance calculated. The -30, +20 mass window was chosen as an improvement over a mass window

of  $2\sigma_{H\rightarrow b\bar{b}} \simeq \pm 30$  since the Higgs invariant mass peak is antisymmetrical with a narrower half width on the high mass side. This gave a reduction in background for little loss of signal.

The cross-section for the  $t\bar{t}H$  process falls with increasing Higgs mass while the background remains constant to within 10% over  $80 < m_H < 120$  GeV. The significance therefore falls with increasing Higgs mass. Figure 7.18 shows the invariant  $m_{bb}$  jet mass plot for all combinations from events with four  $b$ -jets. The background peaks at approximately 80 GeV, visually obscuring the signal in any invariant  $m_{bb}$  plot. Table 7.11 gives the signal significance for  $m_H = 80, 100$  and 120 GeV. The signal can be seen here as an excess of events over an expected background rate.

The leading order performance can be compared to the results described in [64] although there are differences in the details of the analyses. The results for overall signal significance obtained there are comparable with the results described here. However the background rates differ, with approximately three times more background here than in [64]. The combination of differences in analysis methods and background rates result in roughly equal signal significances from both analyses.

Determining the mass of the Higgs from a plot of  $m_{bb}$  has an inherent difficulty, in that many of the  $b$ - $b$  jet invariant mass combinations do not come from the Higgs decay. The reconstruction method which gave the best fraction of correct  $b$ -jet pair combinations was Method I, with a fraction of 0.33 correct within  $2\sigma_{m\rightarrow b\bar{b}}$ . The background contributes another 1387 events in the mass window. This gives 48 out of 1485 correct  $b$ -jet combinations in the mass window. Deriving a mass from this peak is clearly problematic.

The Higgs mass could be determined by running a mass window across the invariant jet mass plot. The window used here was -30, +20 GeV of the

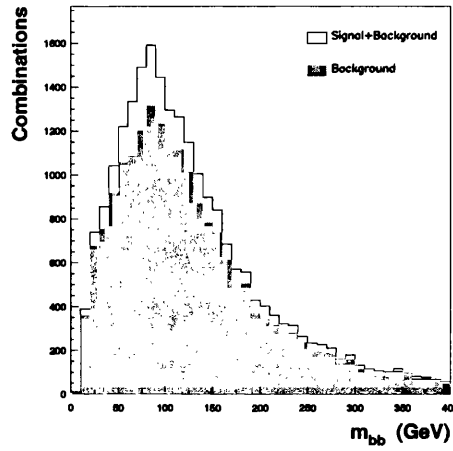
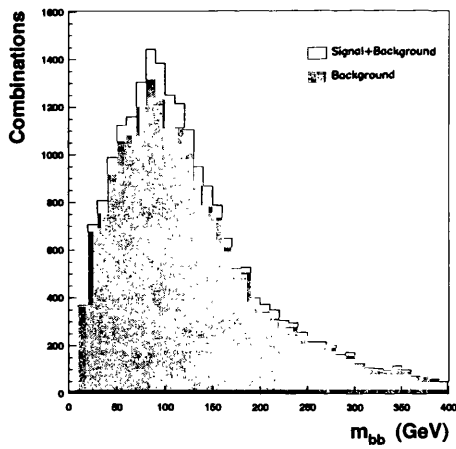
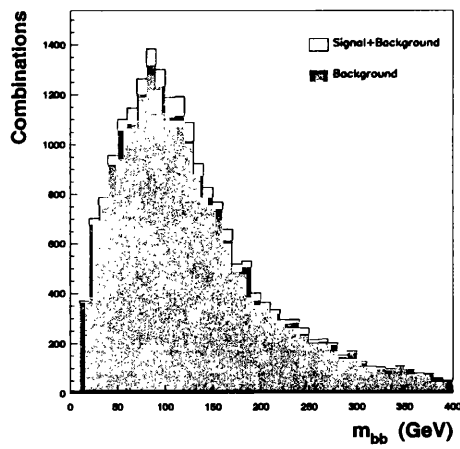
(a)  $m_H = 80$  GeV(a)  $m_H = 100$  GeV(c)  $m_H = 120$  GeV

Figure 7.18: Invariant  $m_{b\bar{b}}$  mass for all combinations from events with four  $b$ -jets, for (a)  $m_H = 80$ , (b)  $m_H = 100$ , (c)  $m_H = 120$  GeV.

	$m_H = 80$ GeV	$m_H = 100$ GeV	$m_H = 120$ GeV
$t\bar{t}H$	822	465	270
Total Background	6183	6424	6163
S/B	0.133	0.072	0.044
$S/\sqrt{B}$	10.5	5.8	3.4

Table 7.11: Total signal and background, signal to background ratio and signal significance for leading order cross-sections for  $m_H = 80, 100$  and  $120$  GeV, using cuts and  $b$ -tagging defined in text.

tested Higgs mass. The number of signal and background events in the mass window was counted and the significance calculated. Figure 7.19 shows a plot of significance versus the central mass values of the window for a generated Higgs mass of  $100$  GeV. The significance peaks at the generated Higgs mass value, however the enhancement is relatively small.

## 7.8 Systematic Errors

A complete determination of the systematic errors would require full reconstruction. However ATLFAST enables the main systematic uncertainties to be estimated. Two systematic errors are evaluated here, uncertainties in the jet scale energy and uncertainties in the  $b$ -tagging performance values.

### Jet Scale

Hadronic jets found in an event have in general less energy than the parton which produced the jet. The 4-vectors of the jets are therefore rescaled such that the jet and parton 4-vectors are on average the same. The scaling factor used is dependent on the jet  $p_T$  and the type of jet,  $b$ -jets requiring a different

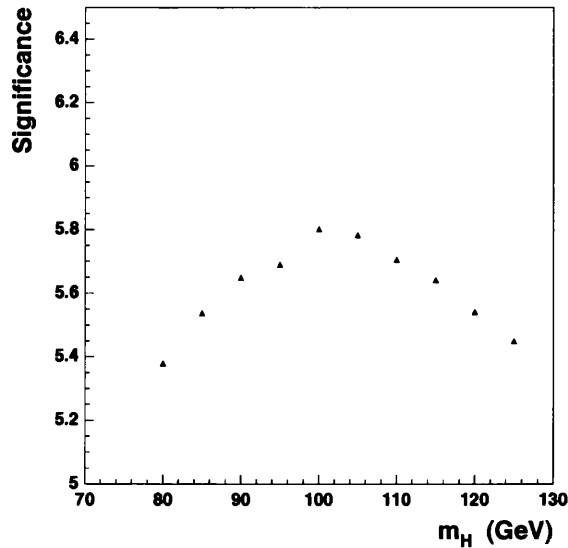


Figure 7.19: Plot of significance of a mass window  $-30, +20$  of the plotted mass, for  $m_H = 100$  GeV. Note the suppressed zero on the  $y$  axis: the absolute change in significance is relatively small.

scaling factor from non  $b$ -jets. The accuracy of this rescaling procedure is expected to be controlled at the 1% level.

The effect on a  $t\bar{t}H$  Higgs search of the accuracy on the jet scaling was investigated by introducing an offset to all the jet energies after rescaling. The change in the number of background events in a mass window of 90 to 150 GeV, corresponding to the mass window for a 120 GeV Higgs, was then determined. The 120 GeV Higgs was used as this has the lowest cross-section in the mass range and will hence be most affected by background uncertainties. Table 7.12 gives the background changes. If the jet rescaling is accurate to within the expected 1% then the background changes by only 23 events, which is 8% of the 120 GeV Higgs signal. For a background of 6150 events the statistical variation is  $\pm 78$  events. The uncertainty in the

	-2.00%	-1.75%	-1.50%	-1.25%	-1.00%	-0.75%
Total Background	6163	6160	6152	6149	6150	6186
Change	0	-3	-11	-14	-13	23
Change/Signal	0.000	-0.011	-0.040	-0.051	-0.048	0.084
	-0.50%	-0.25%	$\pm 0$	+0.25%	+0.50%	+0.75%
Total Background	6176	6169	6163	6168	6172	6181
Change	13	6	0	5	9	18
Change/Signal	0.048	0.022	0	0.018	0.033	0.066
	+1.00%	+1.25%	+1.50%	+1.75%	+2.00%	
Total Background	6177	6178	6175	6181	6174	
Change	14	15	12	18	11	
Change/Signal	0.051	0.055	0.044	0.066	0.040	

Table 7.12: Change in background events in the mass window 90 to 150 GeV for jet energies mis calibrated from  $-2\%$  to  $+2\%$ .

jet scale is not problematic for Higgs discovery if the 1% jet scale uncertainty is achieved.

### ***b* tagging uncertainties**

The requirements on the knowledge of the *b*-tagging performance was investigated by varying  $e_b$  around the 0.60 value used for *b*-tagging Set A. Table 7.13 gives the changes in signal rates for small changes in  $e_b$ , keeping  $R_u$  and  $R_c$  constant. As the signal event rate goes as  $e_b^4$  even small changes in  $e_b$  can effect the signal rate. For  $e_b = 0.60$  the expected number of events is  $465 \pm 22(\text{stat.})$ . A change in  $e_b$  of 0.01 is sufficient to change the number of signal events over three years' low luminosity running by the statistical

	$e_b = 0.60$	$e_b = 0.58$	$e_b = 0.59$	$e_b = 0.61$	$e_b = 0.62$
Signal	465	394	414	483	506
Difference	0	-71	-51	18	41
$S/\sqrt{B}$	5.8	4.9	5.2	6.0	6.3

Table 7.13: Change in signal rate and significance for small changes in  $e_b$  ( $R_u = 93$ ,  $R_c = 6.7$ ), the difference row is the difference in events between  $e_b = 0.60$  and the given  $e_b$ .

uncertainty.

## 7.9 NLO cross-section

The NLO cross section calculation for  $t\bar{t}$  production is 833 pb [65], an increase of 40% on the leading order cross-section. An exact calculation for the  $t\bar{t}H$  signal is not available but using the approximation  $m_H \ll m_t$  the QCD radiative corrections can be calculated [66]. The NLO correction is dependent on  $m_H$  and varies depending on the structure function used from +20% to +30% over the mass range  $80 < m_H < 120$  GeV. A uniform increase of +30% over the leading order cross-section, across the mass range, is used here.

Table 7.14 gives the signal significance using the NLO process cross-sections for  $t\bar{t}$  and  $t\bar{t}H$ . Although the background has increased by a larger percentage than the signal, the signal significance has improved overall. The significance versus  $m_H$  is shown graphically in Figure 7.20, for  $b$ -tagging set A. Without any NLO cross section corrections the signal significance is  $5\sigma$  up to  $m_H = 100$  GeV, for three years' low luminosity data taking. With the NLO corrections the  $5\sigma$  reach for the  $t\bar{t}H$  channel extends out to 110 GeV. The final LEP II run found a possible Higgs signal for  $m_H = 115$  GeV. Using

	$m_H = 80$ GeV	$m_H = 100$ GeV	$m_H = 120$ GeV
$t\bar{t}H$	1068	604	351
Total Background	8347	8684	8355
S/B	0.128	0.070	0.042
$S/\sqrt{B}$	11.7	6.5	3.8

Table 7.14: Signal significance with NLO cross-sections for  $m_H = 80, 100, 120$  GeV, for  $b$ -tagging Set A.

this analysis ATLAS would give a signal significance of  $4\sigma$  after three years' low luminosity running for a Higgs particle with  $m_H = 115$  GeV.

In addition to the NLO cross-section corrections the background could be increased due to enhancement of the inclusive  $b$ -quark cross-section. In results from the Tevatron proton anti-proton collider the inclusive  $b$ -quark production rate measured by the two Tevatron detectors CDF [67] and D0 [68] has been found to be a factor 2.5 higher, on average, than typical Monte Carlo calculations [69]. If the LHC  $b$ -quark production cross-section was similarly increased by 2.5 from values given previously this would result in a drop in signal significance by a factor of  $\sqrt{2.5} \simeq 1.6$ . Further work is required to establish a consistent set of Monte Carlo parameters to obtain results consistent with CDF and D0.

## 7.10 Summary

The channel  $t\bar{t}H$  has been analysed for suitability for a Higgs boson search in the mass range  $80 < m_H < 120$  GeV. The difficulties associated with the multiple  $b$ -jet final state have been described and several techniques evaluated to overcome them. The highest signal significance came from counting

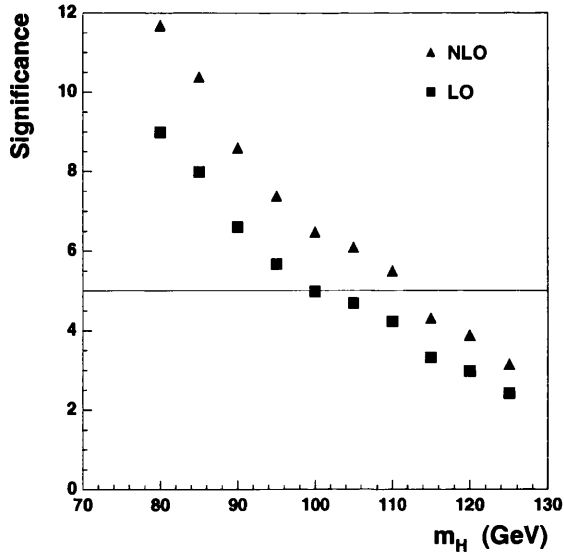


Figure 7.20: Signal significance as a function of  $m_H$  using LO and NLO cross-section values.

all events with one isolated lepton and four tagged  $b$ -jets. The change in significance over a mass window for fixed  $m_H$  was shown, with the highest significance in the mass window corresponding to  $m_H$ . The change in background with uncertainties in jet energy scale and the change in signal with uncertainties in  $b$ -tagging performance was presented. Finally the overall significance for the Higgs boson was given for the NLO process cross-sections. The channel is above a  $5\sigma$  discovery threshold up to  $m_H = 110$  GeV for an integrated luminosity of  $3 \cdot 10^{-4} \text{pb}^{-1}$ . For low luminosity running an integrated luminosity of  $\simeq 4 \cdot 10^{-4}$  (four years' low luminosity running) would be required to achieve a  $5\sigma$  discovery threshold for  $m_H = 115$  GeV.

# Chapter 8

## Summary

The studies presented in this thesis concern the ATLAS ID, which were performed as part of a large effort to characterise and develop the detector design. The study of single track reconstruction was presented. For high transverse momentum ( $p_T = 200$  GeV) muons this gave  $\sigma(1/p_T) = 0.4 \text{ TeV}^{-1}$ ,  $\sigma(d_0) = 10\mu\text{m}$  and  $\sigma(z_0)$  ranged from  $55 < \sigma(z_0) < 150\mu\text{m}$  depending on track rapidity. It was found that the B-layer improves the  $d_0$  resolution by a factor of 3 at low (1 GeV)  $p_T$  and by 1.6 at high (200 GeV)  $p_T$ .

The impact parameter resolution serves as input to the ATLAS  $b$ -tagging performance. For jets with a total energy of 200 GeV and for 50%  $b$ -tagging efficiency the light quark jet rejection is approximately 80. The  $b$ -tagging performance is degraded by 30% when a pixel layer is removed and by 10% if an SCT layer is removed. No layer was removed from the ID design because although removing a pixel layer improved the calorimeter performance the 30% loss in  $b$ -tagging performance was regarded as unacceptable. The four SCT layers were retained as they had marginal effect on the calorimeter and four layers instead of three provide redundancy for the ID.

The  $b$ -tagging performance of the ID was then used to evaluate the poten-

tial of the ATLAS detector to find a Higgs boson in the range  $80 < m_H < 120$  GeV. This mass range is a challenging region for the ATLAS detector where the  $b$ -tagging is used to the full. The channel provides a  $5\sigma$  discovery window out to  $m_H = 100$  GeV after three years' low luminosity data taking. The region is currently of interest given a possible signal at 115 GeV from the final LEP II experimental run. Using the analysis presented with the NLO cross-sections a significance of  $\simeq 4$  can be expected for a Higgs boson with  $m_H = 115$  GeV after three years' low luminosity running.

## References

- [1] OPAL Collaboration, *Search for the Standard Model Higgs Boson in  $e+e^-$  Collisions at  $\sqrt{s} = 192 - 209$  GeV*, CERN Pub EP/2000-156, Submitted to Phys. Lett. B. (2000)
- [2] J. Goldstone, A. Salam and S. Weinberg, *Broken Symmetries*, Phys. Rev. **127** (1962) 965
- [3] Super-Kamiokande Collaboration, *Measurements of the Solar Neutrino Flux from Super-Kamiokande's First 300 days*, Phys. Rev. Lett. **81** (1998) 1158-1162
- [4] F. Halzen and A. D. Martin, *Quarks And Leptons: An Introductory Course In Modern Particle Physics*, New York, USA: Wiley (1984)
- [5] I.J.R. Aitchison, *Standard Model Foundations*, in High Energy Phenomenology, Proceedings of the 42<sup>nd</sup> SUSSP, ed. KJ Peach and LLJ Vick, SUSSP Publications (1994)
- [6] W.N. Cottingham and D.A. Greenwood, *An Introduction to the Standard Model of Particle Physics*, Cambridge University Press (1998)
- [7] G. Wolf, HERA Physics, in High Energy Phenomenology, Proceedings of the 42<sup>nd</sup> SUSSP, ed. KJ Peach and LLJ Vick, SUSSP Publications (1994)

- 
- [8] D.E. Groom et al, *The European Physical Journal* **C15** (2000) 1
- [9] M. Kobayashi and J. Maskawa, *J. Prog. Theor. Phys* **49** (1973) 652
- [10] P.W. Higgs, *Broken Symmetries, Massless Particles and Gauge Fields*, *Phys. Lett.* **12** (1964) 132
- [11] S.L. Glashow, S. Weinberg. *Breaking Chiral Symmetry*, *Phys. Rev. Lett.* **20** (1968) 224
- [12] S. Weinberg, *A Model Of Leptons*, *Phys. Rev. Lett.* **19** (1967) 1264
- [13] ATLAS Collaboration, *Technical Proposal for a General-Purpose pp Experiment at the LHC at CERN*, CERN/LHCC/94-93 LHCC/P2 (1994)
- [14] LHC *Conceptual Design Report*, CERN/AC/95-05
- [15] LHCb Collaboration, *LHCb Technical Proposal*, CERN LHCC98-4 LHCC/P4 (1998)
- [16] ALICE Collaboration, *Technical Proposal for a Large Ion Collider Experiment at the LHC at CERN*, CERN/LHCC/95-71 (1995)
- [17] CMS Collaboration, *The Compact Muon Solenoid - Technical Proposal*, CERN/LHCC/94-38 (1995)
- [18] ATLAS Collaboration, *ATLAS Letter of Intent for a General-Purpose pp Experiment at the LHC at CERN*, CERN/LHCC/92-4 LHCC/I2 (1992)
- [19] ATLAS Collaboration, *ATLAS Detector and Physics Performance Technical Design Report*, CERN/LHCC99-14 (1999)

- 
- [20] ATLAS Collaboration, *Muon Spectrometer Technical Design Report*, CERN/LHCC/97-22 (1997)
- [21] ATLAS Collaboration, *Calorimeter Performance Technical Design Report*, CERN/LHCC/96-40 (1996)
- [22] ATLAS Collaboration, *Inner Detector Technical Design Report Volume 1*, CERN/LHCC/97-16 (1997)
- [23] ATLAS Collaboration, *Inner Detector Technical Design Report Volume 2*, CERN/LHCC/97-17 (1997)
- [24] ATLAS Collaboration, *Trigger Performance Status Report*, CERN/LHCC/98-15 (1998)
- [25] B.W. Lee et al., *Strength of Weak Interactions at Very High Energies and the Higgs Boson Mass*, Phys. Rev. Lett. **38** (1977) 883
- [26] M. Quiros, *Constraints on the Higgs boson properties from the effective potential*, hep-ph/9703412
- [27] R. J. Hawkings and A. R. Weidberg, *TRD Occupancies*, ATLAS Internal Note INDET-93-026
- [28] A. Ghinculov and T. Binoth, *Perturbative and Non-perturbative Higgs Signals*, Acta. Phys. Polon. **B30** (1999) 99
- [29] ALEPH 99-007 CONF-99-003, March 1999
- [30] OPAL Note PN382, March 1999
- [31] S. Wynnoff, *Standard Model Physics Results from Lep2*, Presented at the 5th International Symposium on Radiative Corrections (RADCOR-2000), hep-ex/0101016

- [32] M. Spira, *QCD Effects in Higgs Physics*, CERN-TH/97-68
- [33] Z. Kunszt, S. Moretti and W. J. Stirling, *Higgs Production at the LHC: an Update on Cross Sections and Branching Ratios*, *Z. Phys.* **C74** (1996)
- [34] S. Dawson, J. F. Gunion, H. E. Haber and G. L. Kane, *The Higgs Hunter's Guide*, Addison-Wesley, Reading MA, (1990)
- [35] G. Jarlskog and D. Rein, Proceedings of the "Large Hadron Collider Workshop", Aachen, 4-9 October 1990, eds. CERN 90-10, ECFA 90-133, (1990)
- [36] D. Froidevaux and E. Richter-Was, *Is the channel  $H \rightarrow b\bar{b}$  observable at LHC?*, ATLAS Internal Note PHYS-94-043 (1994), published in *Z. Phys.* **C67** (1995)
- [37] T. Sjostrand, *PYTHIA and JETSET Physics and Manual*, Computer Physics Commun. **82** (1994) 74
- [38] G. Corcella et al., *HERWIG 6 Manual*, hep-ph/0011363, Submitted to *J. High Energy Phys*
- [39] H.W. Baer, F.E. Paige, S.D. Protopopescu and X. Tata, *ISAJET 7.48 Manual*, hep-ph/0001086
- [40] GEANT Manual, CERN Program Library Long Writeup W5013.
- [41] DICE Documentation, [http://atlasinfo.cern.ch/Atlas/GROUPS/SOFTWARE/DOCUMENTS/DICE\\_320/dice320.html](http://atlasinfo.cern.ch/Atlas/GROUPS/SOFTWARE/DOCUMENTS/DICE_320/dice320.html)
- [42] R. Clift and A. Poppleton, *iPatRec: inner detector pattern-recognition and track-fitting*, ATLAS Internal Note SOFT-NO-009

- 
- [43] J.G. Loken and A. Reichold, *Description of a Pattern Recognition Algorithm using Continuous and Discrete Tracking Detectors*, ATLAS Internal Note INDET-96-132
- [44] I.Gavrilenko, *Description of Global Pattern Recognition Program (XKalman)*, ATLAS Internal Note INDET-97-165
- [45] PixlRec Documentation, <http://marpix1.in2p3.fr/Pixel/Plan/lv.html> or L. Vacavent Ph.D Thesis, University of Marseille (1997)
- [46] ZEBRA CERN Program Library Q100.
- [47] R. L. Gluckstern, *Uncertainties In Track Momentum And Direction Due To Multiple Scattering And Measurement Errors*, Nucl. Inst. and Meth. **24** (1963) 381
- [48] ATLAS Collaboration, *ATLAS Detector and Physics Performance Technical Design Report Section 3*, CERN/LHCC99-14 (1999)
- [49] R.E. Kalman, J. Basic Eng. **82** (1961) 34
- [50] S. Haywood, *Impact Parameter Resolution in the Presence of Multiple Scattering*, ATLAS Internal Note INDET-NO-091 (1995)
- [51] S.Haywood, *b-tagging with ATLAS Inner Detector using Fast Simulation*, ATLAS Internal Note INDET-NO-116 (1995)
- [52] R. M. Barnett et al., *Review of Particle Physics*, Physical Review **D54** (1996) 1
- [53] S.Haywood, *B-tagging using the ATLAS Inner Detector*, ATLAS Internal Note INDET-NO-92 (1994)

- [54] I. Gavrilenko et al., *Present status of b-tagging studies in ATLAS*, ATLAS Internal Note, INDET-NO-115 (1995)
- [55] ALEPH Collaboration, *A Precise Measurement of  $\Gamma_{Z \rightarrow b\bar{b}}/\Gamma_{Z \rightarrow \text{hadrons}}$* , Phys. Lett. **B313** (1993) 535.
- [56] J. Loken, A. Reichold, ATLAS Internal Note, INDET-NO-132
- [57] ATLAS Collaboration, *Calorimeter Performance Technical Design Report*, CERN/LHCC/96-40, Section 2.3.1 (1996)
- [58] ATLAS Collaboration, *Calorimeter Performance Technical Design Report*, CERN/LHCC/96-40, Section 2.3.2 (1996)
- [59] A. Rozanov, <http://marpix1.in2p3.fr/Pixel/dice/twothree/material.ps>
- [60] D. Barberis et al., *A comparative Study of Reduced Layouts of the ATLAS Inner Detector*, ATLAS Internal Note, INDET-NO-188 (1997)
- [61] CTEQ Collaboration, J. Botts et al., Phys. Lett. **B304** (1993) 159
- [62] E. Richter-Was, D. Froidevaux, L. Poggioli, *ATLFAST 2.0 a fast simulation package for ATLAS*, ATL-PHYS-98-131
- [63] B. Andersson, G. Gustafson, G. Ingelman and T. Sjostrand, Phys. Rep. **97** (1983) 31
- [64] E. Richter-Was, M Sapinski, *Search of the SM and MSSM Higgs boson in the  $t\bar{t}H$ ,  $H \rightarrow b\bar{b}$  channel*, ATLAS Internal Note ATL-PHYS-98-132
- [65] R. Bonciani et al., Nucl. Phys. **B529** (1998) 424
- [66] S. Dawson, L Reina, *QCD Corrections to associated Higgs boson production*, hep-ph/9712400

- 
- [67] CDF Collaboration, *The CDF Detector: An Overview*, Nucl. Instrum. Meth. **A360** (1995) 137
- [68] D0 Collaboration *The D0 Detector*, Nucl. Instrum. Meth. **A338** (1994) 185
- [69] F. Bedeschi, *Heavy Flavor Production In Hadronic Collisions*, submitted to World Scientific January 2001